KU LEUVEN

ARENBERG DOCTORAL SCHOOL
Faculty of Science

UNIVERSITÀ
CATTOLICA
del Sacro Cuore

Photo-transient metallization dynamics in the strongly correlated oxide V_2O_3: a temporally and spatially resolved perspective

Andrea Ronchi

Supervisors:
Prof. Dr. Jean-Pierre Locquet
Prof. Dr. Claudio Giannetti

Dissertation presented in partial
fulfilment of the requirements for the
degree of Doctor of Science (PhD):
Physics

December 2020

Photo-transient metallization dynamics in the strongly correlated oxide V_2O_3: a temporally and spatially resolved perspective

Andrea Ronchi

Examination committee:
Prof. Dr. Kristiaan Temst, chair
Prof. Dr. Jean-Pierre Locquet, supervisor
Prof. Dr. Claudio Giannetti, supervisor
Catholic University of the Sacred Heart (Italy)
Dr. Mariela Menghini, co-supervisor
KU Leuven/IMDEA (Spain)
Prof. Dr. Francesco Banfi, co-supervisor
Université Lyon 1 (France)
Prof. Dr. Michel Houssa, assessor
Prof. Dr. Luca Gavioli, assessor
Catholic University of the Sacred Heart (Italy)
Dr. Stefano Dal Conte, external member
Politecnico di Milano (Italy)
Prof. Dr. Lino da Costa Pereira, external member

Dissertation presented in partial fulfilment of the requirements for the degree of Doctor of Science (PhD): Physics

December 2020

© 2020 KU Leuven – Faculty of Science
Uitgegeven in eigen beheer, Andrea Ronchi, Celestijnenlaan 200D box 2417, B-3001 Leuven (Belgium)

Alle rechten voorbehouden. Niets uit deze uitgave mag worden vermenigvuldigd en/of openbaar gemaakt worden door middel van druk, fotokopie, microfilm, elektronisch of op welke andere wijze ook zonder voorafgaande schriftelijke toestemming van de uitgever.

All rights reserved. No part of the publication may be reproduced in any form by print, photoprint, microfilm, electronic or any other means without written permission from the publisher.

Acknowledgments

This thesis work is the result of a fantastic experience lasting more than 4 years. To be honest, I am not sure I could have achieved such good results without the help and support of many colleagues, family, and friends.

First of all, I would like to thank my promoters Prof. Claudio Giannetti and Prof. Jean-Pierre Locquet for choosing me for this interesting and promising international project between KU Leuven and the Catholic University of the Sacred Heart (Italy). Working in such an international group was a wonderful experience that allowed me to grow and mature not only as a young researcher but also as a person. Thank you both for guiding me during this (not short) journey and for taking the time to read and revise this manuscript. Thank you, Claudio, for always encouraging me to give my best and, specially, for the eye-opening scientific discussions. For me, you are not only a "boss" but also a real mentor and friend.

Second, I want to thank all the people who actively participated in this project, starting from the former members of the Functional Nanosystems group in Leuven: Dr. Mariela Menghini and Dr. Pía Homm. Without your participation in the numerous DLS beamtimes, it might have been a difficult task to obtain many of the results reported in this work. Mariela, thank you, in particular, for reading and sending me valuable feedback concerning this thesis and the articles published together. Pía, you have not only been a great colleague, but also a good friend. Indeed, you helped me to fit into a completely new working and living environment. A big thank you for mentoring me (by the way in the period of your defense, now I know what that means!!!) and for sharing with me your great experience in the lab.

To the former and current members of I-LAMP laboratories: Paolo Franceschini, Dr. Simone Peli, Dr. Nicola Nembrini, Dr. Andrea Sterzi, Dr.

Fabio Medeghini, and Dr. Selene Mor. Guys, spending these years with you has been wonderful. Simone, Andrea, and Nicola, I learned from you a lot of things about how to manage the experimental set up for time-resolved optical spectroscopy experiments. You have all been fantastic mentors and friends. It was fun to spend the days with you and then have a beer together at the end of the day...Paolo, what can I say?!? Thank you for being a great colleague, for having participated in all the beamtimes, from Trieste to Didcot, for having spent many evenings in the lab with me to finish the experiments, and for your patience with my rough manners. In short, thanks for being a true friend! What I'll miss the most will be your companionship in the lab...

I would also like to thank all the members of the jury: Prof. Kristiaan Temst, Prof. Michel Houssa, Prof. Lino da Costa Pereira, Prof. Luca Gavioli, Prof. Francesco Banfi, Dr. Stefano Dal Conte for taking the time to read my manuscript and giving me precious feedback during the pre-defense. In particular, thanks to Prof. Francesco Banfi and Prof. Gabriele Ferrini for following me during these years and for having been my mentors, respectively, during my bachelor's and master's degrees.

Thanks to the external collaborators Dr. Federico Cilento and Prof. Fulvio Parmigiani of the T-Rex facility at Elettra Sincrotrone Trieste for the time dedicated to me. The same goes for Dr. Francesco Maccherozzi, Dr. Ann Fitzpatrick, and Prof. Sarnjeet Dhesi of the i06 beamline at DLS. Thank you all for contributing to the success of the experiments reported in this thesis.

Thanks to Prof. Michele Fabrizio (SISSA, Trieste) and Andrea De Poli for their precious work with the theoretical simulations.

Thanks to all the colleagues, doctoral students, undergraduates, technicians, and administrators I met at some point during my PhD: Giulio, Gandalf, Gina, Andrea T., Giada, Federico, Paolo, Antonio, Sonia, Julia, Francesco, Valentina, Andrea C., Nicolò, Ali, Luca, Linda, Emanuele, Giovanni, Chahan, Maurizio, and Marina (I hope I have not forgotten anybody!)...and the bartenders Paola, Grazia, and Roby.

Thanks to Leuven's friends and colleagues: Simon, Wei-Fan, LeeWoon, Wout, Matias, Mattias, Piero, Jan, Bram, and Asteri...In particular, I need to thank Wout Keijers for the invaluable help in wire-bonding the samples

and for teaching me how to do them by myself. Thanks also to Simon Mellaerts for helping me with the Dutch translation of the summary.

I acknowledge financial support from MIUR through the PRIN 2017 program (Prot. 20172H2SC4_005).

I will now dedicate a few words in Italian to my beloved family and my dearest friends: *Cari Mamma, Papà e Matteo, veramente grazie!!! In questo lungo percorso ci siete sempre stati, mi avete supportato e sopportato quando le cose si facevano più dure e difficili. Non è stato un percorso facile, nulla lo è nella vita. Voi però mi siete stati sempre vicino pronti a sostenermi con parole di conforto e incoraggiamento, e mai una volta avete avuto dubbi sulle mie reali capacità. Non vi sarà mai abbastanza grato per tutto questo!!! Ringrazio anche tutti i miei parenti, dai nonni, Roberto e Franca, agli zii paterni Salvatore, Carlo, Stefano, Eugenio, Vittorina, Lorenzo con Paolo e Francesca, fino a mia zia Patty con Hernan, Davide e il piccolo Mattia. Grazie a tutti per essere stati parte della mia vita. Se sono l'uomo che sono, è grazie anche a tutti voi. Vi voglio bene!!!*

Ai miei più cari amici, per lo più amici arrampicatori e alpinisti, con cui ho condiviso le mie più belle avventure in montagna. La vostra compagnia è stata una fondamentale valvola di sfogo nei momenti più impegnativi e stressanti. Porto ciascuna avventura vissuta insieme come un piccolo tesoro preziosamente custodito nel mio cuore. Grazie a Compagno Pappagallo, Dido e Boris gli amici di sempre, quelli con cui ho iniziato a muovere i primi passi di arrampicata. Quelli con cui in montagna si andava per divertirsi e stare insieme, alla ricerca di avventure che ricalcassero i passi di quell'alpinismo un po' romantico, ormai andato perso. Grazie a Pedro (grande maestro e amico) e Fabio, compagni sinceri con cui ho sempre avuto modo di confidarmi e che hanno sempre trovato il tempo per ascoltare i miei pensieri. Grazie ai compagni più recenti, Fili, Sandro, e Luca che mi hanno spronato a dare il massimo e ad ottenere grandi soddisfazioni anche in questo sport. Grazie anche a Francy, Giulia Z., Marta, Sergio, Willy, Luca L., Luca B., Chiara, Dani, Giulia P., e Giulietta... Un ringraziamento più in generale a tutte le persone incontrate grazie alla Società Escursionisti Bresciani "Ugolino Ugolini". Partendo da coloro che mi hanno dedicato volontariamente il loro tempo per avviarmi a questo bellissimo sport e a tutti quelli che hanno condiviso con me almeno una salita in montagna. Grazie veramente a tutti!

Come non dimenticare poi gli amici incontrati durante quella lunga parentesi durata 13 anni che è stata per me lo scoutismo. Ho vissuto con voi alcuni dei momenti più belli e spensierati della mia gioventù. Rimpiango ancora le nottate passate attorno ai falò, cantando canzoni degli 883, Ligabue o Vasco...Le disavventure duranti gli hike di squadriglia, il cibo pessimo e le ragazzate combinate insieme! E qui, non posso non ringraziare Andrea, il mio più caro amico di quel periodo. Ci sentiamo poco ma, quando lo facciamo, sembra che il tempo non sia mai passato. Grazie amico per esserci!

Infine, grazie agli amici delle superiori, Reddy, Gatti ed Elia. Siamo sempre i soliti 4 pirla, ma è sempre bello ritrovarsi e ricordare i bei tempi passati!

In short, you have all left a mark, some smaller, some bigger, and all these marks made me the person I am today and who achieved the precious and sought-after goal that is the PhD degree! Thank you all!!! Alé duri!!!

Andrea Ronchi
December 2020

Summary

The use of Mott insulators for new technological applications is one of the most attractive paths for the future of electronics and computer science. These materials undergo an Insulator-to-Metal transitions (IMT) that can be controlled by means of external stimulations as temperature, pressure, magnetic and electric fields and photoexcitations [Basov et al. (2017); Tokura et al. (2017)]. This great tuning possibility makes Mott insulators key materials for novel electronic devices belonging to the Mottronics family. For instance, artificial neuromorphic networks based on Mottronic devices can pave the way to improving the actual possibility to analyze big data, recognize patterns and, as ultimate step, realizing artificial intelligence architectures able to mimic the human brain [Stoliar et al. (2017); del Valle et al. (2018, 2019)]. In this context, the development of ultrafast volatile resistive switching protocols seems to offer a good way to implement the "Leaky, Integrate, and Fire"(LIF) behavior, characteristic of biological neurons.

In particular, this thesis work is focused on Vanadium Sesquioxide (V_2O_3), prototype for the Mott transition, in which the Insulator-to-Metal Transition (IMT) takes place at $\sim$ 170 K and is accompanied by a change in the lattice crystal structure from monoclinic to corundum [McWhan et al. (1969)]. Unfortunately, this Structural Phase Transition (SPT) is the real bottleneck in realizing devices able to reversibly switch at THz frequencies. Therefore, in order to make more attractive the implementation of V_2O_3-based devices in neuromorphic networks or, more in general, in Mottronics, overcoming this barrier is the main goal in the field. In fact, during the Resisitve Switching (RS), the transition from insulator to metal is mainly thermally induced, that means that the fast electronic Mott transition is limited in speed by the structural transition. To avoid the heating effect, it has been shown that it is possible to photoinduce a non-thermally driven transition

by changing the orbital polarization with a pulsed femtosecond laser [Sandri and Fabrizio (2015); Abreu et al. (2017)].

These results inspired the fundamental idea behind this thesis work which is the combination of electrical stimulus (voltage) applied during the RS with the possibility of decoupling the electronic transition from the structural one offered by the non-thermal photoexcitation. The aim of the work is therefore to combine a voltage bias with laser excitations to obtain an ultrafast and reversible non-thermal switching in an actual Mottronic device. It is important to stress that, during the RS, the birth and growth of metallic nuclei is spatially inhomogeneous with a formation of metallic filaments between the electrodes. For this reason it is of crucial importance to study the spatial configuration of the initial insulating state of the system and how it evolves during the IMT transition through microscopy techniques sensitive to structural and electronic changes at the nanoscale.

Driven by these purposes, we performed PhotoEmission Electron Microscopy (PEEM), time-resolved PEEM and time-resolved optical spectroscopy experiments to address some important questions related to the spatial and temporal dynamics of the IMT in V_2O_3 thin films:

i) How does the insulating phase spatially look like at the nanoscale? Is there any intrinsic nanotexture? If yes, is this nanotexture controlling somehow the birth and growth dynamics of the metallic nuclei?

ii) Which is the nature of the photoexcited metallic metastable state? Is it possible to transiently sustain a monoclinic metal? Could the monoclinic nanotexture favour the formation of a monoclinc metal? Is this transient non-thermal state exploitable in ultrafast switching devices?

iii) Is it possible to induce a non-thermal metallic state out for the insulating ground state by combining photoexcitation with electric field?

The PEEM experiments unveiled, for the first time, a spontaneous self-organization of the Mott insulating phase, characterized by striped monoclinic domains with different orientations (see Chapter 3). The insulating stripes are stable and reproducible, as they form in the same position under temperature cycling. The boundaries of this intrinsic nanotexture host the birth of metallic seeds, whose expansion can be triggered by the impulsive photoinduced change of the orbital population (see Chapter 4). The timescale of the growth process (tens of picoseconds) corresponds to the propagation at the sound velocity across the transverse dimension of the insulating stripes. Therefore, our results show that this nanotexture strongly affects the nucleation and growth dynamics of the photoinduced metallic phase. This photoinduced metastable metallic state retains the in-plane monoclinic distorsion confirming the possibility to non-thermally decouple the IMT and Structural Phase Transition (SPT), with great benefit on the transition speed. (see Chapter 5). Numerical simulations support the hypothesis that this intriguing result is, in particular, favored by the presence of the monoclinic nanotexture itself. The final goal of the thesis, i.e. the combination of near-infrared laser pulses with a voltage bias below the threshold to induce the complete RS, was achieved by demonstrating the possibility to favour the metallization of the system well beyond what can be ascribed to thermal effects (see Chapter 6).

The use of the multi excitation protocol proposed in this work could allow a volatile switching in neuromorphic networks faster than what has been obtained up to now through the use of the electric fields alone. In addition, the new results reported in this thesis work call for the possibility of suitably engineering the boundaries of the nanotextured insulating phase in V_2O_3 thin films to control the electronic and magnetic switching of Mott insulators at THz frequencies, with impact on the development of novel Mottronic devices.

Samenvatting

Het gebruik van Mott-isolatoren voor nieuwe technologische toepassingen is één an de meest aantrekkelijke wegen voor de toekomst van elektronica en informatica. Deze materialen ondergaan isolator-naar-metaal overgangen IMT die gecontroleerd kunnen worden door middel van externe stimuli zoals temperatuur, druk, magnetische/elektrische velden en foto-excitaties [Basov et al. (2017); Tokura et al. (2017)]. Deze geweldige mogelijkheid om te worden afgestemd, maakt de Mott-isolatoren de belangrijkste materialen voor nieuwe elektronische apparaten die tot de Mottronics-familie behoren. Artificiële neuromorfe netwerken op basis van Mottronics-apparaten kunnen bijvoorbeeld de weg effenen voor het verbeteren van de feitelijke mogelijkheid om big data te analyseren, patronen te herkennen en, als ultieme stap, artificiële intelligentie-architecturen te realiseren die het menselijk brein kunnen nabootsen [Stoliar et al. (2017); del Valle et al. (2018, 2019)]. In deze context lijkt de ontwikkeling van ultrasnelle volatiele resistieve schakelprotocollen een goede manier te bieden om het “Leaky, integrate, and fire” (LIF) gedrag, kenmerkend voor biologische neuronen, te implementeren.

In het bijzonder is dit proefschrift gericht op Vanadium Sesquioxide, het prototype van de Mott-transitie, waarin de IMT plaatsvindt op ~ 170 K en gepaard gaat met een verandering in de kristalstructuur van het rooster van monoklien naar korund [McWhan et al. (1969)]. Helaas is deze structurele faseovergang (SPT) de echte bottleneck bij het realiseren van apparaten die omkeerbaar kunnen schakelen op THz-frequenties. Om de implementatie van V_2O_3-gebaseerde apparaten in neuromorfe netwerken, of meer algemeen in Mottronics, aantrekkelijker te maken, is het overwinnen van deze barrière daarom het belangrijkste doel in het veld. In feite wordt tijdens de Resisitve Switching (RS) de overgang van isolator naar metaal voornamelijk thermisch geïnduceerd, wat betekent dat de snelle elektronische Mott-overgang in snelheid wordt beperkt door de structurele overgang. Om het verwarmingseffect te vermijden, is aangetoond dat het mogelijk is om een niet-thermisch aangedreven overgang te foto-induceren door de orbitale polarisatie te veranderen met een gepulseerde femtoseconde laser [Sandri and Fabrizio (2015); Abreu et al. (2017)].

Deze resultaten suggereren het fundamentele idee achter dit proefschrift, namelijk de combinatie van elektrische stimulus (spanning) aangelegd tijdens de RS met de mogelijkheid om de elektronische en structurele overgang van elkaar te ontkoppelen en dit met behulp van niet-thermische foto-excitatie. Het doel van dit het werk is daarom om een spanningsaanpassing te combineren met laser-excitaties om een ultrasnelle en omkeerbare niet-thermische schakeling te verkrijgen in een echt Mottronic-apparaat. Het is belangrijk om te benadrukken dat tijdens de RS de geboorte en groei van metallische kernen ruimtelijk inhomogeen zijn met een vorming van metallische filamenten tussen de elektroden. Om deze reden is het van cruciaal belang om de ruimtelijke configuratie van de initiële isolatietoestand van het systeem te bestuderen en hoe het evolueert tijdens de overgang door middel van microscopietechnieken die gevoelig zijn voor structurele en elektronische veranderingen op nanoschaal.

Gedreven door deze doeleinden, hebben we PEEM-, tijdopgeloste PEEM- en tijdopgeloste optische spectroscopie-experimenten uitgevoerd om enkele belangrijke vragen met betrekking tot de ruimtelijke en temporele dynamica van de in V_2O_3 dunne films te beantwoorden:

i) Hoe ziet de isolatiefase er ruimtelijk uit op nanoschaal? Is er een intrinsieke nanotextuur? Zo ja, regelt dit nanotextuur op de een of andere manier de geboorte- en groeidynamiek van de metaalkernen?

ii) Wat is de aard van de foto-geëxciteerde metastabiele toestand? Is het mogelijk om tijdelijk een monoklien metaal te stabiliseren? Zou de monokliene nanotextuur de vorming van een monoklinisch metaal kunnen bevorderen? Kan deze kortstondige niet-thermische toestand worden misbruikt in ultrasnelle schakelapparaten?

iii) Is het mogelijk om een niet-thermische metallische toestand te induceren voor de isolerende grondtoestand door foto-excitatie te combineren met een elektrisch veld?

De PEEM-experimenten onthulden voor de eerste keer een spontane zelforganisatie van de Mott-isolatiefase, gekenmerkt door gestreepte monokliene domeinen met verschillende oriëntaties (zie Hoofdstuk 3). De isolerende strepen zijn stabiel en reproduceerbaar, aangezien ze zich in dezelfde positie vormen bij temperatuurwisselingen. De grenzen van deze intrinsieke nanotextuur herbergen de geboorte van metallische zaden, waarvan de expansie kan worden veroorzaakt door de impulsieve foto-geïnduceerde verandering van de orbitale populatie (zie Hoofdstuk 4). De tijdschaal van het groeiproces (tientallen picoseconden) komt overeen met de voortplanting van de isolatiestroken over de dwarsafmeting met de snelheid van het geluid. Daarom laten onze resultaten zien dat deze nanotextuur de kiemvorming en groeidynamiek van de foto-geïnduceerde metallische fase sterk beïnvloedt. Deze foto-geïnduceerde metastabiele metallische toestand behoudt de monokliene vervorming in het vlak, wat de mogelijkheid bevestigt om de IMT en SPT niet-thermisch te ontkoppelen, met groot voordeel voor de overgangssnelheid. (zie Hofdstuk 5). Numerieke simulaties ondersteunen de hypothese dat dit intrigerende resultaat met name wordt bevorderd door de aanwezigheid van de monokliene nanotextuur zelf. Het uiteindelijke doel van het proefschrift, namelijk de combinatie van nabij-infrarode laserpulsen met een spanningsafwijking onder de drempel om de volledige RS te induceren, werd bereikt door de mogelijkheid aan te tonen om de metallisatie van het systeem te begunstigen, veel verder dan wat enkel kan worden toegeschreven aan thermische effecten (zie Hofdstuk 6).

In neuromorfe netwerken zou het gebruik van het multi-excitatieprotocol dat in dit werk wordt voorgesteld, een vluchtige omschakeling mogelijk maken die sneller is dan wat tot nu toe is verkregen door het gebruik van enkel alleen de elektrische velden. Bovendien bieden de nieuwe resultaten die in dit proefschrift worden gerapporteerd de mogelijkheid om de grenzen van de nanotextured isolatiefase in dunne V_2O_3-films op passende wijze te manipuleren om de elektronische en magnetische schakeling van Mott-isolatoren op THz-frequenties te regelen, met impact op de ontwikkeling van nieuwe Mottronic-apparaten.

List of Abbreviations

AFI Antiferromagnetic Insulating.

AFM Atomic Force Microscopy.

BEMA Bruggeman Effective-Medium Approximation.

CMOS Complementary Metal-Oxide Semiconductor.

DLM Drude-Lorentz Model.

DLS Diamond Light Source.

DMFT Dynamical Mean-field Theory.

DOF Degree of Freedom.

DOS Density of States.

FFT Fast Fourier Transform.

FOV Field Of View.

FT Fourier Transform.

FWHM Full Width at Half Maximum.

GL Ginzburg-Landau.

ILAMP Interdisciplinary Laboratories for Advanced Materials Physics.

IMT Insulator-to-Metal Transition.

KUL KU Leuven.

LDA Local Density Approximation.

LH Linear Horizontal.

LHB Lower Hubbard Band.

MBE Molecular Beam Epitaxy.

MIT Metal-to-Insulator transition.

OPA Optical Parametric Amplifier.

PDA PhotoDiode Array.

PEEM PhotoEmission Electron Microscopy.

PFM PiezoForce Microscopy.

PI Paramagnetic Insulating.

PINES Photo-induced Transient Non-Equilibrium States.

PIPT Photo-induced Phase Transition.

PM Paramagnetic Metallic.

QP Quasiparticle Peak.

RS Resisitve Switching.

RSM Reciprocal Space Map.

RT Room Temperature.

s-SNOM Scattering Scanning Near-field Optical Microscopy.

SC Supercontinuum.

SPEM Scanning Photoemission Microscopy.

SPT Structural Phase Transition.

SQUID Superconducting Quantum Interference Devices.

STM Scanning Tunneling Microscopy.

TMO Transition Metal Oxide.

UCSC Universitá Cattolica del Sacro Cuore.

UHB Upper Hubbard Band.

UOS Ultrafast Optical Spectroscopy.

XAS X-ray Absorption Spectroscopy.

XLD X-ray Linear Dichroism.

XRD X-ray Diffraction.

XRR X-ray Reflectivity.

List of Symbols

$2\Delta_{eff}$ effective Mott gap.

D diffusion coefficient.

E_{abs} absorbed energy.

$F_M(t)$ time-dependent metallic filling fraction.

G_{cr} metallic nucleus energy barrier for stability.

K rate of increasing (t).

N Avrami's coefficient.

$R_M(\omega)$ metallic reflectivity.

$T_{\mathbf{C}}$ critical temperature.

U Coulomb repulsion.

W one-band bandwidth.

$\Delta T/T$ relative variation of transmission.

$\Delta\sigma$ variation of optical conductivity.

α_{cr} metallic nucleus surface tension.

δF_M metallic filling fraction variation.

δN photoexcitation.

$\delta R/R$ relative variation of transmission.

δp orbital polarization.

ϵ_{eff} effective dielectric function.

λ wavelength.

ω angular frequency.

σ_1 optical conductivity.

c speed of light.

$k_{\mathbf{b}}$ Boltzmann's constant.

$n_{\mathbf{c}}$ occupation density in conduction band.

$n_{\mathbf{v}}$ occupation density in valence band.

s_{cr} metallic nucleus critical surface.

t_{pp} time delay between pump and probe pulses [ps].

v_{cr} metallic nucleus critical volume.

2Δ Mott gap.

Contents

Acknowledgments **i**

Summary **v**

Samenvatting **ix**

List of Abbreviations **xiii**

List of Symbols **xvi**

Contents **xix**

1 Ultrafast control of Mott materials **1**

- 1.1 Mott physics in correlated materials 1
- 1.2 Toward the control of Mott materials 3
  - 1.2.1 Resistive switching: Mottronics and neuromorphic applications 5
  - 1.2.2 Photo-induced phase transition in Mott systems . . 11
- 1.3 Probing the dynamics of the Mott transition 13

2 V_2O_3: Prototype for the Mott transition **21**

- 2.1 Metal-to-Insulator in V_2O_3 21
  - 2.1.1 Phase diagram 21
  - 2.1.2 Crystal structure 22
  - 2.1.3 Electronic structure 24
- 2.2 Dynamics of the Metal-to-Insulator transition 26
  - 2.2.1 Spatial inhomogenities and phase coexistence 26
  - 2.2.2 Temporal dynamics of the transition 29
  - 2.2.3 Metastability of the monoclinc metallic phase 34

3 Spontaneous self-organization of the monoclinic insulating phase 39
3.1 Experimental technique: Photoemitted Electron Microscopy (PEEM) 40
3.2 Results and discussion 41
3.3 Conclusion 50

4 Early-stage metalization triggered by photoinduced orbital polarization 51
4.1 Experimental technique: Time-Resolved Optical Spectroscopy 52
4.2 Results and discussion 54
4.3 Conclusion 66

5 Evidence of transient monoclinic metal-like state in V_2O_3 69
5.1 Experimental technique: tr-PEEM 70
5.2 Results and discussion 74
5.3 Conclusion 79

6 Non-thermal light-assisted resistance collapse in a V_2O_3-based Mottronic device 81
6.1 Experimental details 83
  6.1.1 Device fabrication 83
  6.1.2 Photo-induced resistivity measurements 83
  6.1.3 Finite Elements Method simulation of the thermal problem 86
6.2 Results and discussion 88
6.3 Conclusion 91

7 Conclusion and outlook 93

Appendices 97

A Thin films growth details and sample list 98

B PEEM images analysis 100
B.1 Evaluation of the metallic filling fraction F_M 100
B.2 PEEM resolution 100
B.3 Study of the Antiferromagnetic Insulating (AFI) monoclinic domain orientation 102

C Reflectivity variation and Bruggeman Effective Medium Approximation 103

D Sample holder drawings for electrical and optical measurements 106

Bibliography 111

Curriculum Vitae 126

List of Publications 128

Chapter 1

Ultrafast control of Mott materials

1.1 Mott physics in correlated materials

In the past fifty years, condensed matter physics has been dominated by the study of quantum correlated systems, whose properties and functionalities are originated by many-body physics. In most cases, this new class of materials presents emergent phenomena and exotic properties driven by the very strong electron-electron interactions and the possible different coupling of the relevant electronic degrees of freedom (charge, spin and orbital) to the atomic and crystal potential (see Fig. 1.1 adapted from Ref. Tokura et al. (2017)). Among all these exotic phenomena we can name, for instance, insulator-to-metal Mott transitions, high-temperature superconductivity, and colossal magnetoresistance. The possibility to control and change these properties on-demand by applying small external stimuli as electric and magnetic field, optical photoexcitation, thermal heating and mechanical stress opens new scenarios for developing the next-generation of solid state devices [Basov et al. (2017)]. In particular, the main application fields are ultra-low power consumption to cope with the impending energy crisis and dissipationless electronics; energy harvesting for photovoltaics and thermoelectrics; and quantum computing and quantum technologies.

Nowadays, it is well-known that Silicon-based electronic devices are reaching their miniaturization limits, due to the impossibility to have enough charge

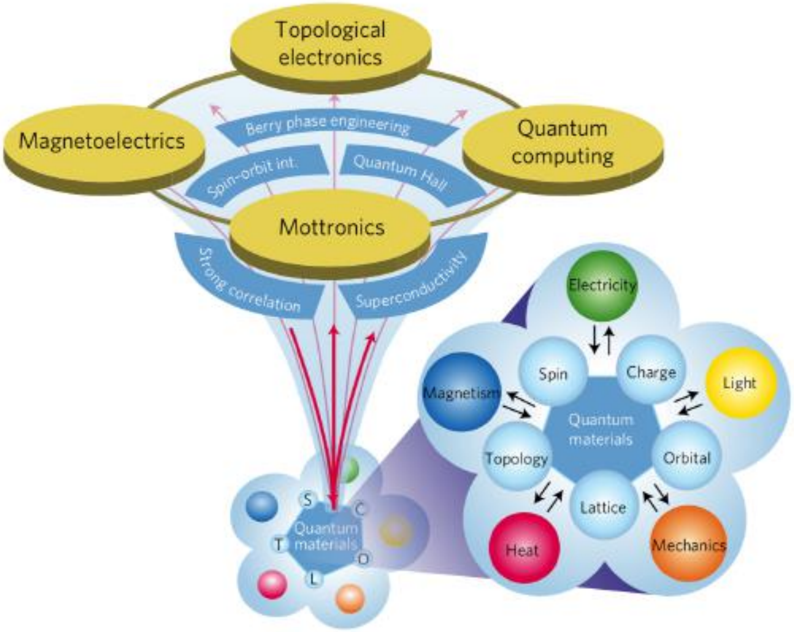
Topological electronics
Magnetoelectrics
Quantum computing
Berry phase engineering
Spin-orbit int.
Quantum Hall
Mottronics
Strong correlation
Superconductivity
Electricity
Spin
Charge
Light
Magnetism
Quantum materials
Topology
Orbital
Lattice
Heat
Mechanics
S
C
T
O
L
Quantum materials

Figure 1.1: **Controlling quantum materials on-demand.** The pentagon shows the coupling of the various degrees of freedom in strongly correlated materials with external stimuli. These strong interactions lead to the emergence of a new class of functionalities that might be used for developing new technological applications. Adapted from [Tokura et al. (2017)].

carriers in a nanometer-scale cell. In this scenario, one of the most interesting and promising feature for future electronic devices is the Mott transition [Tokura et al. (2017); Basov et al. (2017); Inoue and Rozenberg (2008); Yang et al. (2011)]. When atoms are well ordered in space, they form a lattice structure. The orbitals of those atoms then combine to form a new set of eigenfunctions, which extend throughout the full lattice and correspond to plane waves modulated by the Bloch's function [Bloch (1928)]. The eigenenergies of these eigenfunctions are organized into discontinuous bands of energy. When at T = 0 K, all these bands are fully occupied by two electrons per electronic state, the system behaves as a "band" insulator. Therefore, the picture emerging from this simple consideration is that systems with an odd number of non-interacting electrons in its upper filled band are metals, while those with even number can be band insulators [Bethe (1928); Sommerfeld (1928)]. However, in some relevant cases, band-structure theory, which is based on the independent-electron approximation, fails. In fact, some solids with an odd number of electrons in the highest occupied band are insulators. This possibility was envisaged by Sir Neville

Mott in the 1940s [Mott (1990)]. The reason of this anomalous behaviour is due to the strong Coulomb repulsion U between two electrons occupying the same orbital; which "freezes" the single electron on its atomic site. In this picture, systems with an odd number of electrons, which are expected to be metallic, may turn into insulators. Therefore, to distinguish a Mott system, the simplest argument amounts to consider a free-electron system and to evaluate the magnitudes of the kinetic and potential energies as a function of the density. Indeed, when the value of U overcomes the bandwidth W, the electron motion is frozen, despite the fact that the N atomic orbitals contain an odd number of electrons. As a consequence, there is the formation of two characteristic bands separated by U, the full-filled Lower Hubbard Band (LHB) and the empty Upper Hubbard Band (UHB) (see Fig.1.2 (a)). The energy separation between the LHB and the first empty level in the conduction band is called Mott gap ($\sim$ 1-10 eV, depending on the compound). Above the critical temperature T_C, which might range from 0 K to above Room Temperature (RT) according with the energy scale of the e-e correlations in the different compounds, the material behaves as a correlated metal.

1.2 Toward the control of Mott materials

A peculiar class of Mott systems with interesting electronic and magnetic properties are the transition-metal oxides, which are mostly dominated by the physics of the d-orbitals electrons. The spin, charge and orbital degrees of freedom and their coupling can produce versatile electronic phases with phase separation and pattern formation as spin, orbital, and charge ordering. In general, the Mott transition belongs to either of two categories [Imada et al. (1998)] (see Fig.1.2 (b)); bandwidth controlled IMT, in which the effective electron correlation strength, represented by the ratio of the electron correlation energy U to the one-electron bandwidth W, changes; and band-filling controlled, in which the electron number n per atomic site (for example, half-filling state; n = 1) is changed by chemical, electrostatic or photo doping. Bandwidth-controlled and filling-controlled Metal-to-Insulator transition (MIT)s are typically observed in the family of perovskites (AMO_3) and pyrochlores ($A_2M_2O_7$), where M is the transition metal, in which the A-site ionic size can control the bandwidth by changing the O–M–O bond length or angle, and the mixed ionic valences in the A site can change the band filling [Tokura (2003)]. The perovskites have been

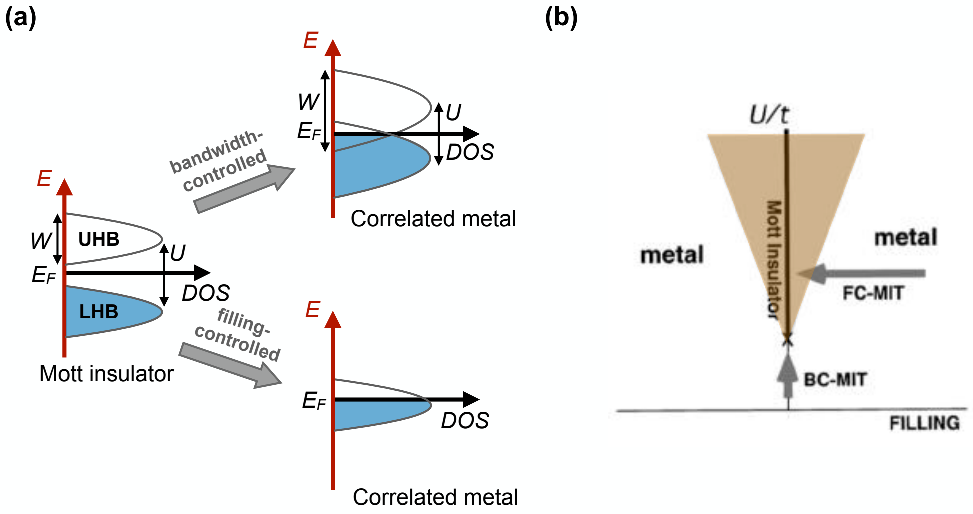

Figure 1.2: **Control of the Mott transition.** (a) In general, Mott transitions can be achieved through bandwidth or filling control. The change of the bandwidth W and the filling with extra carriers can lead to the collapse of the Mott gap. Adapted from [Zhou and Ramanathan (2013)]. (b) Metal-insulator phase diagram based on the Hubbard model in the plane of U/t and filling n. The shaded area is in principle metallic but under the strong influence of the metal-insulator transition, in which carriers are easily localized by extrinsic forces such as randomness and electron-lattice coupling. Two routes for the MIT (metal-insulator transition) are shown: the FC-MIT (filling-control MIT) and the BC-MIT (bandwidth-control MIT). Adapted from [Imada et al. (1998)].

demonstrated to be one of the most promising compounds for photovoltaic solar cells, with an optical bandgap that can be easily tuned between $\sim$ 1.55-2.3 eV [Razza et al. (2016)]. Thanks to this enormous flexibility, it was possible to increase the conversion efficiency up to 30 % during the last decades [Nishigaki et al. (2020); Bhandari and Ellingson (2018); Maniarasu et al. (2018)]. On the other hand, the pyrochlores are being put forward as materials for use in wide application fields including solid electrolytes [Shimizu and Maeda (1998)], anodes [Porat et al. (1997)] and cathodes [Porat et al. (1996)] for fuel cells and sensors, catalysts [Sohn et al. (2003)], dielectrics [Dimoulas et al. (2004)] and materials for the encapsulation of actinides and other nuclear wastes.

Another example of band-filling-controlled MIT is the case of copper-oxide superconductors, where a quasi-two-dimensional electronic structure with half filling (one hole per Cu) forms the parent correlated insulator composed of CuO_2 square-lattice sheets sandwiched by ionic block layers which acts as the charge reservoirs [Imada et al. (1998); Tokura et al.

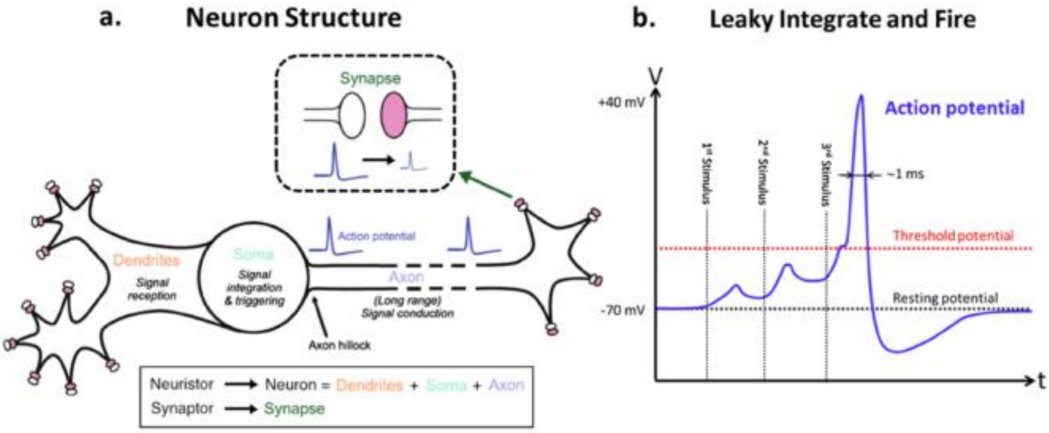
a.
Neuron Structure
Synapse
Dendrites
Signal reception
Soma
Signal integration & triggering
Action potential
Axon
(Long range) Signal conduction
Axon hillock
Neuristor → Neuron = Dendrites + Soma + Axon
Synaptor → Synapse
b.
Leaky Integrate and Fire
V
+40 mV
-70 mV
t
1st Stimulus
2nd Stimulus
3rd Stimulus
Action potential
~1 ms
Threshold potential
Resting potential

Figure 1.3: (a) Schematic design of the structure of a neuron. (b) The voltage spiking of a neuron showing the LIF after a well-defined threshold potential is reached. Adapted from del Valle et al. (2018) and previously shown in Serdijn and Dongen (2016).

(2017)]. In this class of materials the reduction or increment of the electron or hole doping can tune the superconductive dome and, as a consequence, leading to the highest possible critical temperature T_C. Needless to say, the exploration forwards room-temperature (RT) superconductors is of tremendous relevance for technological applications, from lossless power cables [Shiohara et al. (2011); Sato et al. (2011)] to superconducting magnets in medical applications, motors, and highly sensitive magnetic-field sensors employing Superconducting Quantum Interference Devices (SQUID) [Krause and Kreutzbruck (2002); Tokura et al. (2017)].

1.2.1 Resistive switching: Mottronics and neuromorphic applications

Upon external stimulation, such as by chemical doping, electrostatic doping, pressure, or electric and magnetic field application, the MIT can be exploited for many different technological applications [Tokura et al. (2017); Basov et al. (2017)]. Among all these control mechanisms, electrical switching is the most useful for electronic devices. For instance, two- or three-terminal field-effect Mott transistors made by VO_2 films can be used as ultrafast ON/OFF electronic switches [Inoue and Rozenberg (2008)]. Since during the IMT the systems are highly spatially inhomogeneous due to the coexistence of metallic and insulating nano-domains (first order phase transition), the application of new spatially-resolved techniques to address how this

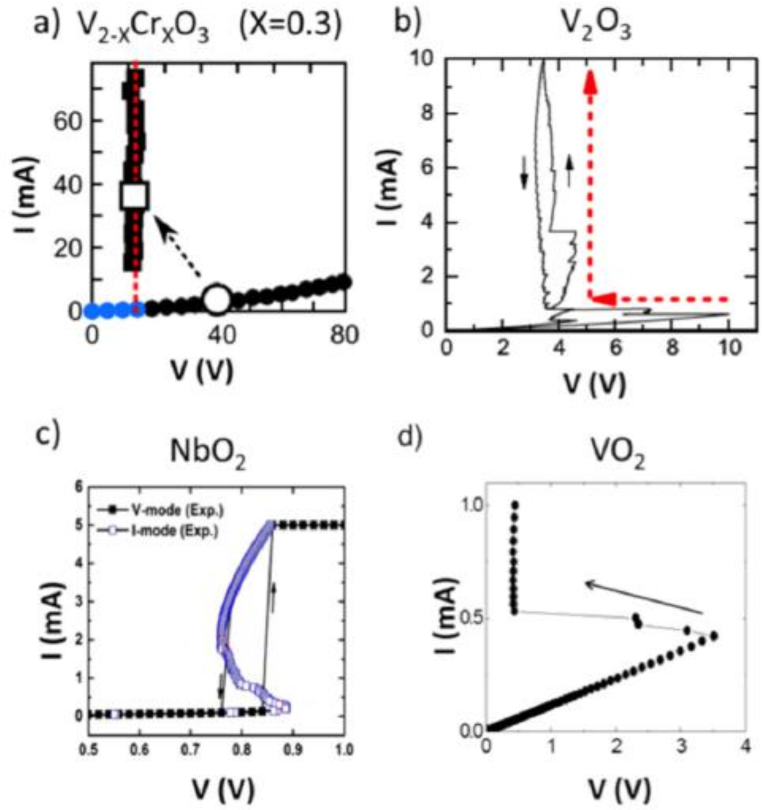

Figure 1.4: **I-V curves showing volatile Resisitve Switching (RS) in three Mott systems.** (a) $V_{2\text{-x}}Cr_xO_3$ (x = 0.3), adapted from Stoliar et al. (2013). (b) V_2O_3, adapted from Guénon et al. (2013). (c) NbO_2, adapted from Liu et al. (2016). (d) VO_2, adapted from del Valle et al. (2019). Figure adapted from del Valle et al. (2018).

spontaneous nanotexture affects the switching properties is becoming a topic of great interest [Dönges et al. (2016); McLeod et al. (2016); Singer et al. (2018); Lupi et al. (2010)]. The application of such devices in integrated circuits is very attractive for non-volatile memories called Resistive Random Access Memory (ReRAM), where information is memorized as metallic or insulating states of a device unit in a non-volatile and rewritable way [Sawa (2008); Waser and Aono (2007)]. Higher speed, higher-density integration and low power consumption are the main advantages of ReRAM with respect to the typical flash memories based on semiconductor technologies. Other common applications of Transition Metal Oxide (TMO)s devices are optical, thermal and chemical sensors [Yang et al. (2011)] and neuromorphic computers [del Valle et al. (2018)].

Breaking away from the classical Turing-von Neumann machine paradigm to implement new types of bio-inspired ("neuromorphic") electronic devices or cognitive hardware [Mead (1990)] may allow for the implementation of artificial neural networks. These AI systems are achieving remarkable feats, from beating the best chess and go players to recognizing faces in a crowded places [LeCun et al. (2015)], pushing ahead the computational possibilities in outstanding ways. In a neuromorphic computer, exactly as in a brain, synapses and neurons are replaced by artificial devices, respectively, synaptors and neuristors, that act like the biological ones (see Fig. 1.3 (a)). In particular, the neuristors are the central element of the circuit [Bear et al. (2007)], they produce electrical signals (like spikes) triggered by an external stimulation or excitation. If the excitation voltage exceeds the voltage threshold, the neuristor "fires" an electrical spike [Gerstner et al. (2014)] mimicking a behavior called "Leaky, integrate, and fire" (LIF) characteristic of biological neurons (Fig. 1.3 (b)).

The first simplest and most immediate choice for the realization of neuromphic computers was the use of conventional Complementary Metal-Oxide Semiconductor (CMOS) devices [Mahowald and Douglas (1991)]. Unfortunately, such a network requires a lot of classic CMOS [Indiveri et al. (2011)], which greatly increase the energy consumption. A particularly interesting approach attempts to implement all the important neuro-biological features and functionalities in a unique device, by means of Resisitive Switching (RS), where the resistivity of the device depends on the voltage or current applied. There are two types of RS: *volatile* and *non-volatile*. In the former case, the phenomenon is a sudden collapse of the resistance under the action of an external electric field, which spontaneously returns to the initial state [Janod et al. (2015); Imada et al. (1998)]. Therefore, the systems does not keep memory of the switching. This kind of resistive switching is commonly observed in materials that feature a temperature-driven MIT, for instance, NbO_2, VO_2, and $V_{2\text{-x}}Cr_{x}O_3$ (see Fig. 1.4). In the latter case, the change of resistance in the non-volatile RS is semi-permanent. This means that the system does not return completely to the initial state after the electric excitation is terminated. This behavior is observed in simple (TiO_2, NiO, CuO, HfO_2, and Ta_2O_5 [Waser et al. (2009); Waser and Aono (2007); Wong et al. (2012); Inoue and Rozenberg (2008); Ielmini (2016)]) and more complex ($YBa_2Cu_3O_{7\text{-x}}$, $SrTiO_3$ [Waser et al. (2009); Sawa (2008); Imada et al. (1998); Szot et al. (2006)]) oxides. Depending on whether the system keeps memory or not, its use can be more appropriated for synaptor or neuristors. Note that the characteristic times scales of the volatile switching potentially could be several orders faster

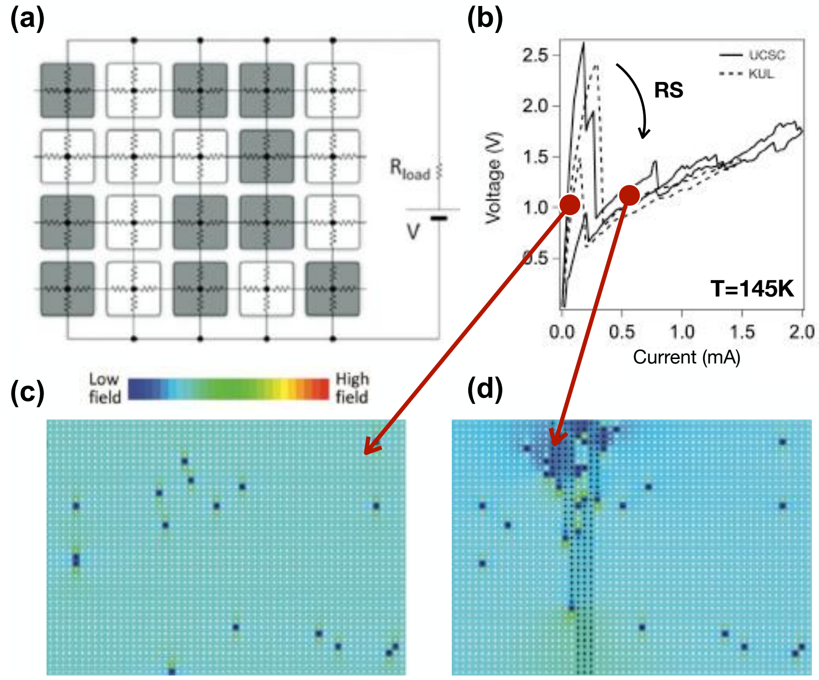

Figure 1.5: **The resistor network model.** (a) Typical resistor network configuration used for simulations of resistive switching in Mott materials. Each cell can be either metallic or insulating (black and white). Adapted from [del Valle et al. (2018).] (b) I-V curve showing volatile RS in V_2O_3 at T = 145K. The dashed line corresponds to a 2-points I-V measurement performed at KU Leuven (KUL) on a 2 μm gap device, the solid line corresponds to a 2-points I-V measurement performed at Universitá Cattolica del Sacro Cuore (UCSC) on the same device. Similar results are obtained. (c) The resistance network before the resistive switching. A few metallic sites are created randomly due to the thermal excitation. (d) The resistive switching is associated with the formation of a filamentary metallic path between the bottom and top electrodes. In this case, the numerical results do not simulate the real behavior of the device shown in (b). Panel (c-d) are adapted from [Stoliar et al. (2017)] and are just used to explain the universal behavior of the breaking of the insulating state during the RS.

than the non-volatile switching.

It is immediately evident that the detailed study of the spatial and temporal dynamics of RS are of fundamental importance for understanding the physics of these materials and the application of these concepts in a neuromorphic network. Along with numerous experimental studies, valuable help comes from numerical models [Stoliar et al. (2013, 2017)]. Indeed, the resistor network model shown in Fig. 1.5 (a) was introduced to explain the universal volatile and non-volatile RS found in many TMOs. In this model, each

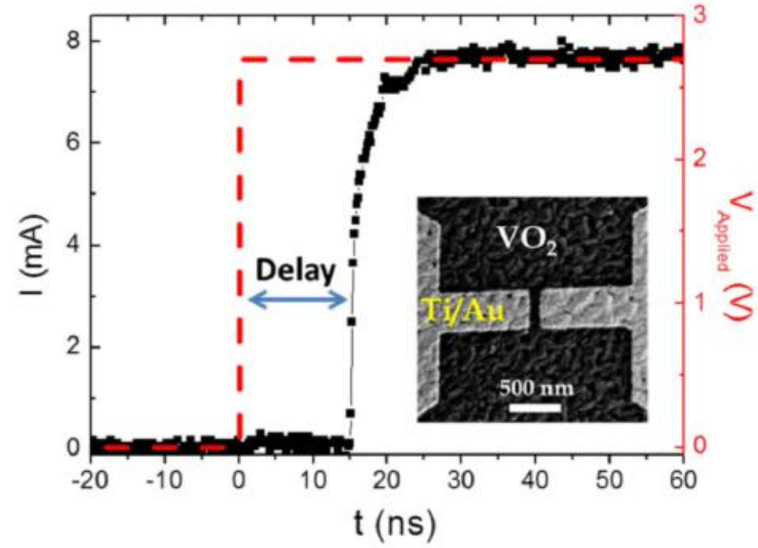

Figure 1.6: Current (left axis, black squared data) as a function of time when a voltage pulse is applied (right axis, dashed red line) to a VO_2 nanodevice (inset). Adapted from [del Valle et al. (2018, 2019)].

resistor of the network can be in one of two possible resistive state: a metastable low-resisitivty correlated metal (CM) or a stable high-resisitvity Mott insulator (MI) (Fig.1.5 (c)). The transition MI → CM can be driven by the action of a strong local electric field, that, above threshold, leads to the sudden growth of a filament that percolates through the electrodes (see Fig. 1.5 (d)).

Besides the nanoscale characteristics of the resistive switching process, another crucial aspect for applications is how fast the response to an external stimulus occurs. In fact, in the model of the resistive network for the case of a train of short electric pulses, the relaxation time and the temporal width of the pulses become important control parameters. Experimentally, it was observed that by changing the ratio between the time of two consecutive voltage pulses (frequency) and the duration of the excitation (width), it is possible to induce the RS after a different number of excitations, but without changing the low-voltage threshold [Stoliar et al. (2017)]. This is mainly due to the heat accumulation effect. In this respect, the parasitic capacitance and the large resistance of these materials in their insulating state play a fundamental role, and lead to RC constants of the order of ns [del Valle et al. (2018)]. This effect can be appreciated in Fig. 1.6 that shows results of a voltage pulse applied across a 100 nm Metal/VO_2/Metal structure. The transition does not take place immediately, but it takes

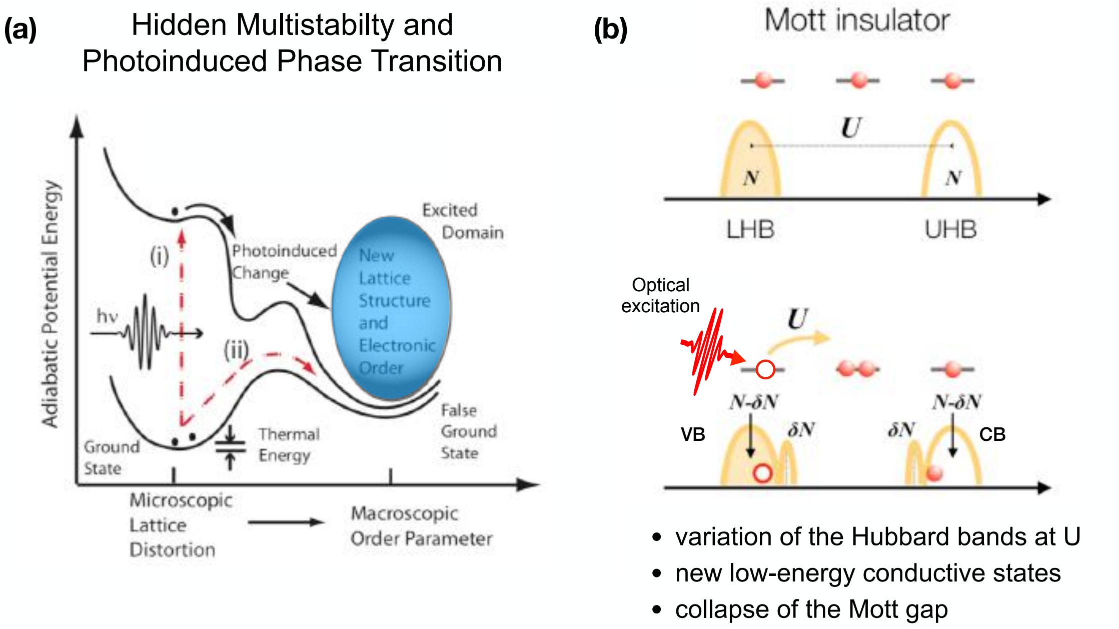
(a)
Hidden Multistabilty and Photoinduced Phase Transition
Adiabatic Potential Energy
(i)
(ii)
hν
Photoinduced Change
New Lattice Structure and Electronic Order
Excited Domain
Ground State
Thermal Energy
False Ground State
Microscopic Lattice Distortion
Macroscopic Order Parameter
(b)
Mott insulator
U
N
N
LHB
UHB
Optical excitation
U
N-δN
N-δN
VB
δN
δN
CB
• variation of the Hubbard bands at U
• new low-energy conductive states
• collapse of the Mott gap

Figure 1.7: **Photoinduced Phase Transiton in Mott systems.** (a) Depiction of a photoinduced phase transition showing the potential energy as a function of a generalized structural coordinate. Photoexcitation initiates a structural change which, in turn, drives an electronic phase transition with an order parameter different from that in the ground state. The energy barrier to obtain the new long-range (though likely metastable) ordered phase is greater than k_bT. The red dashed arrows labeled (i) and (ii) depict electronic and vibrational routes towards inducing a phase transition. Adapted from [Basov et al. (2011), previously shown in [Nasu (2004)]. (b) Cartoon of the photoexcitation process of a Mott insulator: the multiplicity of the upper-(UHB) and lower-Hubbard bands (UHB) is modified by the optical excitation and is compensated by the emergence of new conductive states at low energies. The basic consequence of this process is the injection of δN photoexcitations across the Mott gap, and thus the emergence of δN low-energy metallic-like states and the corresponding decrease of the spectral weight of electronic bands at the energy scale U. This represent the optically-induced collapse of the Mott gap. Adapted from [Ronchi et al. (2018)].

around 10 ns for the metallic phase to be induced [del Valle et al. (2018, 2019)] in this device configuration. In fact, in order to have the fastest temporal dynamics in the MIT, we must necessarily go for optically-induced transitions.

1.2.2 Photo-induced phase transition in Mott systems

Another approach to control and study Mott systems is the employment of out-equilibrium experimental techniques, for example, ultrafast pump-probe optical spectroscopies. The possibility to selectively excite specific electronic degrees of freedom unveiled a wealth of metastable states and transient "hidden" phases not apparent in the steady-state phase diagrams (see Fig. 1.7 (a)). The possibility of tuning material properties on sub-picosecond timescale led to a large number of experiments exploring photoinduced phase transformations. This huge amount of studies can be differentiated in three distinct categories, according to the "nature" of the phase transition or the final goal of the experiment [Giannetti et al. (2016)]:

1. *Photo-induced phase transition (PIPT) between quasi-equilibrium phases*, in which the light-driven transient state is already present in the equilibrium phase diagram, thus is well-defined by a thermodynamics potential.
2. *Photo-induced Transient Non-Equilibrium States (PINES)*, in which the the light-driven transient state is not present in the equilibrium phase diagram, thus no thermodynamics potential is defined.
3. *Coherent control of transient quantum phases*, in which the key point is to control on-demand the behavior of the system.

The main idea below these non-equilibrium approaches can be easily understood by noting that in correlated materials, the bandstructure intrinsically depends on the band occupation, which can be non-thermally manipulated by light. Consider the simplest case of a two-band insulator in which the correlated half-filled valence band (v) and the conduction band (c) of different orbital origin are separated by a gap 2Δ. The effective gap thus takes into account that the v-band, corresponding to the LHB in the single-band Mott insulator, is pushed down in energy by a factor $U/2$ due to the strong onsite Coloumb repulsion. The effective band distance, $2\Delta_{eff}$ can be thus parametrized by the average occupation of each band [Ronchi et al. (2018); Sandri and Fabrizio (2015)]:

$$2\Delta_{eff} = 2\Delta + \frac{U}{2}(n_v - n_c) = 2\Delta + \frac{U}{2}\delta p \tag{1.1}$$

where δp represents the orbital polarization, defined as the difference between

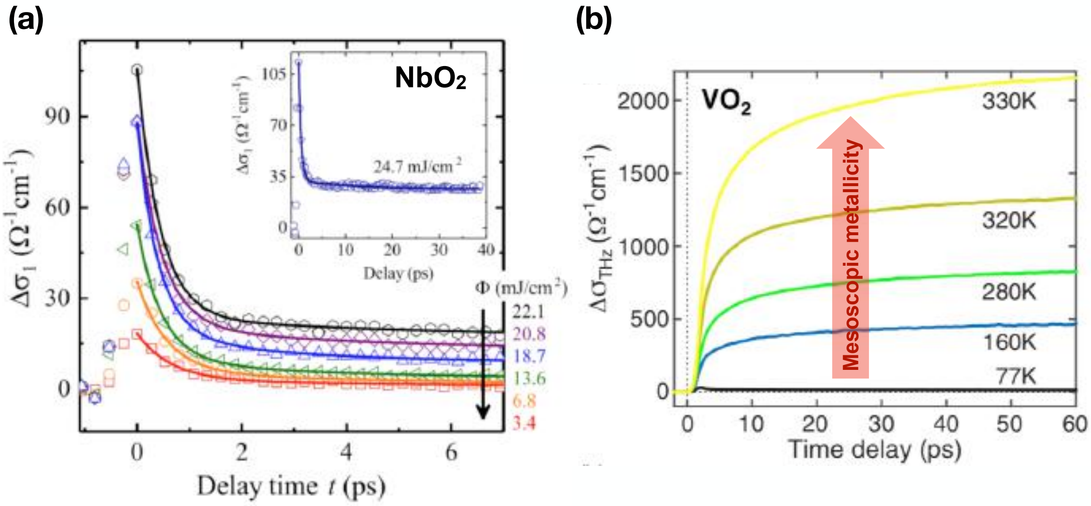

Figure 1.8: **Photo-induced insulator-to-metal transition in NbO$_2$ and VO$_2$.** (a) Spectrally integrated transient change of the THz conductivity $\Delta\sigma$ of a 190-nm-thick NbO$_2$ film as a function of the pump-probe delay time t for selected fluences at a substrate temperature of 295 K. (b) Transient $\Delta\sigma$ of a 75-nm-thick VO$_2$ film for temperatures below the IMT temperature at 800 nm (1.55 eV) pump fluence of 3.8 mJ/cm^2. Despite of the fast peak in NbO$_2$, in both materials, it is possible to observe a long-live (tens of picoseconds) THz response and a conductivity increase which corresponds to the IMT. Panel (a) adapted from [Rana et al. (2019)], panel (b) adapted from [Abreu et al. (2017)].

the average occupation densities in the valence (n_v) and conduction (n_c) bands. It is evident that the orbital polarization δp plays a crucial role in determining the electronic properties of multi-band correlated materials and in the possibility to control on-demand the system by means of ultrashort laser excitation [Tokura (2006); Giannetti et al. (2016); Ronchi et al. (2018)] (see Fig. 1.7 (b)). In this scenario, an ultrafast optical pulse with photon energy $\sim U$ can induce the collapse of the Mott gap and transiently bring a Mott insulator to a metastable metallic state [Sandri and Fabrizio (2015)]. As an example, one interesting result reported recently is the transient photo-creation of possible room-temperature superconductivity in cuprate and C$_{60}$-based superconductors [Hu et al. (2014); Mitrano et al. (2016)].

More specifically, the photo-induced Insulator-to-Metal transition has been observed by means of time-resolved 1.5 eV pump-terahertz (THz) probe spectroscopic studies. The THz pulses (0.1 - 2.5 THz) can effectively probe the low-energy Drude response and hence the conductivity of the material. This approach has been successfully applied to many TMOs, including NbO$_2$ [Rana et al. (2019)], SmNiO$_3$ [Torriss et al. (2018)] and VO$_2$ [Abreu et al.

(2017)]. In Fig. 1.8 we report transient optical conductivity $\Delta\sigma$ measured in (a) NbO_2 and (b) VO_2. In both cases, similar trends are observed. Above a certain (a) fluence threshold or (b) in vicinity of the transition temperature, the emergence of a longstanding (tens of picoseconds) dynamics in the optical conductivity $\Delta\sigma$ indicates the formation of a percolative-network of metallic domains and a metastable metallization of the systems. This means that a Photo-induced Phase Transition (PIPT) has occurred. A crucial point concerns the speed of the IMT, which is of the order of picoseconds with respect to the nanoseconds in the previously mentioned electrically induced transition. The innovative idea to combine optical and electrical excitation on a Mott device can open new intriguing scenarios where the RS is driven by ultrafast laser pulses with the final aim of controlling them at THz frequencies in a non-thermal way. However, before proceeding with such an ambitious project, it is appropriate to thoroughly understand the spatial and temporal dynamics of the photo-induced Metal-to-Insulator transition and of the electrical switching.

1.3 Probing the dynamics of the Mott transition

Ultrafast spectroscopies can be an extraordinary tool to unveil the physical behavior of the thermally, electrically and optically driven Mott transition. In particular, in this section we discuss and present some examples of the possibility of using ultrafast techniques to investigate the temporal and spatial dynamics of the MIT in correlated TMOs.

During the MIT, the interplay between the charge, lattice, spin, and orbital Degree of Freedom (DOF) is very strong, and defines the macroscopic properties of the system and its equilibrium phase diagram. Understanding the competing mechanism between different DOF is therefore of extraordinary relevance for the control of these materials on ultrafast time scales. Within this contest, the Metal-to-Insulator transition in vanadates can be considered as a paradigmatic case of study even if many other transition oxide families from manganites to iron oxides have shown similar behavior [Giannetti et al. (2016)]. For instance, in VO_2 the electronic Insulator-to-Metal Mott transition driven by Coulomb repulsion is accompanied by a structural phase transition from a low-temperature monoclinic M_1 phase to a high-temperature rutile R phase at $T_C \sim 340$ K. During this hysteretic first order phase change, a coexistence between the two phases is observed. This aspect is due to the nucleation and growth of

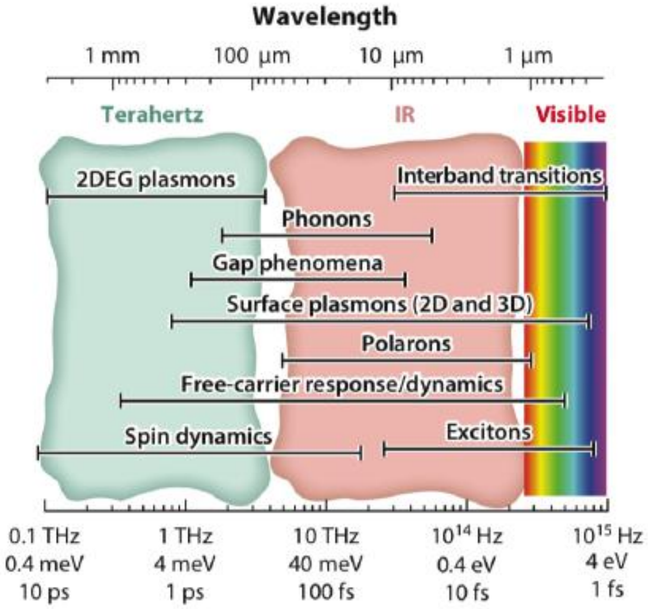
Wavelength
1 mm
100 µm
10 µm
1 µm
Terahertz
IR
Visible
2DEG plasmons
Interband transitions
Phonons
Gap phenomena
Surface plasmons (2D and 3D)
Polarons
Free-carrier response/dynamics
Spin dynamics
Excitons
0.1 THz
0.4 meV
10 ps
1 THz
4 meV
1 ps
10 THz
40 meV
100 fs
10¹⁴ Hz
0.4 eV
10 fs
10¹⁵ Hz
4 eV
1 fs

Figure 1.9: Fundamental excitations and corresponding energy and timescales for TMOs. Adapted from [Zhang and Averitt (2014)].

metallic nanodomains in an insulating template. Despite intensive studies during the past fifty years, the microscopic nature of this phase transition has been subject to considerable debate, and precisely the question is whether the transition is determined by Mott physics (electronic) or by the Peierls mechanism (structural). In particular, the Peierls distorsion is a mechanism that allows a one-dimensional metallic chain to spontaneously become an insulator by doubling the periodicity. It is clear how finding ultrafast techniques capable of probing (a) the electronic state, (b) the crystalline structure and (c) the spatial inhomogeneities at the nanoscale during the IMT is of fundamental importance to address the problem of the mechanisms leading to the phase transition in VO_2, as in all those systems that show similar features.

Concerning the dynamics of the electrons in the system, ultrafast optical spectroscopy plays a fundamental role since it can spectrally access all the relevant excitation processes (inter- and intraband transitions, electron-phonon coupling, plasmons, magnons, etc...see Fig. 1.9). The response of the systems (under perturbation) in terms of changes of the optical properties is huge [Basov et al. (2011); Dressel and Grüner (2002)]. The main idea behind this kind of ultrafast experiments is to excite a sample with a short

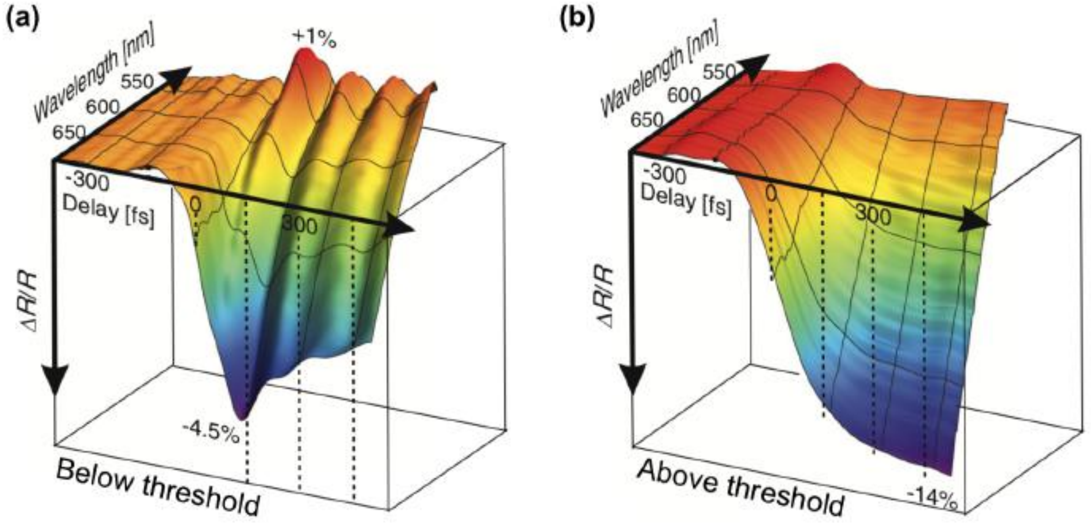

Figure 1.10: **Ultrafast optical pump-probe spectroscopy in VO_2**. Broadband reflectivity change, measured at room temperature (a) below the photoinduced IMT transition threshold pumping and (b) above. The transient decay to the steady state can give important information about the electronic dynamics during the MIT. In addition, below threshold, coherent phonons are observed in all frequency range. Nevertheless, these oscillations are more evident for wavelengths below 550 nm demonstrating how the tuning of the probe energy can facilitate the observation of a particular physical effect. Above threshold, the active phonon modes disappear due to the optical induced change in the lattice potential. Adapted from [Wall et al. (2012)].

pump pulse (10 fs-1 ps) then following the subsequent relaxation dynamics with a second delayed probe pulse. This relaxation process, measured at the fundamental timescales of the electronic and atomic motions, contains useful information to disentangle DOF competition and interaction, that cannot be obtained in a standard equilibrium approach. Therefore, the main control parameters in all these out-equilibrium experiments are the photon energy of the pump and probe pulses. By tuning these energies from visible to mid-IR or terahertz is it possible to select a mode-selective excitation and follow a particular relaxation path. Fortunately, during the past decades, many works including ultrafast optical studies of semiconductors and metals have laid the foundation for understanding free-carrier effects, electron-phonon coupling, spin dynamics, exciton dynamics, and coherent phonons [Zhang and Averitt (2014); Giannetti et al. (2016)]. Fig. 1.10 shows the transient reflectivity in VO_2 measured using 800 nm (1.55 eV), 40 fs pump and a broadband supercontinuum probe at room temperature. Above threshold, the large decrease in reflectivity induced by the pump pulse occurring in hundred femptosecond time scale is followed by a slow response revealing

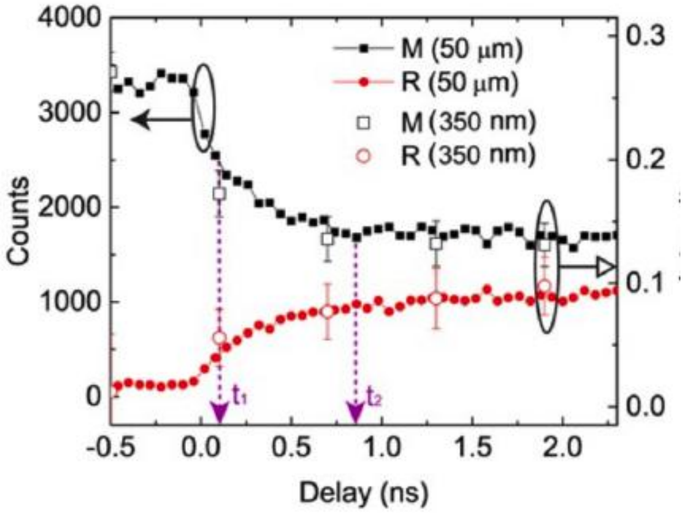

Figure 1.11: **Time-resolved X-ray Diffraction (XRD) spectroscopy in $\mathbf{VO_2}$.** Bragg reflection intensities of the $40\bar{2}$ monoclinic (M) and 002 rutile (R) phases as a function of delay, measured with a 50μm (Full Width at Half Maximum (FWHM)) x-ray beam (filled symbols) and with a 350 nm X-ray beam with a pump fluence above the threshold to induce the IMT. Adapted from [Zhu et al. (2016)].

that highly photo-excited VO_2 reaches a metallic state immediately after photo-excitation. The photo-excited transient reflectivity change is therefore a direct probe of the electronic properties of the sample. Below the IMT threshold, the decay dynamics is faster with clear oscillations superimposed. The oscillations are the result of the excitation of coherent M_1-phase phonon modes. These are due to a rapid redistribution of the electron charge density that causes the ions to displace from their equilibrium positions. As demonstrated, by tuning probe photon energy, pump fluence and pump-probe temporal delay it was possible to access an entire set of information related to the electronic dynamics during the IMT transition in VO_2. In addition, the study of coherent oscillations permits to even acquire useful information about the change in symmetry of the lattice potential.

Nonetheless, the use of techniques which can directly probe the crystalline structure of the materials turned out to be very useful. Time-resolved X-rays diffraction (Tr-XRD) [Zhu et al. (2016)], time-resolved X-Rays scattering [Wall et al. (2018)] or time-resolved electron diffraction [Baum et al. (2007)] are possible and reasonable paths to investigate the structural changes during the IMT transition. For instance, using a newly developed laser pumped X-ray diffraction imaging technique with 350 nm spatial resolution and 100 ps temporal resolution, Zhu et al. (2016) investigated the structural phase propagation during the photo-induced phase transition in a VO_2 thin film (see Fig. 1.11). Time-resolved mapping of the real-space structural transformation is captured by tracking signatures of the structural phases in the reciprocal space. From these results, a three-steps picture is evident. The first step is the initial symmetry change at nucleation sites on the unit-cell level on fs time scales due to the absorption of the optical pump excitation. The second step is a process in which the lattice is superheated above the transition temperature within a few ps, as a result of electron-phonon coupling. Finally, the lattice symmetry change propagates from the nucleation site in a domino-like effect due to a displacive lattice transformation (hundreds of picoseconds). This experiment was therefore able to follow the dynamics of the structural transition in VO_2.

Finally, as previously said, phenomena such as IMT are often characterized by the spontaneous appearance of spatially separated regions with distinct structural, magnetic, and electronic properties. Therefore, the extreme importance of the microscopic situation during the IMT has inspired efforts to extend the strategy of local probes to electrical, optical, magnetic, dielectric, and chemical phenomena at ultrahigh spatial resolution. Indeed, understanding complex phenomena at the nanometer scale not only pushes frontiers of fundamental physics, but is a prerequisite to next-generation applications in electronics, sensing, energy harvesting, and more. Techniques as Atomic Force Microscopy (AFM), Scanning Tunneling Microscopy (STM), Scattering Scanning Near-field Optical Microscopy (s-SNOM), PiezoForce Microscopy (PFM), PEEM, and more, have been used to investigate the nanoscale behavior in TMOs [Bonnell et al. (2012)]. In Fig. 1.12 (a) a snapshot is reported of insultating and metallic domains in $NdNiO_3$ obtained by means of PEEM. In this particular case, the approach followed allowed to reconstruct the hysteresis cycle by calculating the filling fraction of the metallic phase within the insulating one [Mattoni et al. (2016)], measuring the nucleation, growth and percolation dynamics. In panel (b), B. T. O'Callahan performed nano-infrared s-SNOM to probe the Drude dieletric responce of VO_2 microcrystals on heating and cooling through the IMT, with $\sim$ 10 nm resolution. This microscopic study has been accompained by pump-probe optical spectroscopy investigating the temporal dynamics in many individual single crystals with different dimensions. They concluded that, even on the individual-crystal level for nominally homogeneous VO_2 single crystals, a highly inhomogeneous IMT behaviour was observed, with different temporal dynamics. This confirms how spatial inhomogeneities can also affect temporal dynamics. In the next years, the effort to combine

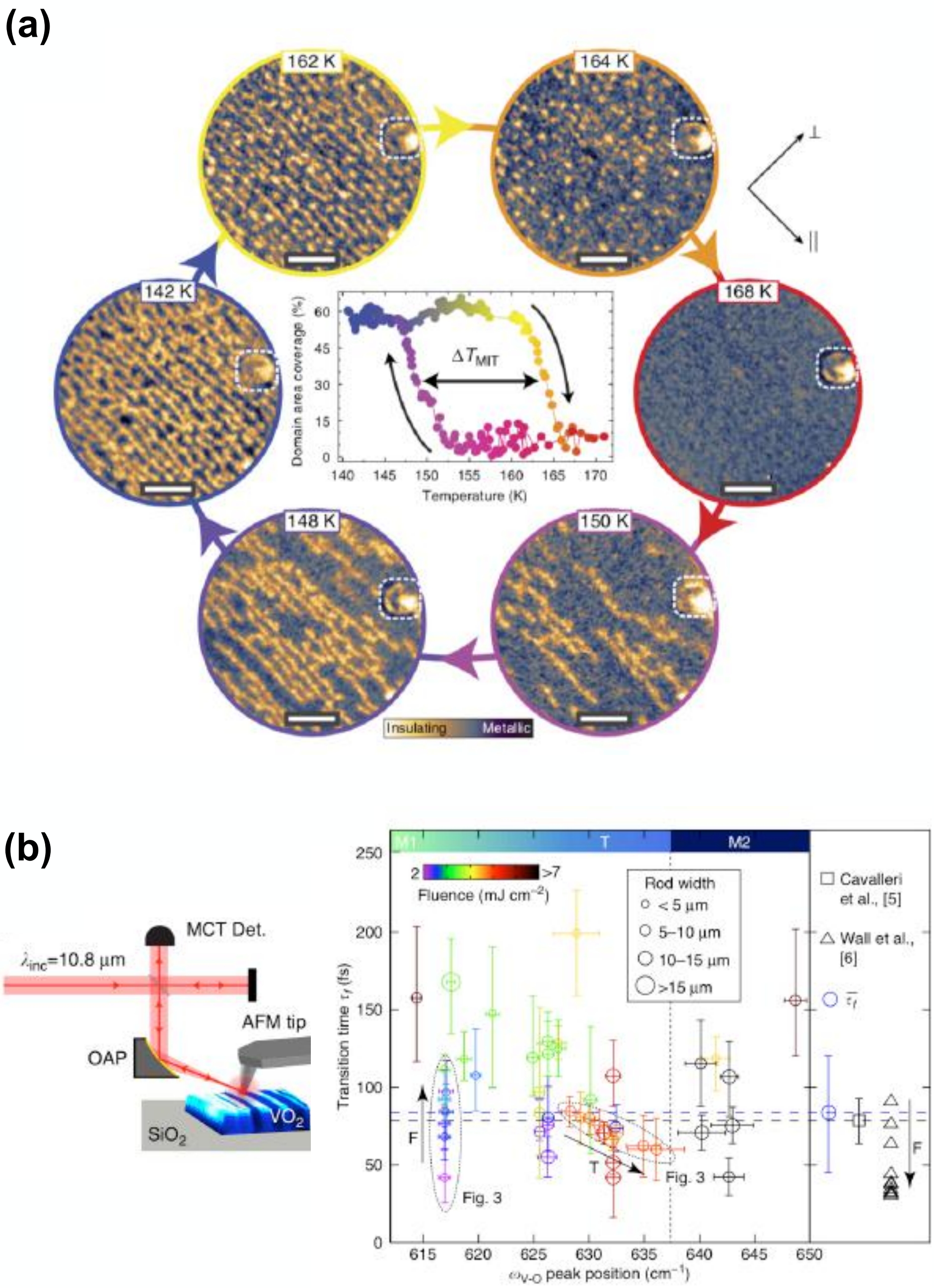

Figure 1.12: **Nanoimaging of the IMT**. (a) Nucleation and growth of metallic domains during the thermal cycle in $NdNiO_3$. Images obtained by means of PEEM. (b) Left: Schematic of Drude response s-SNOM. When heating VO_2 microcrystals through the insulator-to-metal transition, these form alternating metallic (bright) and insulating (dark) domains perpendicular with respect to the c_R-axis to minimize substrate strain. Right: Photoinduced transition time τ_f, plotted against initial ambient insulating phase, represented by the frequency of the Raman mode ω_{V-O}. Colour bar at top shows corresponding insulating phases. Symbol size reflects microcrystal width, from < 5 μm, to > 15 μm. Panel (a) is adapted from [Mattoni et al. (2016)], panel (b) is adapted from [O'Callahan et al. (2015)].

these imaging techniques with ultrafast optical spectroscopy will certainly pave the way for new pathways to understanding Mott's physics in TMOs.

Chapter 2

V_2O_3: Prototype for the Mott transition

2.1 Metal-to-Insulator in V_2O_3

2.1.1 Phase diagram

Vanadium sesquioxide (V_2O_3) has been widely studied as a prototype for the MIT from the seventies up to nowadays [Lantz (2015)]. With more than 700 papers published is considered a unique theoretical and experimental platform for the understanding of the mechanism lying under the Mott transition [Mott (1990); Hansmann et al. (2013)]. McWhan et al. (1969) were the first one able to grow and to characterize with resisitivity and XRD measurements a high-quality single crystal of $(V_{1\text{-}x}Cr_x)_2O_3$. In particular, they observed a drastic change in resistivity of six orders of magnitude at 180 K for the undoped compound (see Fig. 2.1 (a)). This metal-to-insulator transition was completely quenched by introducing a ∼5% doping with Ti atoms. On the other hand, a 1% doping with Cr was sufficient to unveil a RT insulating phase. Further investigations has permitted D. B. McWhan and P. Hansmann to completely reconstruct the phase diagram, shown in Fig. 2.1 (b). As it is possible to observe, V_2O_3 is a paramagnetic (correlated) metal (PM) in standard condition (p = 1 atm at RT), with a resisitvity of about 10^{-3} Ω cm. At T = 150 K, there is a breaking of the crystal symmetry from rhombohedral to monoclinic and the system becomes an antiferromagnetic insulator AFI through a MIT. Strikingly, it is still object of strong debates

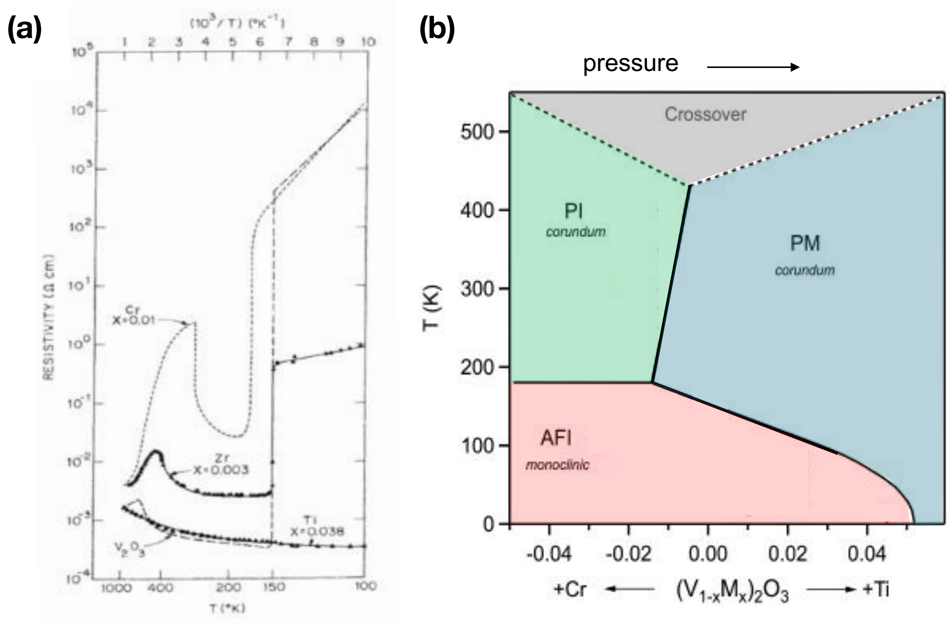

Figure 2.1: **Phase diagram of $(V_{1\text{-}x}Cr_x)_2O_3$ bulk** (a) Comparison of the electrical resisitvity perpendicular to the c-axis versus temperature for different dopants and doping. Adapted from [McWhan et al. (1973)]. (b) Generalized phase diagram for the metal-to-insulator transition in V_2O_3 as a function of doping with Cr or Ti and as a function of pressure. The metal-insulator boundary terminates at the critical point. Adapted from [Hansmann et al. (2013)].

if this temperature-driven transition is dominated by the strong electronic correlations or, viceversa, by the lattice distortion, and in particular, we will discuss this aspect later on in Sec. 2.2.3. Nevertheless, when V_2O_3 is doped with Cr, the system crosses from PM to the Paramagnetic insulator (PI) for a 1% Cr doping at 300 K, without any change in the crystal structure. This phase change is the true Mott transition, and for this reason V_2O_3 is considered a good candidate to explore the still hidden nature of the Mott physics in multi-orbital systems. A phase coexistence between PI and PM phases, called the crossover region, is present above the critical point at around 400 K. This critical point follows the universal properties of a liquid-gas transformation [Limelette et al. (2003)].

2.1.2 Crystal structure

The V_2O_3 crystal structure in the different phases was resolved in the seventies [McWhan et al. (1969); McWhan and Remeika (1970); McWhan

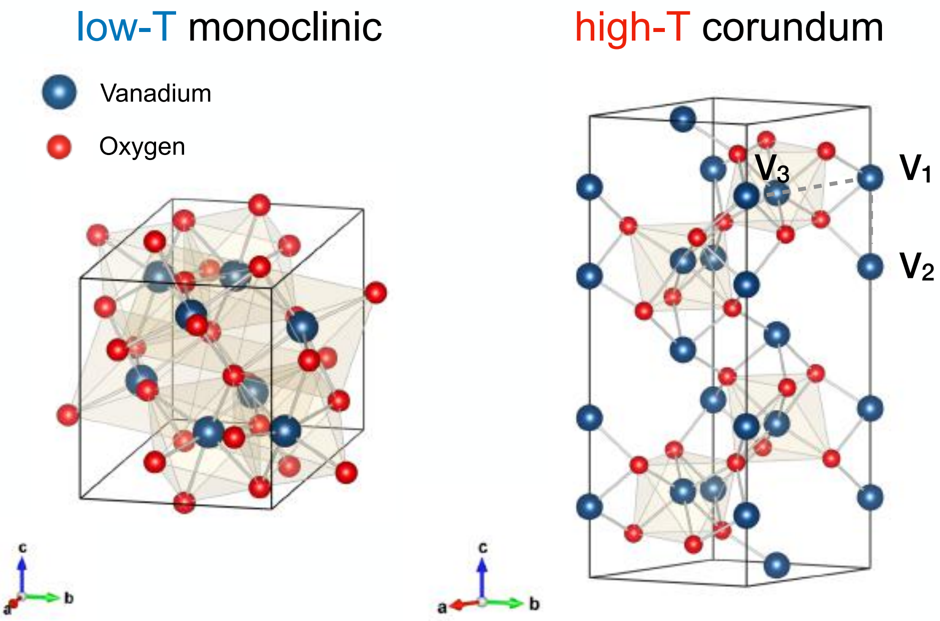

Figure 2.2: **Crystal structure of V_2O_3.** Crystal lattice unit cell for the monoclinic and corundum phases. The software used to build the crystal structures is VESTA. The atoms positions are taken from Ref. Dernier and Marezio (1970).

et al. (1973); Dernier and Marezio (1970)]. In the high-temperatures Paramagnetic Insulating (PI) and Paramagnetic Metallic (PM) phases the compound has a corundum crystal structure (see Fig. 2.2) and a symmetry space group R$\bar{3}$c (group number 167). The typical unit cell considered is hexagonal with 18 oxygen atoms and 12 vanadium atoms. If we consider just the vanadium atoms, the high-temperature corundum lattice consists of shifted honeycomb planes stacked along the c-axis. The low-temperature monoclinic antiferromagnetic phase (symmetry group I2/a, group number 15) is the result of breaking the hexagonal symmetry, associated with the elongation of two edges of the hexagons (V_1-V_3), which leads to an overall increase of the unit-cell volume by 1.4% [McWhan and Remeika (1970); Dernier and Marezio (1970)]. The breaking of the hexagonal symmetry is accompanied by a tilt of the hexagons with respect to the honeycomb planes, which increases the distance of the V_1-V_2 dimers along the c-axis, without further affecting the unit-cell volume. The more insulating the material gets, the larger the distance V_1-V_2 is. The lattice parameters in PI, PM and AFI phases are reported in Table 2.1.

	Phase	**T**(K)	**a**(Å)	**b**(Å)	**c**(Å)	$\mathbf{V_1}$**-**$\mathbf{V_2}$ (Å)	$\mathbf{V_1}$**-**$\mathbf{V_3}$ (Å)
V_2O_3	PM	300	4.951	4.951	14.001	2.700	2.872
V_2O_3	AFI	100	5.548	5.002	7.255	2.745	2.987
$(V_{0.962}CrO_{0.038})_{23}$	PI	300	4.991	4.991	13.912	2.745	2.914

Table 2.1: Lattice parameters and V-V nearest neighbour distance for V_2O_3 taken from Ref. Dernier and Marezio (1970).

2.1.3 Electronic structure

The low-energy physics of vanadium sesquioxide (V_2O_3) originates from the interactions between the two electrons occupying the V 3d levels and from their coupling to the crystal lattice distortion. In particular, the octahedral crystal field splits the V 3d orbitals into lower t_{2g} and upper e_g bands. Since the octahedra display a further trigonal distortion, strengthened by the on-site Coulomb repulsion (U $\simeq$ 2.5 eV[Qazilbash et al. (2008)]), the t_{2g} orbitals are split (see Fig. 2.3 (a)) in turn into a lower e_g^π doublet, mainly oriented in the a-b plane, and an upper a_{1g} singlet. In the low-T AFI monoclinic phase, the average occupancy of e_g^π orbitals ($n_{e_g^\pi} \simeq 0.83$) largely overcomes that of the a_{1g} level ($n_{a_{1g}} \simeq 0.17$) and the system behaves as a half-filled two-band Mott insulator [Park et al. (2000)] with an effective charge gap of $2\Delta_{eff} \simeq 0.5$ eV [Qazilbash et al. (2008)]. At $T_{IMT} \sim 160$ K, the first-order structural change from monoclinic to corundum, which implies an increase of crystal symmetry and a reduction of the unit-cell volume, accompanies a jump of the a_{1g} occupation with a concomitant transition to the PM phase, characterized by $n_{a_{1g}} \simeq 0.25$ [Park et al. (2000)]. In 2000, Park et al. (2000) performed X-rays absorption spectroscopy and discovered that vanadium atoms are in a spin S = 1 state with the $e_g^\pi e_g^\pi$:$e_g^\pi a_{1g}$ occupation ratio varying from 2:1 in the AFI, 1:1 in the PM, and 3:2 in the PI phase.

The numerous experimental measurements were accompanied by as many theoretical works using LDA+DMFT calculations that really refined the understanding of the V_2O_3 electronic structure [Poteryaev et al. (2007); Anisimov et al. (2005)] (see Fig.2.3 (b)). In particular, they showed that the trigonal distorsion is the real responsible for the MIT, while the Coulomb repulsion is substantially constant. Hard X-ray photoemission have verified and confirmed these theoretical results [Fujiwara et al. (2011)]. Another phenomenon predicted by theory and then confirmed by experiments is the presence of a strong Quasiparticle Peak (QP) close to the Fermi energy in the metallic phase. High energy photoemission spectroscopy experiments [Mo

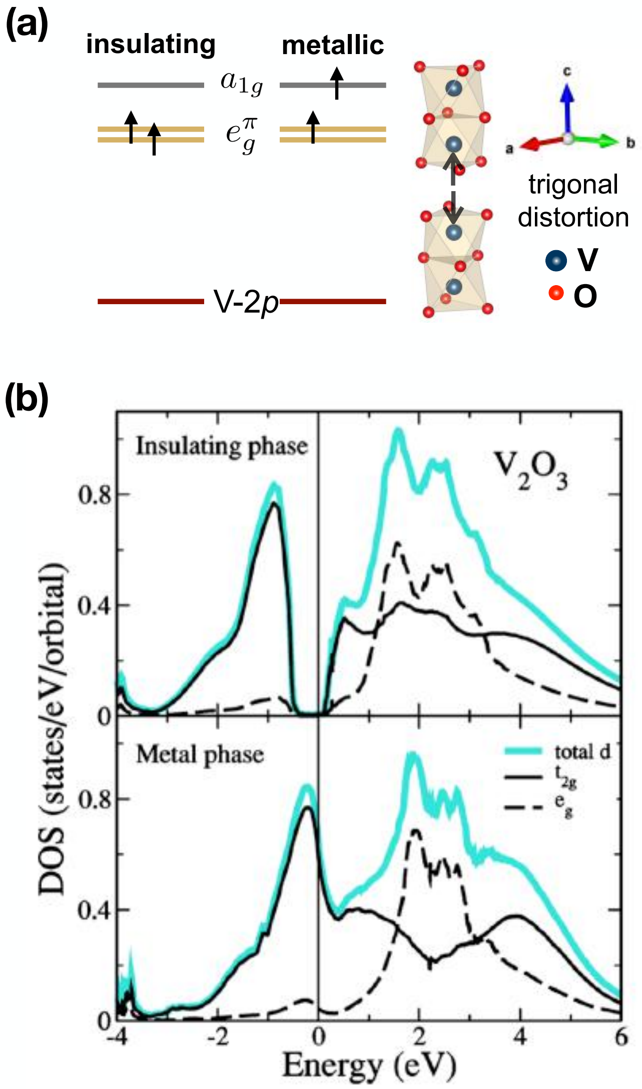

Figure 2.3: **Trigonal distorsion of the octahedra and Density of States (DOS) in V$_2$O$_3$** (a) Trigonal distortion of the V atoms along the c-axis of the hexagonal unit cell indicated by the arrows. The doubly occupied V t$_{2g}$ levels are further splitted into a$_{1g}$ and e$_g^\pi$. (b) Partial V-3d DOS for V$_2$O$_3$ calculated using full-orbital self-energy from Local Density Approximation (LDA)+Dynamical Mean-field Theory (DMFT) Total d-full light blue line; t$_{2g}$-full black line; e$_g$-dashed black line. The Fermi level corresponds to zero. Panel (a) adapted from [Ronchi et al. (2019)], Panel (b) adapted from [Anisimov et al. (2005)].

et al. (2003, 2004, 2006); Papalazarou et al. (2009)] and optical conductivity measurements [Qazilbash et al. (2006, 2008, 2011)] corroborated even this aspect.

2.2 Dynamics of the Metal-to-Insulator transition

2.2.1 Spatial inhomogenities and phase coexistence

The investigation of spatial inhomogeneities during the MIT transition is of fundamental relevance since in V_2O_3 both termally-driven PM → AFI and pressure/doping-driven PM → PI transformations are first-order transitions with phase coexistence between metallic and insulating nanodomains. However, until a few years ago, the matter was poorly studied even if the spatial scale on which such transitions develop play a fundamental role for academic research and technological applications. In fact, beyond the intrinsic usefulness of studying how spatially the transition takes place in micro- and nanodevices, the use of high-resolution local probes in contrast to spatially integrated techniques can reveal key aspects to unveil the competing mechanism between SPT and MIT. In this section we present two milestones for the study of spatial inhomogeneities in V_2O_3, and we will discuss the still open questions. In particular, the first work concerns the investigation of the "true" Mott electronic transition driven by pressure or doping between PM and PI phases, in which no structural change occurs. The second work investigates the spatial dynamics of the thermally-driven transition between the corundum PM and the monoclinic AFI phases.

In 2010, S. Lupi and co-authors investigated for the first time the real-space behavior of MIT in Cr-doped V_2O_3 adopting Scanning Photoemission Microscopy (SPEM) with sub-micron spatial resolution [Lupi et al. (2010)]. In particular, they discussed the case of $(V_{0.989}Cr_{0.011})_2O_3$, which retains the same corundum crystal structure when transforming from metal to insulator with just a slightly discontinuity of the lattice parameters. The choice of x=0.011 Cr doping is of great interest since it permits to span all the three phases just by changing the temperature of the system [McWhan et al. (1969)]. They found unambiguous evidence of an electronic phase separation in the thermally-induced PM phase. The maps of the photoelectron yield at Fermi energy E_F are plotted in Fig. 2.4 together with representative photoemission spectra obtained with 27 eV photon energy. At 220 K, in the PM state, the coexistence of insulating and metallic domains is observed (Fig.

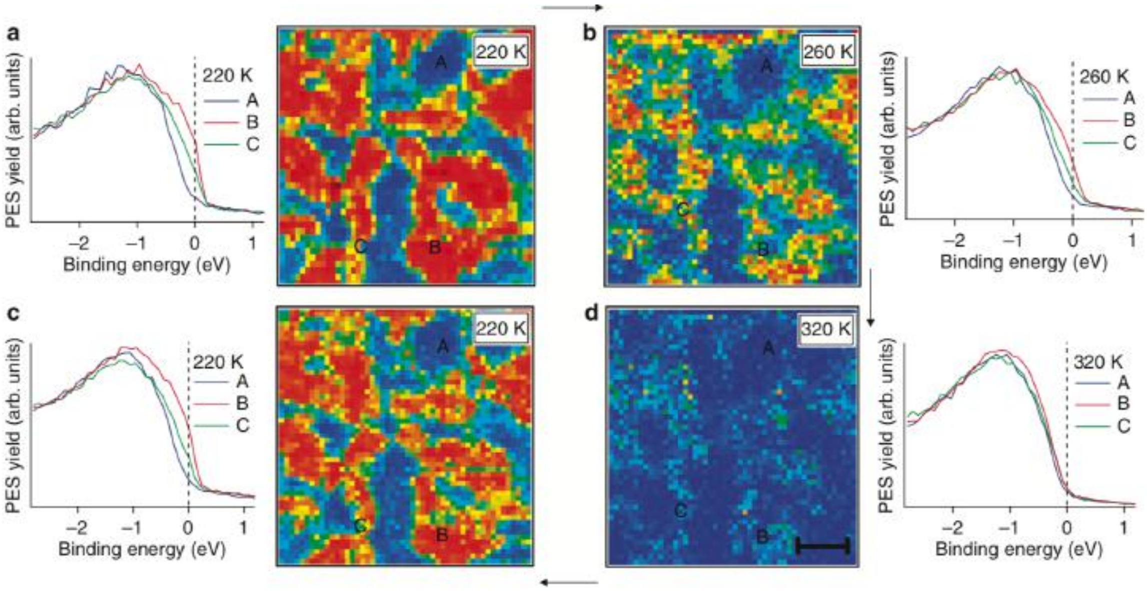

Figure 2.4: **Scanning photoemission microscopy of 1.1% Cr-doped V_2O_3**. Panel (a) and (c): Images taken in the PM phase at 220 K before (a) and (b) after thermal cycle. Phase coexistence of metallic (red) and insulating (blue) nanodomains is observed. The domain shapes are always pinned in the same position. By warming the sample a IMT from PM to PI occurs, and slowly the metallic domains are reduced (b) and, consequently, disappear (d). Adapted from [Lupi et al. (2010)].

2.4 (a)), with typical size of tens of microns. They are weakly connected, and this is reflected in the absence of a Drude-like contribution in the far infrared optical conductivity $\sigma_1(\omega)$ [Lupi et al. (2010)]. Note that the completely homogeneous metallization is obtained when external pressure is applied to the thin film. By increasing the temperature, those metallic domains are melted till in the fully PI phase, above 320 K, a completely homogeneous insulating background is shown (Fig. 2.4 (d)). Furthermore, when the sample is cooled down again (Fig. 2.4 (c)), the metallic and insulating domains are still found in the same position and with a similar shape. This observation indicates a pinning of the domains around some particular nucleation centers probably related to microscopic structural defects.

Another interesting work focused on the investigation of the thermal dynamics of the MIT between the PM and AFI phases [McLeod et al. (2016)]. Indeed, in this case there is also a structural transition. Part of the article is in fact dedicated to the discussion of whether Mott's transition and the SPT are coupled or not, but this will be discussed later

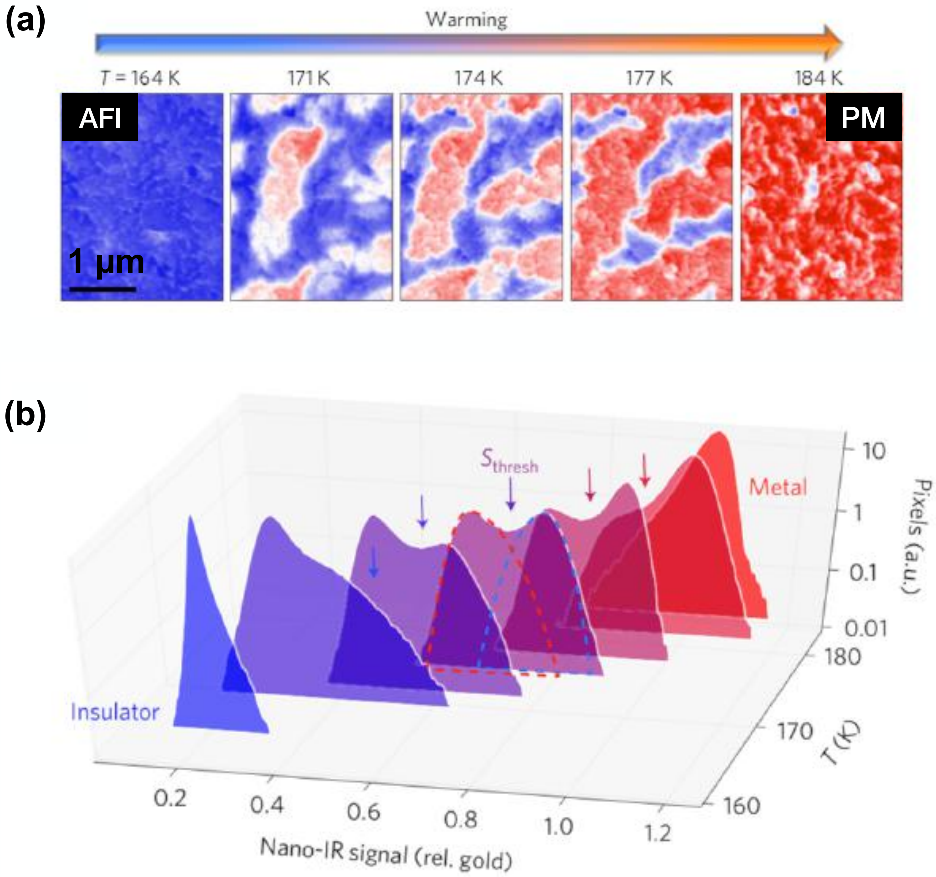

Figure 2.5: **Infrared near-field microscopy of V_2O_3.** (a) and Real-space snapshots of the IMT showing coexistence of insulating (blue) and metallic (red) nanodomains. Note that the low temperature phase AFI phase appears to be completely homogeneous. (b) Histograms of the Nano-IR signal with the two color distributions. The hysteresis loop has been calculated by counting the number of pixels corresponding to a particular phase with respect to the total. The transition temperature has been indicated as the temperature where the two distributions have equal number of pixels. Adapted from [McLeod et al. (2016)].

in Sec. 2.2.3. Concerning the imaging of the IMT, they developed cryogenic infrared near-field (nano-IR) spectroscopy (25 nm resolution) to assess nanoscale phase inhomogeneity thus revealing a spontaneous real-space nanotexture composed by alternating metallic and insulating nanodomains. In Fig. 2.5 (a), it is shown a set of images extracted from the warming cycle and measured with $\sim 11\ \mu$m wavelength. Therefore, this infrared spectroscopy is mainly probing the free-carrier Drude response, or the mesoscopic metallization occurring during the IMT. In particular, in the color scale, red areas indicate the metallic state while the blue ones are insulating. The characteristic size of these nanodomains is about a few hundreds of nanometers with sharp domain walls. The images also show a bi-directional orientation of the stripes due to the monoclinic distorsion, that are more evident in images with lower magnification. Nevertheless, a third crystallographic twin is expected but unobserved in their images. The reason of the missing twin is probably due to a cut of the (012)-Al_2O_3 substrate, which does not allow to appreciate the third monoclinic distortion happening in the (001)-plane. This point is still to be addressed and a dedicated discussion will be given in the next chapter when our results will be shown. In this work, the authors reconstructed even the hysteretic behavior of the MIT by calculating the percentage filling fraction of the metallic area (i.e. the number of pixels associated to the metallic nano-IR signal, see Fig. 2.5 (b)) and obtaining a 6 K hysteresis. It is important to note that the evolution of the phase transition passes from a *homogeneous* insulating to a *homogeneous* metallic phase.

Interestingly, some questions still had to be addressed. First of all, no nano imaging work probing the monoclinic structural deformation in the insulating phase has been published yet. In fact, there is no evidence in literature up to now of real-space inhomogenities in the low-temperature phase. Secondly, a complete study describing how the transition takes place both spatially and temporally starting from the nucleation of the metallic seed, passing through growth and percolation up to a complete homogeneous metallic state, is still missing.

2.2.2 Temporal dynamics of the transition

Over the past decade, the temporal dynamics of the MIT transition in V_2O_3 has been extensively studied by time-resolved ultrafast spectrocopies. In 2011, the first work showing the possibility of thermally photoinducing

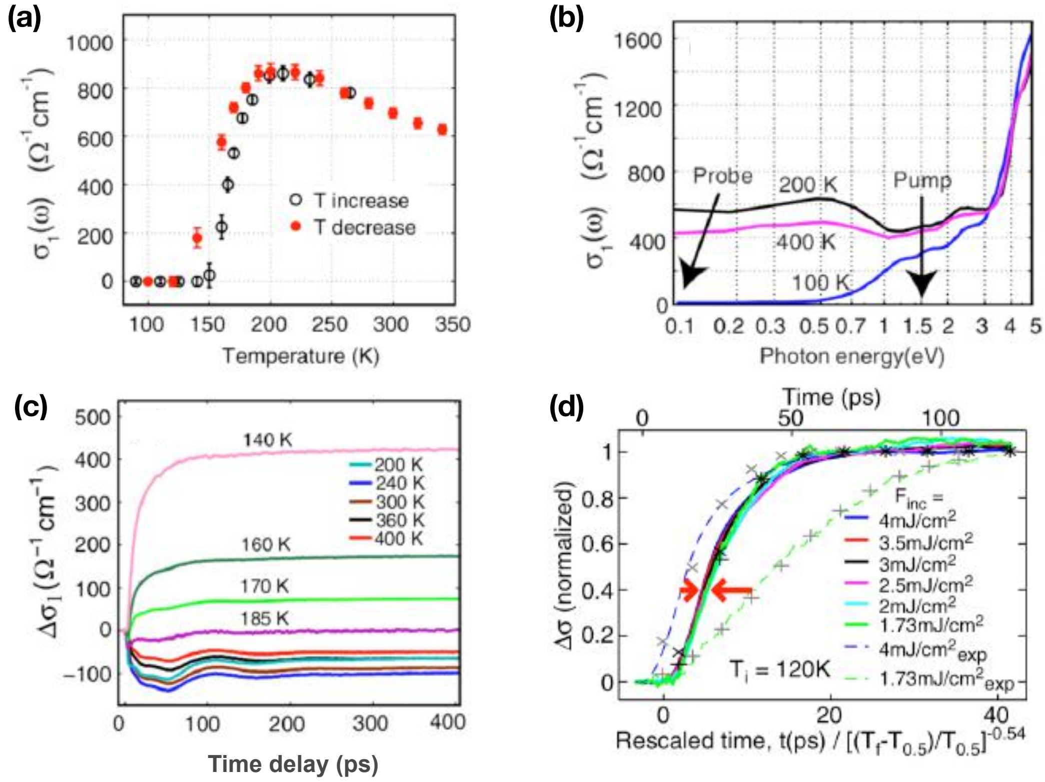

Figure 2.6: **Photoinduced Phase Transitions by Time-Resolved Far-Infrared Spectroscopy in V_2O_3**. (a) Temperature dependence of far- infrared conductivity of a 75 nm V_2O_3 thin film on sapphire measured by THz time domain spectroscopy. (b) Real part of the optical conductivity as a function of photon energy for various temperatures. The arrows indicate the spectral range for the pump and probe pulses for the far-infrared time-resolved experiments. (c) THz conductivity dynamics as a function of delay time at different temperatures. (d) Normalized conductivity dynamics for of a 95 nm V_2O_3 thin film on sapphire and fluences between 1.73 and 4 mJ/cm^2, fitted using Avrami's Eq. (2.1) with n = 2. Panel (a), (b) and (c) adapted from [Liu et al. (2011)], panel (d) adapted from [Abreu et al. (2015)].

the transition in a 75 nm V_2O_3 film grown on sapphire was published [Liu et al. (2011)]. They performed optical-pump terahertz (THz)-probe measurements with a regenerative amplifier producing 35 fs, 3.5 mJ pulses centered at 1.55 eV (800 nm). The 0.1-2.5 THz pulses were used to probe the far-infrared optical conductivity. Fig. 2.6 (b) shows the equilibrium optical conductivity from the far-infrared to 6 eV at 100, 200, and 400 K. Below $T_{MIT} \sim 150$ K, an optical gap of 500 meV is observed. Above 200 K there is a decrease of the spectral weight below 1 eV. The spectral contribution in the range 0-3 eV is determined by the non-degenerate a_{1g} and double degenerate e_g^π orbitals, therefore, the pump and probe pulses are primarly exciting and probing the vanadium d-orbitals manifold and the emergence of a macroscopic metallic state. Above a threshold of 1 mJ/cm^2 of incident pump fluence, they measured the pump-induced increase of the THz conductivity σ_1 at different temperatures (see Fig. 2.6 (c)). A $\sim$ 20 ps rising time is observed, even if the THz conductivity σ_1 reaches a plateau after $\sim$ 100 ps indicating the complete metallization of the probed area. The rise time, which is considerably longer than the time for electron-phonon thermalization, represents the effect of a latent heat in this first order phase transition and prevents a faster dynamics.

A more detailed study of the photo-induced dynamics was made a few years later by Abreu et al. (2015). By means of a similar technique, optical pump-THz probe, the authors studied nucleation and growth of metallic domains by varying the initial temperature and the absorbed fluence. In particular they applied a Bruggeman Effective-Medium Approximation (BEMA) to estimate the metallic filling fraction related to the pump-induced variation of conductivity $\Delta\sigma$ (for a more detailed discussion about the BEMA, see Appendix C.1). They discovered that the dynamics of nucleation and growth and, in particular, the metallic filling fraction $F_M(t)$ follow the Avrami's law [Avrami (1939)]:

$$F_M(t) = 1 - \exp\{-Kt^N\} \tag{2.1}$$

where K is the rate for the increase of $F_M(t)$, and N is an exponent that depends on the dimensionality and nature of the nucleation and growth. By fitting the experimental data, they have found $N = 2$ consistent with a two-dimensional interfacial growth with quasi-instantaneous nucleation (see Fig. 2.6 (d)). Then, the growth propagates in a balistic way at the sound velocity, which is consistent with the 30-70 ps of rise time they observed. In particular, they have found just one dynamics of growth and almost instantaneous nucleation because they were insensitive to the very small metallic nuclei, since essentially they were probing the interconnectivity of the metallic domains after percolation that gives a mesoscopic change in the DC conductivity. By considering the measurements as a function of the initial temperature, they discovered that closer to the T$_{\text{IMT}}$, a faster time to reach saturation was observed (i.e, the complete metallization of the probed area). In a similar way, starting from the same temperature, higher fluence drives the system to saturation in less time. In these works, the photo induced transition was essentially attributed to the local heating induced by the pump laser.

In 2015, a theoretical work by M. Sandri and M. Fabrizio demonstrated the possibility to photoinduce a non-thermal MIT with the collapse of the Mott gap driven by the change of the orbital polarization $\delta p = n_{\text{v}}$ - n_{c} rather than Joule heating [Sandri and Fabrizio (2015)]. In particular, they discussed the case of quarter-filled two bands Hubbard model of V_2O_3, which does describe a Mott insulator with a charge gap between occupied and unoccupied orbitals. Specifically, they performed a time-dependent Gutzwiller approximation to study the temporal evolution of a nonequilibrium initial state characterized by an excess population of particle-hole excitations, where holes lie in the lower Hubbard band of the occupied orbital while particles sit in the unoccupied conduction orbital. According to their results, a transient change of $\delta p \sim 0.15/0.20$ (or an absorbed fluence $\sim$ 11-15 mJ/cm^2) might drive the system in a metastable *non-thermal* metallic state. This threshold now appears to be quite high since more recent experimental works seem to show a lower threshold for photoinducing the non-thermal transition. In 2017, G. Lantz and co-workers claimed that a transfer of $\sim$ 0.13 electrons to the conduction band was possible to drive the system into a metastable metallic phase [Lantz et al. (2017)]. In particular, experimentally, they performed time-resolved photoelectron spectroscopy (trPES), probing the electronic structure and time-resolved X-ray diffraction (trXRD) probing the lattice evolution, as well as time-resolved reflectivity (TRR). This remarkable result was obtained by reducing the repetition rate of the pump laser but by keeping the same energy per pulse, to avoid Joule heating effects. They discovered that the formation of this non-thermal phase is very fast - faster than their experimental time resolution $\sim$ 50 fs - and it is eminently electronic in nature, being driven by a transient overpopulation of a bonding a_{1g} orbital, as previously suggested by M. Sandri and M. Fabrizio.

A paradigm change of strategy has been the use of intense terahertz pulses to reveal an almost instantaneous ($t_{pp} < 0.3$ ps) purely-electronic IMT generated by quantum tunneling of valence electrons across the Mott gap [Giorgianni et al. (2019)] (see Fig. 2.7 (a)). This non-thermal transition occurs without any direct interaction with the lattice but demands large electric fields at very short timescales. In 2019, F. Giorgianni and co-workers performed non-resonant THz stimulus to trigger an ultrafast IMT in V_2O_3. The pump spectrum is strictly below the main optical phonon modes of the insulating phase (see Fig. 2.7 (b)), and prevents a direct resonant excitation

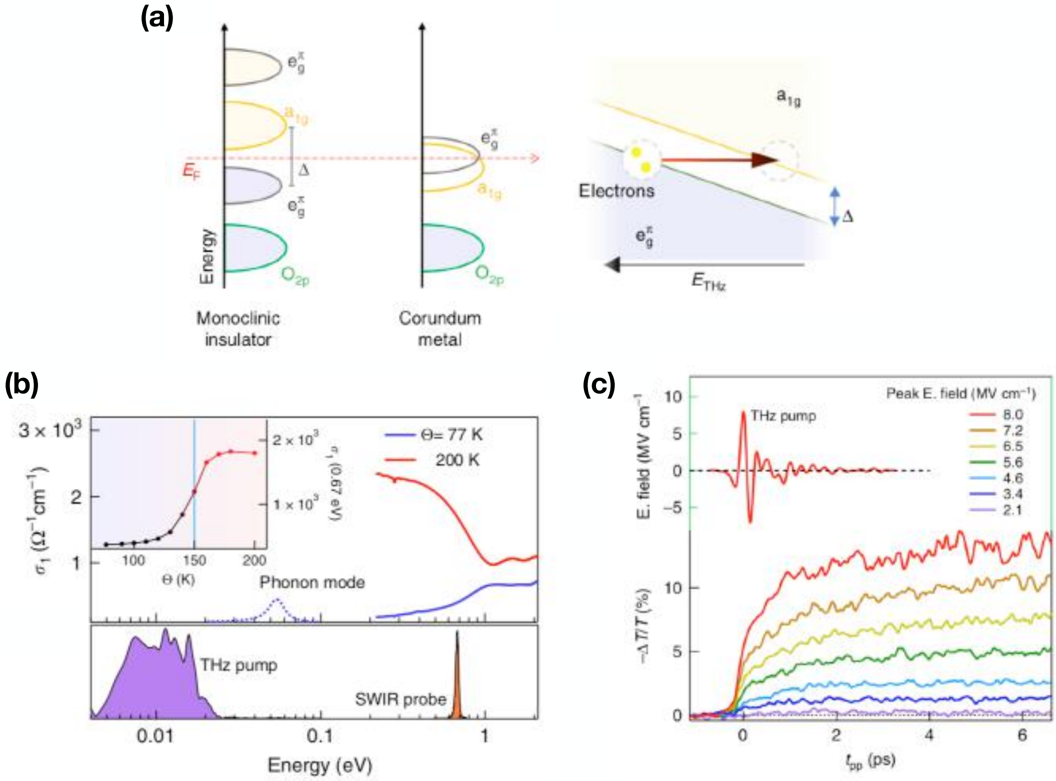

Figure 2.7: **Non-thermal electric-field driven Mott transition in V_2O_3**. (a) Left: Energy level diagrams for the AFI phase and paramagnetic metallic PM phase of V_2O_3. Right: Non-resonant THz field induces energy band distortion and leads to an interband tunneling of electrons in a_{1g} resulting in a sub-ps Mott transition. (b) Top: Real part of the optical conductivity as a function of photon energy for 77 K and for 200 K. Inset: Temperature dependence of the real part of the optical conductivity at the probe energy (0.67 eV). Bottom: Spectral distribution for the THz pump and short-wave infrared (SWIR) probe pulses. THz pump photon energy is below the lattice phonon modes and the interband transitions. SWIR probe energy measures the metallicity of the system. (c) Maximum THz pump field and (bottom) differential transmission modulation -$\Delta T/T$ at T = 4 K probed by short-wave infrared (SWIR) laser as function of different pump field strengths (from 2.1 to 8 MVcm^{-1}). Adapted from [Giorgianni et al. (2019)].

of the lattice. The temporal dynamics of the electronic response to the THz excitation is probed using an ultrashort laser at a photon energy of 0.67 eV (SWIR). At this energy, the contribution to the optical conductivity is dominated by intraband transitions, and therefore they were probing the metallic behavior of the system. In Fig. 2.7 (c) the traces of transient change in transmission through the sample for field strengths between 2.1 and 8.0 MVcm^{-1} are shown. We can observe a two-step dynamics characterized by a sudden suppression over the timescale of the THz pump excitation followed by a slow transient. The differential transmission turns constant after tens of ps, meaning the thermal nucleation of mesoscopic metallic puddles. The rapid switching, over the sub-optical period of THz pump pulse (rise time, $t_{pp} < 0.3$ ps), is the experimental fingerprint of a purely electronic transition. In this picture, the main effect of the strong THz electric field is to move electrons into $\mathrm{a_{1g}}$ band by quantum tunneling. Indeed, due to the strong electric field, the $\mathrm{a_{1g}}$ and e_g^π bands start to bend (Fig. 2.7 (a)) and this induces the band crossing. In addition, Giorgianni et al. (2019) claimed that the electrically-driven Mott transition can be disentangled from the Joule heating with the temperature. Indeed, when the background temperature is well below the $\mathrm{T_{IMT}}$ (for instance, T = 4 K, as shown in Fig. 2.7 (c)), a pure tunneling breakdown leads to the metal monoclinic precursor phase on a sub-ps timescale followed by a subsequent lattice rearrangement. This result paves the way to control Mott devices as ultrafast electronic switches at Terahertz frequencies.

2.2.3 Metastability of the monoclinc metallic phase

The mechanism driving the MIT in vanadates is still an object of strong debates. Although numerous studies have been conducted in the past few decades, the relationship between competing electronic, structural, magnetic, and orbital DOF is not clear yet. In particular, understanding the transition mechanism and how to decouple the SPT from the electronic MIT would allow for Mott devices with low power consumption and reduced switching time. For instance, in VO_2, already many studies have been devoted to investigate the evolution of the MIT and SPT, both at equilibrium and out-of-equilibrium. Although a final verdict is still far away, many results seem to suggest that the temperature-driven structural and electronic transition follow different paths [Nag et al. (2012); Qazilbash et al. (2011)]; in particular, the observation of metallicity without the structural transformation to the rutile phase [Kim et al. (2004, 2006, 2008)], the bad metal behavior of

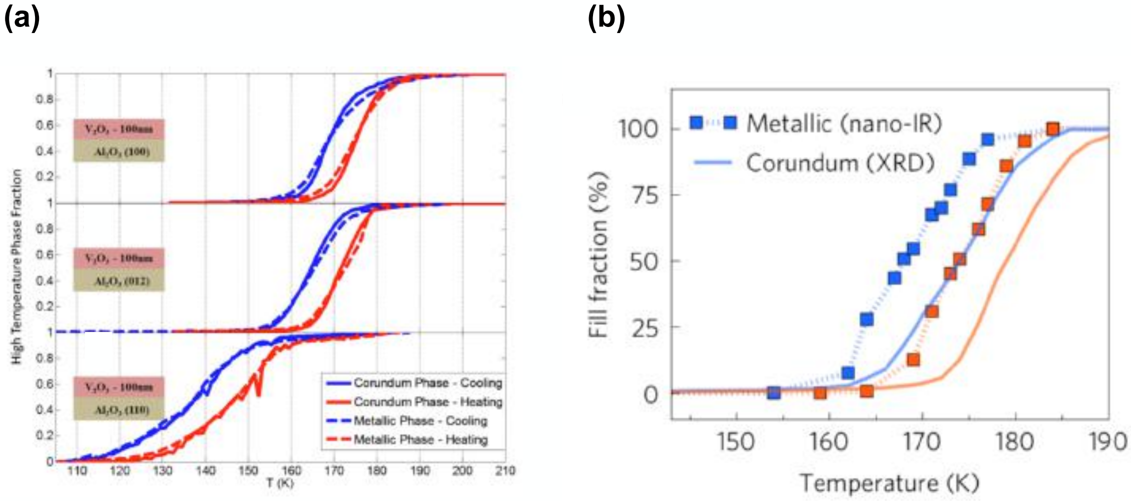

Figure 2.8: **Comparison between SPT and MIT.** (a) Comparison between the metallic and corundum phase fractions as determined from IR spectroscopy and XRD adapted from [Kalcheim et al. (2019)]. The picture suggests the coupling of the SPT and MIT. The temperature sensitivity is 1 K. (b) Comparison between areal fill fractions for the metallic phase identified by nano-IR imaging and volumetric fractions for the high-temperature structural phase (corundum) identified by XRD adapted from [McLeod et al. (2016)]. The $\sim$ 6K shift between the two hysteresis loops suggests the presence of a monoclinic metal in the proximity of MIT. Panel (a) adapted from [Kalcheim et al. (2019)]

the rutile phase [Qazilbash et al. (2006)], the observation of metallicity in the monoclinic structure in high-pressure measurements [Arcangeletti et al. (2007)], the fast time scales for the appearance of metallic conductivity compared to the lattice dynamics [Kübler et al. (2007)], and theoretical first principles calculations [Liang et al. (2019)] suggest the existence of a metastable monoclinic metallic state.

In V_2O_3, the situation is more complex since the MIT and SPT are accompanied by antiferromagnetic ordering. Anyway, many results indicate that the transition from the paramagnetic to the antiferromagnetic state is possibly decoupled from the MIT. In fact, AFM fluctuations have been reported experimentally above T_C [Bao et al. (1997); Trastoy et al. (2020)] and theoretical works support the possibility to induce the transition from corundum metal to monoclinic insulator even without magnetic ordering [Grieger and Fabrizio (2015)]. A very recent work by I. K. Schuller's group combines IR spectroscopy and X-ray diffraction (XRD) and claims that structural and electronic transition are strongly coupled [Kalcheim et al. (2019)]. In particular, comparing the temperature dynamics of the metallic phase (IR spectroscopy) and of the corundum phase (XRD), they claim that, by forcing a strain through films due to the lattice mismatch on different Al_2O_3 substrates, the structural and electronic dynamics remain interconnected within 1 K. Nevertheless, looking at the top panel in Fig. 2.8 (a), it seems evident how the two transitions have different shapes, reaching a variation of the filling fraction of about 7% at 175 K, during cooling. Similar conclusions have been reported even by Frandsen et al. (2019). As we discussed above, in 2016, A. S. McLeod combined near-field infra-red microscopy with XRD to analyze the filling evolution of insulating and metallic nanodomains across the MIT. The surprising result shown in Fig. 2.8 (b) is $\sim$ 6 K separation between the MIT and the SPT, suggesting an intermediate monoclinic metal that may be stabilized by residual strain in the film.

In support of decoupling between the MIT and SPT, experimentally, V_2O_3 remains metallic during the corundum to monoclinic structural transition if subjected to very high pressure ($\sim$ 32.5 GPa) [Ding et al. (2014)]. Hard x-ray absorption has been used to study the fine structure changes during the thermally-driven PM $\rightarrow$ AFI MIT [Pfalzer et al. (2006)]. They distinguished between two structural effects with different temperature characteristics: (1) At the onset of the electronic transition temperature, the vanadium dimers along the hexagonal c axis abruptly increase their distance transforming the system from metal to insulator; (2) viceversa in the basal plane it is observed a continuous increase of the monoclinic distortion starting above T_{MIT} and getting its maximum at T_{MIT}. The different contribution of the in-plane and out-of-plane (with respect c axis) structural distorsion of vanadium dimers, in determining the electronic properties of the system, was discussed also in theoretical works [Grieger and Fabrizio (2015)]. These results strongly support the scenario of a structural precursor which possesses metallic properties while maintaining the in-plane monoclinc distortion. In particular, more evidence for a structural precursor to the MIT was reported in surface acoustic waves measurements [Kündel et al. (2013)], Raman spectroscopy [Majid et al. (2017)] and, in the case of a recent out-of-equilibrium experiment, time-resolved XRD unveiled a two-steps scenario where the corundum crystal structure is partially altered ($\sim$ few ps) before completely recovering ($\sim$ 100 ps) [Singer et al. (2018)].

There is still a lot of ambiguity on this topic although it is of great importance for applications, since MIT without SPT would allow much faster switching times. The main reasons for all these conflicting results can be attributed to three main issues. First of all, it has been shown that the results obtained on nominally equal samples can vary widely, since the transition dynamics is extremely sensitive to microscopic growth defects or impurities in the films. Secondly, the substrate orientation and the growth technique play both a fundamental role in determining the behavior of the MIT. Finally, it is likely that the decoupling of the MIT and SPT takes place within a small temperature difference (a few Kelvin). This implies great accuracy in temperature calibration and in the ways in which this temperature is measured. Experimental aspects such as the presence or absence of a free-standing sample can lead to huge differences in the dynamics of heat dissipation or accumulation [Vidas et al. (2020)]. For this reason it is essential to continue with the investigation by means of out-of-equilibrium spectroscopies to solve the long-standing questions of how to disentangle different DOF and their characteristic time scales. For instance, a recent work [Morrison et al. (2014)] revealed a photoinduced monoclinic metal-like phase in VO_2 by ultrafast electron diffraction and Li et al. (2017) performed imaging of the metal-like monoclinic phase that was stabilized by the surface coordination effect in VO_2 nanobeams. At this point, one may wonder if it would be possible to photoinduce a metastable monoclinc metallic state also in V_2O_3? And if yes, which is the temporal dynamics and the real microscopic behavior of the system? Of course, an attractive perspective for technological applications would be that this metastable state evolves on much faster time scales than those controlled by thermally or electrically-driven IMT.

Chapter 3

Spontaneous self-organization of the monoclinic insulating phase

This chapter has been adapted from the publication:

"Early-stage dynamics of metallic droplets embedded in the nanotextured Mott insulatig phase of V_2O_3 device"
A. Ronchi, P. Homm, M. Menghini, P. Franceschini, F. Maccherozzi, F. Banfi, G. Ferrini, F. Cilento, F. Parmigiani, S.S. Dhesi, M. Fabrizio, J-P. Locquet, and C. Giannetti

Phys. Rev. B. **100**, 075111 (2019)
doi: *10.1103/PhysRevB.100.075111*

In this chapter, we use element-specific x-ray nanoimaging to investigate the early stages of the formation of nanometric metallic seeds across the IMT in a 40 nm V_2O_3 thin film on (0001)-Al_2O_3 substrate. We discover an intrinsic nanotexture of the monoclinic antiferromagnetic insulating (AFI) phase, which is characterized by striped and ordered polydomains with different lattice distortions. Before the present work, the insulating phase was supposed to be completely homogeneous [McLeod et al. (2016)]. In the insulator-metal coexisting region, the boundaries of the insulating stripes seed the formation of metallic nuclei, whose proliferation leads to the formation of mesoscopic metallic networks through a percolative IMT

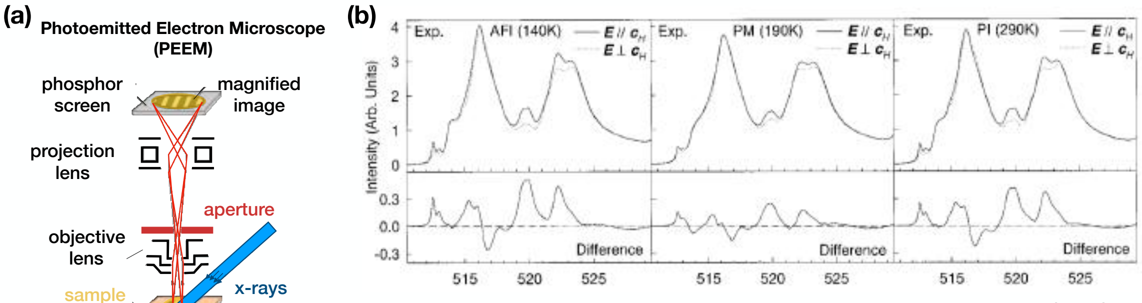

Adapted from Park et al. PRB **61**, 11501 (2000)

Figure 3.1: **PEEM experimental working principle.** (a) Sketch of the PEEM working principle. A monochromatic beam of polarized x-rays is shined on the sample. The energy delivered to the system is selectively absorbed by atoms and, as a consequence, core electrons are photoemitted from the surface. A system of electromagnetic lenses drive the photoemitted electrons through the analyzer up to the phosphor screen, where the microscopic nanotexture is reconstructed. The different contrast originates from the different occupancy of the selective element orbitals. (b) X-ray absorption spectroscopy (XAS) spectrum showing the $L_{2,3}$ vanadium absorption lines in the AFI, PM and PI phases of V_2O_3. The different XAS spectra are observed according to the different coupling of the x-ray polarization with the a_{1g} orbitals, which are oriented along the V_2O_3 c-axis. The occupancy ratio $n_{a_{1g}}/n_{e_g^\pi}$ within the V t_{2g} orbitals controls the X-ray Linear Dichroism (XLD) contrast between AFI and PM phases. Image adapted from [Park et al. (2000)].

transition. This AFI nanotexture appears to be an intrinsic property of the insulating phase, independently of the film's thickness or the substrate characteristics, as predicted from the theory of the martensitic transitions [Papon et al. (2006)]. In addition, those domains are pinned during the heating up and cooling down thermal cycle, and this is a novel and original result rarely observed in other martensitic systems, and, never reported in V_2O_3. The PEEM measurements shown in this chapter were performed at beamline i06 of Diamond Light Source (DLS) (Didcot, The United Kingdom).

3.1 Experimental technique: Photoemitted Electron Microscopy (PEEM)

X-ray Absorption Spectroscopy (XAS) and PhotoEmitted Electron Microscopy (PEEM) have been performed to investigate the dynamics of the intrinsic nanotexture of the V_2O_3 insulating phase across the IMT. X-ray absorption spectra of any material, atomic or molecular in nature, are characterized by sharp increases in absorption at specific X-ray photon energies. These energies are characteristic of the absorbing element and corresponds to the energy required to eject a core electron (i.e. a photoelectron). By studying the spectra coming from a particular sample, it is possible to get useful information about lattice distortions, magnetic behavior and chemical composition. The PEEM combines the chemical and structural sensitivity of XAS with an electromagnetic microscope able to resolve nano-inhomogeneities in the XAS spectra with spatial resolution down to 20 nm (see Fig. 3.1). The Field Of View (FOV) of the x-ray beam is $10 \times 10\ \mu\text{m}^2$. The PEEM images presented in this thesis have been obtained by performing X-ray Linear Dichroism (XLD) experiments at a photon energy of ∼513.4 eV in proximity to the vanadium $L_{2,3}$ edge. The Linear dichroism (LD) is the difference between absorption of light polarized parallel and polarized perpendicular to an orientation axis. Indeed, each PEEM image is the average of the difference between 50 PEEM images taken with light polarization parallel (i.e., in the a-b plane) and perpendicular (i.e., along the V_2O_3 c-axis) to the film surface, normalized by their sum. In the AFI phase, the XLD signal at the specific energies of 513 and 520 eV arises from the difference in absorption between X-rays polarized parallel and perpendicular to the a_{1g} orbitals (see Fig. 3.1 (b), adapted from Park et al. (2000)), which have lobes oriented along the c-axis. The different contrast between the AFI and PM phases originates from the different occupancy ratio, $n_{a_{1g}}/n_{e_g^{\pi}}$, within the V t_{2g} orbitals [Park et al. (2000),Rodolakis et al. (2010)].

3.2 Results and discussion

Description of the AFI nanotexture and thermal dynamics of the IMT

Snapshots of the IMT in real space have been taken via XLD-PEEM on a 40 nm V_2O_3 film epitaxially grown on a (0001)-Al_2O_3 substrate (sample VB6-B), therefore with the c-axis perpendicular to the surface (see Appendix A). In Fig. 3.2 (b) (top left) we report the spatially resolved XLD contrast at 513 eV in the AFI phase (T = 120 K). Striped insulating nanodomains, oriented along the hexagonal crystallographic axes, are clearly visible with characteristic dimensions of a few micrometers in length and 200-300 nm in width. The analysis of the intensity distribution (see Appendix B.1)

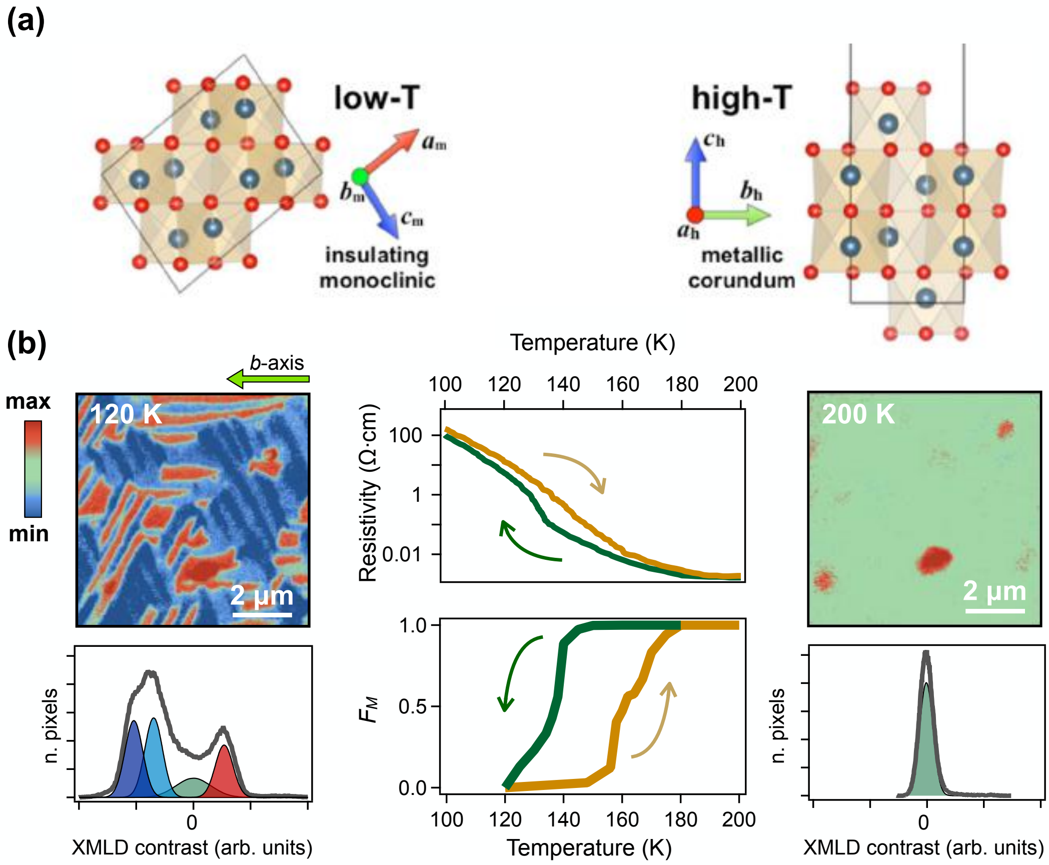

Figure 3.2: **Nanoscale insulating domains imaged by XLD-PEEM.** (a) Left: a-c plane projection of the monoclinic lattice structure in the low-T AFI phase. The $\mathrm{a_m}$, $\mathrm{b_m}$, and $\mathrm{c_m}$ axes of the monoclinic cell are indicated by the colored arrows. Right: c-b plane projection of the corundum lattice structure in the high-T PM phase. The $\mathrm{a_h}$, $\mathrm{b_h}$, and $\mathrm{c_h}$ axes of the hexagonal cell are indicated by the colored arrows. (b) Left top: XLD-PEEM image taken at 120 K (heating branch of the hysteresis) evidencing striped monoclinic domains. Left bottom: XLD intensity distribution (thick gray line) of the image. The analysis evidences a broad zero-centered distribution (green), corresponding to the resolution-broadened edges of the striped domains, and three distinct distributions with nonzero signal (red, blue, light blue), reflecting the different structural nanodomains within the AFI phase. Middle: Hysteresis cycle as obtained by resistivity measurements and by the metallic filling analysis of the temperature-dependent XLD-PEEM images (see Appendix B.1). The yellow (green) arrows indicate the heating (cooling) cycles. Right top: XLD-PEEM image taken at 200 K (heating branch of the hysteresis) showing a homogeneous background, typical of the PM phase. The residual red spots are due to defects used as reference to precisely align the XLD-PEEM images. Right bottom: XLD intensity distribution (thick gray line) of the image. The analysis evidences a zero-centered single-mode distribution. Adapted from [Ronchi et al. (2019)].

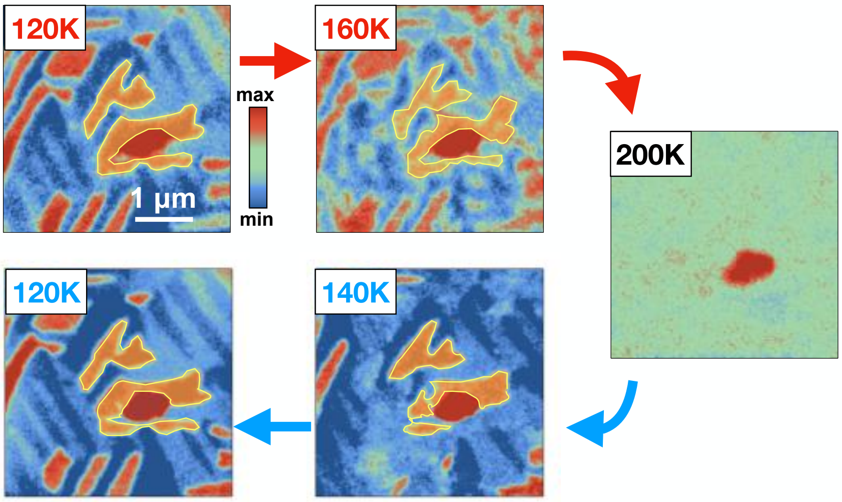

Figure 3.3: **Domain pinning and hysteresis.** XLD-PEEM images at different temperatures during a heating and cooling cycle. After the complete melting of the AFI phase at T = 200 K, the insulating striped domains form in the same spatial position when the system is cooled down to T = 120 K. Adapted from [Ronchi et al. (2019)].

highlights the presence of three different regions, which correspond to three possible orientations of the monoclinic domains subject to distortions along the three equivalent edges of the hexagonal unit cell [Singer et al. (2018); Dernier and Marezio (1970); Lüning et al. (2003)]. In addition, the XLD contrast of the insulating domains depends on the relative angle between the direction of the linear horizontal light polarization and the antiferromagnetic axis within each domain (for a complete discussion of the angular dependence of the XLD signal, see Appendix B.3.) During the heating up process, the XLD contrast of the insulating domains progressively vanishes until the uniform metallic phase, characterized by a single color distribution, emerges (see right-top panel in Fig. 3.2 (b)). We point out that, under temperature cycling, the striped domains always nucleate at the same location and with the same characteristics (see Fig. 3.3), thus suggesting that the formation of nanotextured polydomains is not only unavoidable in the transformation from the high-temperature corundum structure to the low-temperature monoclinic one [Roytburd (1995)], but also reproducible. The reason of this fact can be assigned to the presence of nucleation centers for the insulating phase likely formed by defects in the crystalline structure. Therefore, these defects determine the initial condition of the monoclinic

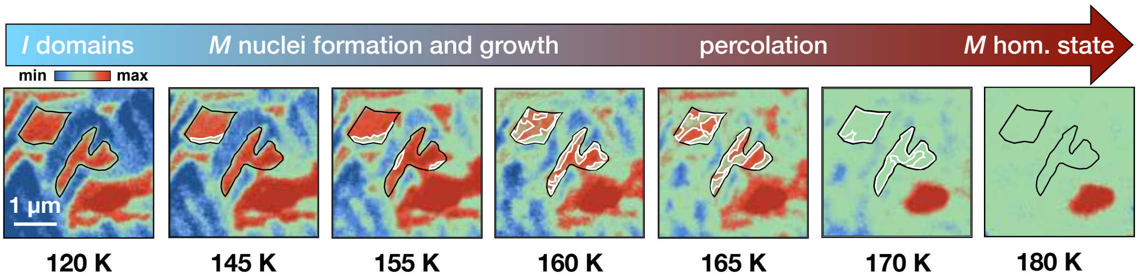

Figure 3.4: **Temperature-dependent XLD-PEEM images.** The color scale is the same as that reported in Fig. 3.2 (b). The black contours highlight the monoclinic domain on which the metallic filling analysis has been performed. The white contours indicate the metallic seeds within the monoclinic domains as identified via the routine described in Appendix B.1. The arrow highlights the main processes leading to the complete IMT. We can recognize three different phases for the metallic seeds dynamics: the nucleation (120 K-155 k), the growth (155 K-165 k) and the percolation (above 165 K). Adapted from [Ronchi et al. (2019)].

seed nucleation with the consequence of blocking the monoclinic domain in the same position each time. The metallic filling F_M is calculated as the ratio between the number of metallic pixels (green XLD contrast), recognized by pixel-based segmentation techniques (see Appendix B.1), and the total number of pixels within a fixed monoclinic domain. The temperature dependence of F_M is shown in the bottom-middle panel of Fig. 3.2 (b). The metallic filling displays a large temperature hysteresis ($\delta T \sim$ 20 K), which corresponds to the resistivity hysteresis measured on the same sample and reported in the top-middle panel of Fig. 3.2 (b). When focusing on specific monoclinic domains (see the black contours in the XLD-PEEM images shown in Fig. 3.4)), we observe the emergence of finite-size metallic nuclei [see the white contours in the XLD-PEEM images shown in Fig. 3.4], i.e., metallic regions with a critical width larger than the experimental resolution of 30 nm, at temperatures above 145 K. The metallic phase nucleates along the boundaries between different monoclinic domains, which is a typical characteristic of martensitic transitions [Papon et al. (2006)]. Martensitic effects in the course of the IMT in V_2O_3 were already suggested on the basis of acoustic emission experiments [Chudnovskii et al. (1997)]. When further increasing the temperature, the growth of the elongated metallic nuclei leads to a percolative transition [McLeod et al. (2016)] in a narrow temperature range centered at $\sim$ 160 K, which corresponds to F_M^{perc} = 0.45. At 180 K, the average dimension of the residual insulating puddles is below the experimental resolution, and the metallic phase eventually

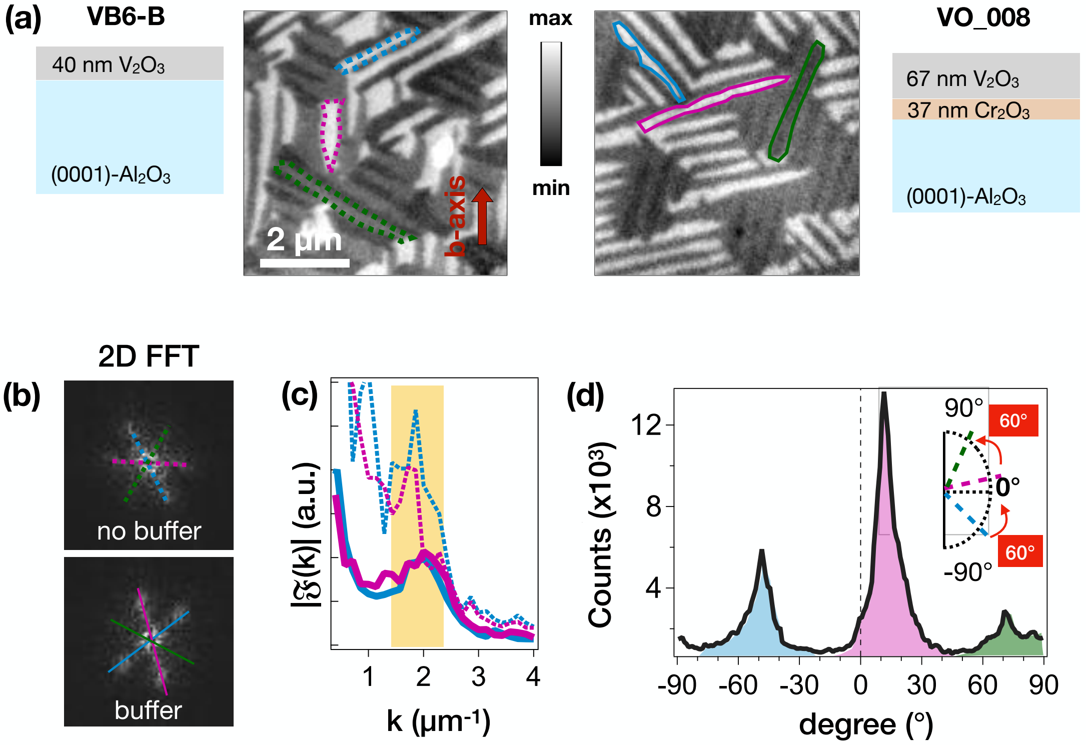

Figure 3.5: **Comparison of the two films.** (a) Middle: XLD-PEEM snapshots taken at 120 K (heating branch of the hysteresis) for the sample with (right) and without (left) buffer layer. Nano-textured striped AFI domains are shown. Dashed/solid coloured lines (blue, pink, green) highlight the three main orientations of the AFI domains. Left and right: schematic description of the sample with (right) and without (left) buffer layer. (b) 2D Fast Fourier Transform (FFT) calculated starting from the images in (a), respectively top: no buffer layer and bottom: with buffer layer. The three main directions are highlighted via solid/dashed coloured straight lines (blue, pink, green). (c) 2D FFT Line profiles along the domains directions. The yellow box highlights the main peaks (in k-space) according to the domain real space periodicity. (d) Angular distribution histogram: The analysis evidences the presence of three distinct distributions (blue, pink, green) about 60 degree equally angular spaced, as schematically shown in the small inset.

occupies most of the pristine insulating domains ($F_M \simeq 1$).

Role of the residual strain controlled by the Cr_2O_3 buffer layer in the domains formation

Another important consideration can be done by analyzing a different sample, a 67-nm-thick V_2O_3 film epitaxially-grown on a 37-nm-thick Cr_2O_3 buffer layer on (0001)-Al_2O_3 substrate (sample VO008). By looking at the results in Fig. 3.5 (a), it is possible to observe how the stripes appear to be more regular in the sample with the Cr_2O_3 buffer layer as compared with the one grown directly on Al_2O_3. We investigated the intrinsic periodicity of these two different thin films. A 2-dimensional Fast Fourier Transform (FFT) of the images is shown in Fig. 3.5. In Fig. 3.5 (b), we reported the images computed by the numerical algorithm [Cooley and Tukey (1965)], as a 2D map for the absolute Fourier Transform (FT) spectral weight $|F(k)|$. In both cases, the most intense signal is obtained along the three principal orientations, perpendicular respectively to the three principal domains directions in the real space snapshots. The less-regular aspect of the sample VB6-B causes a broader intensity distribution in the 2D FFT plot. Taking a line cut along the direction of the most intense peaks in Fig. 3.5 (c), we can quantitatively estimate the typical spatial periodicity of the AFI stripes as the reciprocal of the position of the main FFT peaks in the k-space, $\lambda_{\text{buffer}} = (519 \pm 10)$ nm and $\lambda_{\text{no buffer}} = (538 \pm 26)$ nm as reported in Fig. 3.5 (c). Therefore, the lateral dimension of the AFI domains can be easily extracted as half the periodicity, and respectively $d_{\text{buffer}} = (260 \pm 5)$ nm and $d_{\text{no buffer}} = (269 \pm 13)$ nm. This results fall in the 95% confidence interval. We characterized the orientation and isotropic properties of the polydomains in the images, using the Java plug-in OrientationJ [Püspöki et al. (2016); Fonck et al. (2009); Rezakhaniha et al. (2012)] for Fiji [Schindelin et al. (2012); Rueden et al. (2017)]. Analyzing the evolution of the structure tensor in a local neighborhood, the software calculated the angular distribution of the pixels constituting the image. Thus, in Fig. 3.5 (d) we discern three peaks sixty degree angular spaced in the distribution plot. Similar results have been obtained in both samples. Therefore, as main result of the above analysis, the dimensionality of these AFI domains appears to be an intrinsic property of the insulating phase, independently of the film thickness or the substrate characteristics, as predicted from the theory of the martensitic transitions [Papon et al. (2006)].

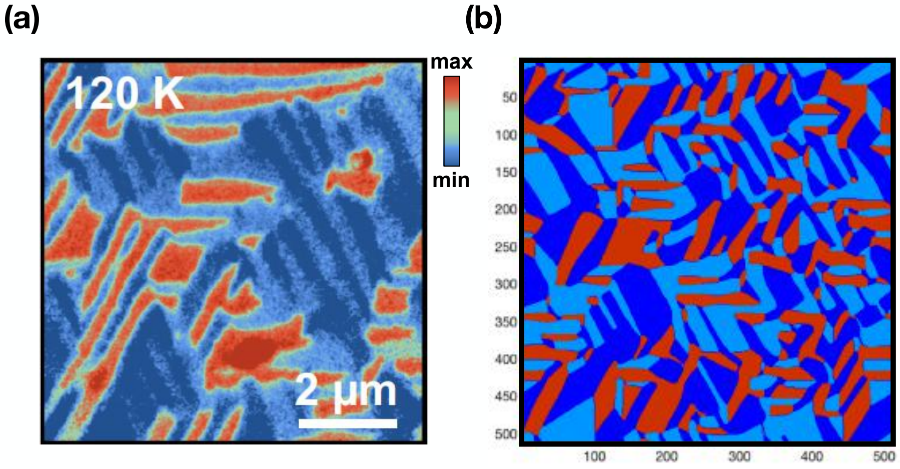

Figure 3.6: **Comparison between experimental results and numerical simulation.** (a) XLD-PEEM snapshot taken experimentally at 120 K (heating branch of the hysteresis) Nano-textured stripy monoclinic domains are shown. (b) Plot of mean field solution of Eq. 3.1 representing the intrinsic nanotexture of the low-temperature phase in V_2O_3. Adapted from [De Poli (2020)].

Numerical approach to the description of the AFI intrinsic nanotexture

Still remains an open question, why these monoclinic domains are formed and if is it possible to theoretically explain and describe their formation? To address these questions, we decided to develop a numerical model able to describe the formation of this intrinsic monoclinic nanotexture below the MIT. The following discussion presents some results obtained in Andrea De Poli's master thesis, in collaboration with Prof. Michele Fabrizio at Trieste SISSA. Further details can be found in [De Poli (2020)]. In a very simple picture, the formulation of the problem is as follows: the system can deform in three degenerate directions, along the three equivalent hexagonal crystallographic axes. On the one hand, it wants to avoid sudden gradients of strain, on the other hand, it can develop inhomogeneous domains that minimize the Ginzburg-Landau free energy. The balance between the two mechanisms gives rise to a nanotexture that allows monoclinic deformations while keeping the total volume unchanged. Therefore, we define a Ginzburg-Landau free energy density to describe the temperature-driven structural phase transition in V_2O_3

$$E[\boldsymbol{\epsilon}(\tau,\mathbf{r})] = f_L(\boldsymbol{\epsilon}(\tau,\mathbf{r})) + \xi^2|\nabla\boldsymbol{\epsilon}(\tau,\mathbf{r})|^2 + \frac{A_1}{2}\int d\mathbf{r}'\boldsymbol{\epsilon}(\tau,\mathbf{r}')^T U(\mathbf{r}-\mathbf{r}')\boldsymbol{\epsilon}(\tau,\mathbf{r}) \tag{3.1}$$

where $\boldsymbol{\epsilon}(\tau,\mathbf{r})$ is the strain tensor, $\tau = \frac{T-T_C}{T_0-T_C}$ is the scaled temperature and U is the interacting potential. The second term in (Eq. 3.1) is the energy cost of creating inhomogeneity in the system. It is given by the well known Ginzburg term proportional to a parameter ξ, named coherence length, that gives information about the length scale necessary for the system in order to recover its equilibrium value after small localized perturbations. The third term in (Eq. 3.1) is the energy gain of the long range inhomogenities. In particular, it originates from the compatibility equations, this means that the distorted unit cells have to fit together in a smooth compatible fashion, without defects-like dislocations, so no gaps or overlaps are admitted. Mathematically these conditions are imposed through the St. Venant compatibility constraint [Borg (1990); Baus and Lovett (1990, 1991)]. The competition between the last two terms defines the typical length scale of the three possible twins insulating domains. The Ginzburg-Landau (GL) energy is transformed in a discrete pseudospin Hamiltonian [Shenoy and Lookman (2008)], that is simply the total scaled free energy evaluated at the Landau minima in the OP. On that a local mean-field approximation [Shenoy and Lookman (2008)] is applied and it gives rise to a set of self consistent equations, that are solved iteratively. The experiments [Ronchi et al. (2019)] have shown typical dimensions of the domains of about a few micrometers in length and $\simeq 250$ nm in width (see Fig. 3.6, panel a). The results in Fig. 3.6 (b) well describe the three monoclinic domains of the intrinsic insulating nanotexture, experimentally observed (Fig. 3.6 (a)). The boundaries between neighbouring domains form angles of 120 degree, following the admitted deformations of the hexagonal cell. In conclusion, the GL model describes the monoclinic insulating phase of the system and its typical nanotexture composed by three different kinds of domains, with defined interface directions, similar to what is found in experiments previously shown in this Chapter [Ronchi et al. (2019)].

First evidence of AFI nanotexture into a micrometric V_2O_3 device

The sample VO008 was coated with gold metal electrodes, made via maskless optical lithography (for further details, see Appendix A). The geometry has

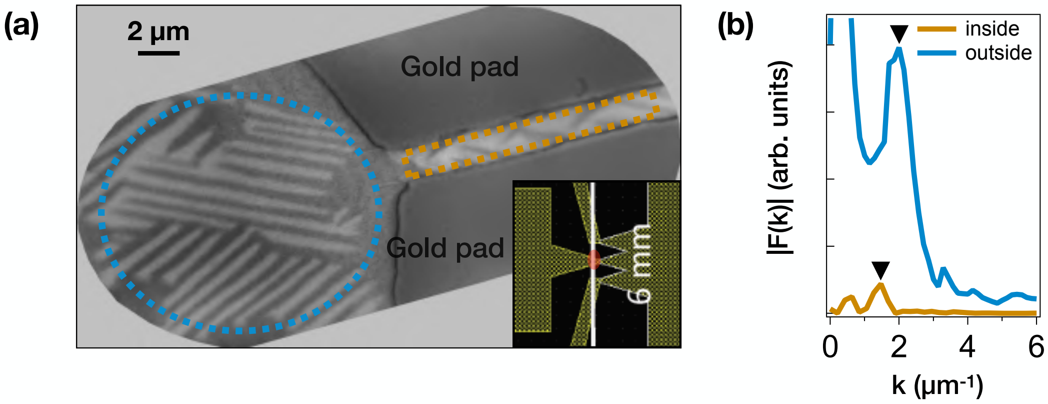

Figure 3.7: **Nanoscale insulating domains in a micro device.** (a) XLD-PEEM snapshots of the gap taken at 120K (heating branch of the hysteresis). Nano-textured stripy AFI domains are shown revealing a different periodicity inside and outside the gap across the metallic pads. In the inset, the investigated region in a larger scale is represented. The color scale used is the same of Fig. 3.5. (b) FFT calculated for the two areas (inside and outside the gap) highlighted with the dashed lines in (a). An evident lower-k shift of the main FFT peak for the area inside the gap is observed.

been studied for applying an electric bias during the transport measurements (see inset Fig. 3.7 (a)). The presence of three gaps (1, 2 and 3 um width x 50 um length) permits to perform resistive switching experiments since V_2O_3 shows a IMT when a sufficiently large electric field is applied across the gap in the proximity of T_{IMT}. In Fig. 3.7 (a) PEEM snapshot showing evidence of AFI domains into a narrow separation region (i.e the gap) is shown. In particular, a difference in the stripes periodicity can be immediately observed. By comparing the FFT calculated on an evaluating region within (yellow dashed line) and outside (blue dashed line) the gap, we immediately see a lower frequency shift in the second area, as reported in Fig. 3.7 (b). Indeed, the main peak appear respectively at k vectors corresponding to a periodicity of $\lambda_{IN} = (700 \pm 18)$ nm and $\lambda_{OUT} = (519 \pm 10)$ nm. Hence, it is possible to argue that the presence of the metal pads somehow induces a variation in the periodicity of the AFI stripes. This periodicity change could be attributed to the presence of additional strain in the gap region as a consequence of the metal electrode deposition. Preliminary analysis of the temperature-dependent resisitivity measurements and RT-Raman spectroscopy performed inside and outside the gap region didn't reveal any relevant information to clarify a potential role of residual strain in the gap. This might be addressed to the fact that the metal electrodes can probably induce additional strain just close to the surface of the film. Therefore, further surface sensitive investigations of the nano-patterned gap region will be fundamental to unveil the mechanism of electrical breakdown in such microdevices.

3.3 Conclusion

In conclusion, we shed new light on the intrinsic nanotexture of the monoclinic AFI phase of V_2O_3 and its relation with the nature of the IMT dynamics [Ronchi et al. (2019)]. Exploiting the sensitivity of resonant x-ray PEEM to the orientation of the V 3d orbitals, we unveiled a spontaneous self-organization of the Mott insulating phase, characterized by striped monoclinic domains with different orientations. The insulating stripes are stable and reproducible, as they form in the same position under temperature cycling. This AFI nanotexture appears to be an intrinsic property of the insulating phase, independent of the film's thickness or the characteristics of the substrate, as predicted from the theory of the martensitic transitions [Papon et al. (2006)].

Chapter 4

Early-stage metalization triggered by photoinduced orbital polarization

This chapter has been adapted from the publication:

"Early-stage dynamics of metallic droplets embedded in the nanotextured Mott insulatig phase of V_2O_3 device"
A. Ronchi, P. Homm, M. Menghini, P. Franceschini, F. Maccherozzi, F. Banfi, G. Ferrini, F. Cilento, F. Parmigiani, S.S. Dhesi, M. Fabrizio, J-P. Locquet, and C. Giannetti

Phys. Rev. B. **100**, 075111 (2019)
doi: *10.1103/PhysRevB.100.075111*

In this chapter, the growth dynamics of the metallic seeds is investigated by probing the transient optical conductivity in the 1.4–2.2 eV energy range, which is extremely sensitive to the local band-structure rearrangement in the nanometric metallic regions. We demonstrate that weak light excitation, i.e., with fluence smaller than that necessary to overcome the latent heat and to photoinduce a mesoscopic IMT, triggers the growth of the metallic filling factor in the system. The application of the Avrami model indicates that the dynamics saturates after 25–30 ps, which corresponds to the time necessary for the propagation at the sound velocity of metallic droplets across the $\sim$ 250-nm-wide insulating stripes. The time-resolved optical conductivity spectra have been measured using different pump-probe setups situ in Interdisciplinary Laboratories for Advanced Materials Physics (ILAMP) laboratories (Brescia, Italy) and T-Rex laboratory (Trieste, Italy).

4.1 Experimental technique: Time-Resolved Optical Spectroscopy

Nowadays time-resolved spectroscopy is intensively used to investigate the out-of-equilibrium ultrafast electron dynamics of strongly correlated materials [Giannetti et al. (2016)]. The different many-body interactions have dynamics spanning time scales ranging from 100 fs up to 10 ns.

The standard approach that is used to access these time scales is the pump-probe technique. In this method, a laser is splitted into two beams through a beam splitter. Between the two beams, the one with larger intensity (pump) is used to excite the sample. The second one with lower intensity (probe) is used instead to snapshot the dynamics of the sample. Since the probe laser beam is much less intense than the pump's one, it does not substantially excite the sample (Fig. 4.1). What it is measured directly with this technique is the difference of relative transmission (or relative reflectivity) of a certain material. The optical properties of the material are changed by a perturbation in the electronic structure. This perturbation is given by the pump pulse, the variation in transmission/reflectivity is investigated through probe pulses. The probe works like a "photo camera" taking snapshots of the dynamics of the system at different time delays. If we can ensure that the probe pulses arrive on the sample with increasing delays time with respect to pump pulses, we are also able to follow the relaxation dynamics of the sample from the excited state to the unperturbed. To introduce the delay between the pulses, the most used method is a mechanical delay line. This line allows the pump pulse to follow a different optical path so that the two beams arrive on the sample with a relative time delay. By controlling the difference in the optical path of the probe beam with respect to the pump beam, the time delay between the two pulses can be tuned. Varying this delay one can access the whole relaxation dynamics of the sample.

Generally, the thermal dynamics of a thin-film excited by an ultrashort laser pulse (pump) can be described with a 3-steps process spanning different time scales [Banfi et al. (2010)]:

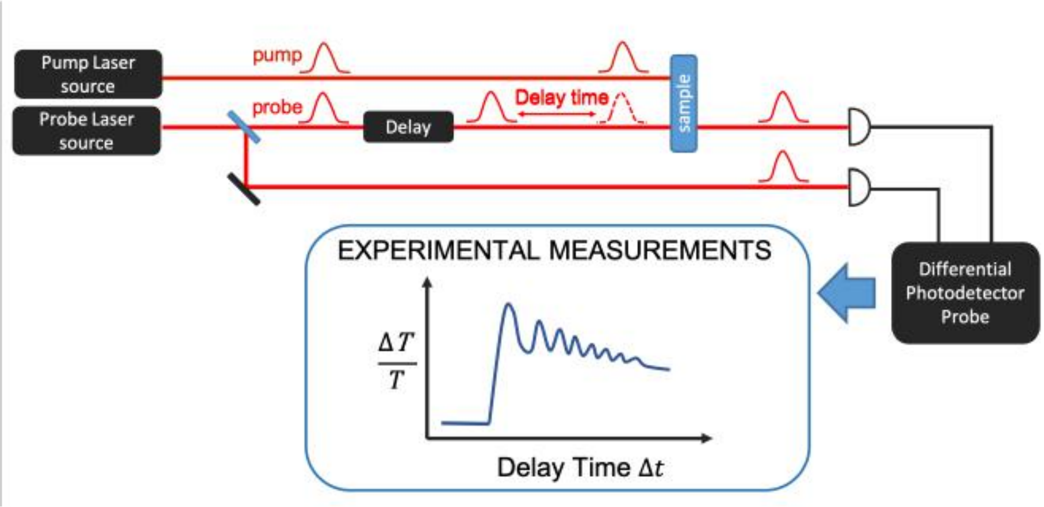
Pump Laser source
Probe Laser source
pump
probe
Delay
Delay time
sample
Differential Photodetector Probe
EXPERIMENTAL MEASUREMENTS
$\frac{\Delta T}{T}$
Delay Time Δt

Figure 4.1: **Example of a typical pump-probe optical experiment.** The signal from the probe pulses is detected as the mechanical delay line is being scanned. By the relation $\Delta t = 2\Delta r/c$, c being the speed of light, the position change of the mechanical delay line is translated into a change of the time delay between pump and probe pulse. The measurements can be done in reflection or transmission mode.

1. The electrons of the material are warmed up due to the almost instantaneous absorption of the laser pulse energy (hundred of femtoseconds). The electromagnetic energy is absorbed by the electrons, as in the Drude-Lorentz model;

2. Electron-phonon thermalization is completed within the picosecond time scale;

3. The energy flows from the film to the substrate and, then, is dissipated through the thermal bath (nanosecond time scale).

The results illustrated in this chapter have been obtained using three different experimental setups [Ronchi et al. (2019)]:

1. (SU1) a pump supercontinuum-probe, based on white light (from 0.8 to 3.1 eV, generated by focusing a ~1 μJ energy/pulse in a 3-mm-thick sapphire window);

2. (SU2) pump-tunable probe setup, based on an Optical Parametric Amplifier (Optical Parametric Amplifier (OPA)).

   In both of these cases, a Regenerative Amplifier (Coherent RegA 9000), generating a train of ultrafast pulses (temporal width $\sim$ 50 fs) at 250 kHz with a wavelength $\lambda = 800$ nm and a ~6 μJ energy/pulse, has been used as a seed.

3. (SU3) a pump-probe setup, based on a Ti:sapphire cavity-dumped oscillator (Coherent Mira 900), to explore different repetition rates, from 250 kHz to 1 MHz.

In the setup SU1, the reflected probe beam is spectrally dispersed by an equilateral SF11 prism and focused on a Hamamatsu InGaAs linear photodiode array (PhotoDiode Array (PDA)), capturing the 0.8–2.5 eV spectral region. In configurations SU2 and SU3, the reflected probe is collected by a commercial Si or InGaAs photodiode. For single-color measurements, lock-in acquisition is used, together with fast (~60 kHz) modulation of the pump beam. This ensures a better signal-to-noise ratio with respect to spectroscopic measurements. Measurements with setups SU1 and SU2 were performed at the T-ReX facility at FERMI, Elettra (Trieste), while those with setup SU3 has been performed at ILAMP.

4.2 Results and discussion

Dynamics triggered by photoinduced orbital polarization change

The intrinsic nanotexture of the insulating phase unveiled by the XLD-PEEM experiment constitutes a natural template, which regulates the metallic nuclei formation and possibly affects their growth and expansion. The picosecond dynamics of the increase of metallic filling can be directly investigated in the time domain by time-resolved optical spectroscopy, which employs ultrashort light pulses to weaken the AFI phase and drive the temporal evolution of the metallic seeds. The excitation process can be understood starting from the following thermodynamic considerations. At the equilibrium temperature T, the distribution function of stable metallic nuclei, i.e., those with a volume of the order of the critical volume v_{cr}, is $f(v_{cr}) \sim exp(G_{cr}/kT)$, where G_{cr} is the energy barrier necessary to form a stable nucleus. This energy barrier, $G_{cr} = (g_M - g_I)v_{cr} + \alpha_{scr}$, is a balance between the volume energy gain to form metallic nuclei ($g_M < g_I$) and the surface energy loss associated with the surface tension (α_{cr})[Papon et al. (2006); E.M. Litshitz (1981)] and critical surface area (s_{cr}). The effect of the excitation with light pulses shorter ($\sim$ 50 fs) than the typical dynamics of the phase transformation and with photon energy ($\hbar\omega = 1.55$ eV) larger

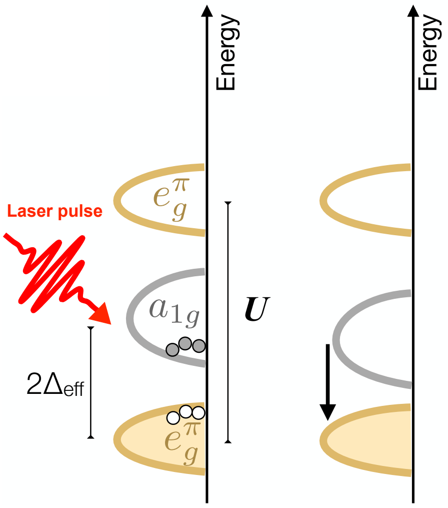

Figure 4.2: **Illustration of the photoexcitation across the Mott gap.** The change in the occupation of the a_{1g} and e_g^π orbitals gives rise to the orbital polarization change $\delta p = \delta(n_{e_g^\pi} - n_{a_{1g}})$), which triggers the growth of metallic seeds. Adapted from [Ronchi et al. (2019)].

than the charge gap is thus twofold. On the one hand, the energy absorbed is rapidly released to the lattice and leads to a quick increase (δT) of the local effective temperature within less than one picosecond [Mansart et al. (2010); Lantz et al. (2017)]. On the other hand, the impulsive photoexcitation modifies the population of the e_g^π and a_{1g} orbitals (sketch in Fig. 4.2, which constitutes the control parameter of the IMT [Lantz et al. (2017); Sandri and Fabrizio (2015); Ronchi et al. (2018)]. The light thus induces a change in the orbital polarization, $\delta p = \delta(n_{e_g^\pi} - n_{a_{1g}})$, that weakens the Mott insulating phase and drives a further decrease of the free-energy density difference between the insulating and metallic phases, as given by [Sandri and Fabrizio (2015); Ronchi et al. (2018)]

$$\delta(g_M - g_I) \sim -\frac{U}{2}\delta p \tag{4.1}$$

The light-induced increase of T and the simultaneous change of the orbital population is the microscopic mechanism that, in the I-M coexisting region, triggers the generation and growth of isolated metallic nuclei within the striped insulating domains. At high excitation fluence, the distribution of metastable metallic nuclei will eventually overcome the percolative threshold, thus leading to the formation of connected metallic networks and the emergence of mesoscopic conductivity.

Time-resolved reflectivity measurements in the low-fluence regime

Optical pump-THz probe experiments have been widely used [Liu et al. (2011); Abreu et al. (2015)] to probe the dynamics of mesoscopic metallization. When the absorbed pump energy overcomes the threshold necessary for inducing the IMT, the onset of a finite THz conductivity variation has been measured on a timescale of 50–100 ps [Abreu et al. (2015)]. Although THz frequencies are a direct probe of metallicity, the presence of domains smaller than the characteristic transport length scale, $L = \sqrt{D}/\omega$, where D is the diffusion coefficient, strongly affects the low-frequency (ω) conductivity [Henning et al. (1999)]. Therefore, THz properties do not exclusively depend on the metallicity, but also on the connectivity among the different metallic domains, which dramatically mutates across the IMT. As a direct consequence, the modeling of the low-frequency optical conductivity across the IMT in VO_2 and V_2O_3 requires a modified Drude model, which accounts for carrier localization in nanograins and directional scattering at the crossover between ballistic and diffusive electronic motion [Jepsen et al. (2006); Cocker et al. (2010); Luo et al. (2017)]. In this section, we decided to use optical spectroscopy in the infrared-visible range to probe the early dynamics of isolated metallic nanograins below the threshold necessary to induce mesoscopic metallization. As a consequence of the reduced characteristic transport length, visible light constitutes an extremely sensitive probe to bandstructure changes localized in isolated nanometric spatial grains, independently of the formation of percolative patterns. We also note that across the insulator-to-metal Mott transition, the spectral weight of the optical transitions involving the Hubbard bands mirrors the low-energy spectral weight of the Drude conductivity. The V_2O_3 optical properties in the visible range are dominated by the transition between the e_g^π LHB and upper UHB [Qazilbash et al. (2008); Stewart et al. (2012)], which is accounted for by a broad Lorentz oscillator centered at 2 eV. In Figg. 4.3 (a) and 4.3 (b), we report the equilibrium reflectivity variation measured at selected photon energies during the heating cycle, i.e., $[R(T,\omega) - R_M(\omega)]/R(T,\omega)$, where $R(T,\omega)$ is the generic temperature-dependent reflectivity and $R_M(\omega)$ is the reflectivity of the metallic phase, taken as the average of $R(T,\omega)$ between 190 and 250 K. Starting from the reflectivity of the insulating phase at $T = 120$ K, i.e., $R(120\ K,\omega) = R_I(\omega)$,

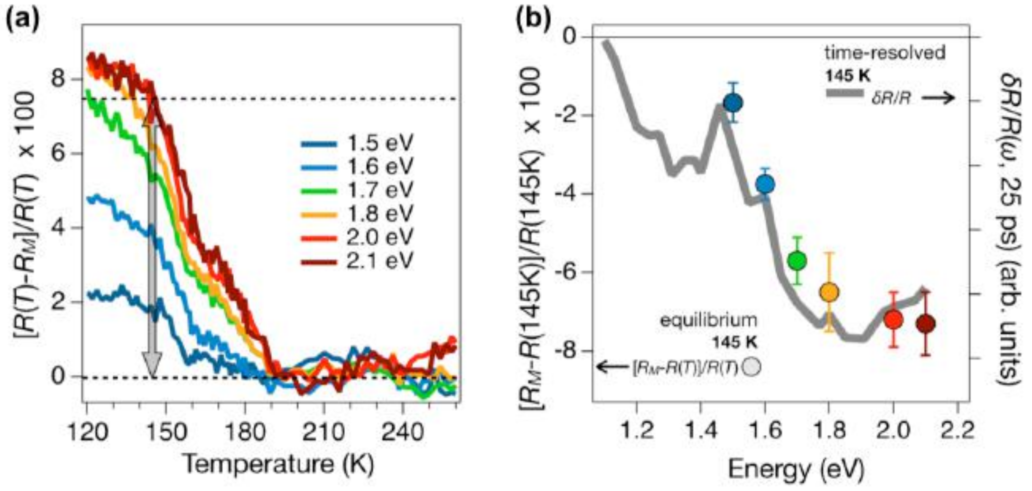

Figure 4.3: **Equilibrium infrared/visible reflectivity change during MIT.** (a) Equilibrium infrared/visible reflectivity change, $[R(T,\omega) - R_M(\omega)]/R(T,\omega)$ as a function of the sample temperature during a heating cycle. $R_M(\omega)$ is taken as the average of $R(T,\omega)$ between 190 and 250 K. The arrow and the dashed lines graphically show the procedure to obtain the value $[R_M(\omega) - R(145\text{K},\omega)]/R(145\text{K},\omega)$ reported in panel (b), for 2 eV (600 nm) photon energy. The measurements have been performed using setup SU3. (b) Frequency dependence of the equilibrium reflectivity change, $[R_M(\omega) - R(145\text{K},\omega)]/R(145\text{K},\omega)$ (colored dots, left axis), and of the time-resolved $\delta R/R(\omega)$ signal (gray line, right axis) measured at Δt = 25 ps and T = 145 K. The measurements have been performed using setup SU1. Adapted from [Ronchi et al. (2019)].

a maximum drop of ∼8% across the IMT is measured in the 1.8–2.1 eV photon-energy range, which corresponds to the e_g^π LHB → UHB transition. We can therefore conclude that the spectral weight variation at optical frequencies (1.4–2.2 eV) is a direct measure of the change of the metallic filling fraction and that broadband pump-probe reflectivity measurements can be used to snap the pump-induced growth dynamics of isolated metallic grains even at fluences much smaller than those necessary to overcome the latent heat and induce mesoscopic metallicity. More quantitatively, the pump-induced variation of the effective dielectric function, ϵ_{eff}, of an inhomogeneous phase can be modeled by the BEMA (see Appendix C), which correctly describes the percolative IMT in vanadates [Lupi et al. (2010); Jepsen et al. (2006); Bruggeman (1935)]. In general, for small filling-fraction variations (δF_M), the transient reflectivity change between the excited and equilibrium states can be linearized as follows:

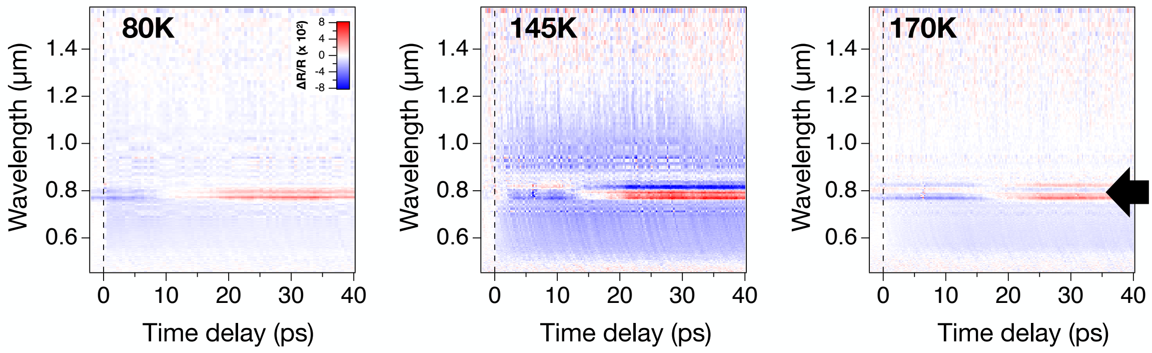

Figure 4.4: **Two-dimensional maps of the out-equilibrium reflectivity change made with Supercontinuum (SC) probe in visible/infrared range.** Frequency dependence of the out-of-equilibrium reflectivity change measured at T = 80, 145 and 170 K. The noise shown at 800 nm wavelength is due to the residual pump scattering (region indicated by the black arrow). The measurements have been performed using setup SU1, and an incident pump fluence of 0.3 mJ/cm^2, which corresponds to an absorbed energy E_{abs} = 13 J/cm^3.

$$\frac{\delta R}{R}(F_M,\omega,\Delta t) = \frac{R_{exc}(F_M,\omega,\Delta t) - R_{eq}(F_M,\omega)}{R_{eq}(F_M,\omega)} \simeq \Phi(F_M,\omega)\delta F_M(\Delta t), \tag{4.2}$$

where Δt is the delay between the pump and probe pulses, and $\Phi(F_M,\omega)$ is a function of both the initial filling factor and the probe frequency. In Appendix C, we demonstrate that $\Phi(F_M,\omega) \simeq [R_M(\omega) - R_I(\omega)]/R_I(\omega)]$ in the 1.4–2.2 eV region and for any initial F_M value. Therefore, we obtain that $\delta F_M(\Delta t) \simeq \delta R/R(\omega,\Delta t) \times R_I(\omega)/[R_M(\omega) - R_I(\omega)]$, where $[R_M(\omega) - R_I(\omega)]/R_I(\omega)$ is the relative reflectivity difference between the metallic and insulating phases, as obtained from the equilibrium reflectivity. In Fig. 4.3 (b) we report the $\delta R/R(\omega,\Delta t)$ signal measured at T = 145 K (δF_M = 0.01) as a function of the probe photon energy and at fixed delay time (Δt = 25 ps). The frequency dependence of the transient reflectivity variation perfectly reproduces the relative difference between the reflectivities measured at the equilibrium temperatures T = 145 and 200 K (see Fig. 4.3 (a)), thus experimentally proving that $\delta R/R(\omega,\Delta t) \propto [R_M(\omega) - R_I(\omega)]/R_I(\omega)$. In Fig. 4.4, the transient reflectivity variation is reported as a function of the supercontinuum (SC) probe wavelength and of the temperature in two-dimensional maps. These measurements

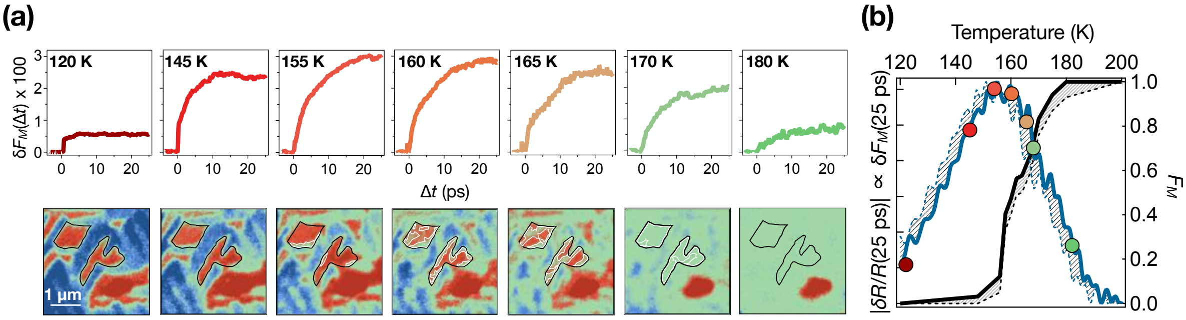

Figure 4.5: **Pump-induced filling-factor variation of metallic seeds.** (a) Top: Pump-induced filling-factor variation, $\delta F_M(\Delta t)$, at different temperatures below (120 K), within (145–165 K), and above (> 180 K) the I-M coexistence region. The measurements have been performed using setup SU2, with an incident pump fluence of 0.3 mJ/cm^2. Bottom: PEEM snapshots of the insulating nanotexture according with the temperature shown just above. (c) Absolute value of the long-time ($\Delta t = 25$ ps) reflectivity variation as a function of the temperature (blue line, left axis). The measurements have been performed using setups SU2 and SU3. The maximum reflectivity variation, (25 ps) $\simeq$ 2.2 $\times$ 10-3 at 2.1 eV (600 nm) photon energy, is measured at T $\simeq$ 155 K and corresponds to a filling-factor variation $\delta F_M \simeq 3\%$. The dashed area between the solid and dashed blue lines indicates the uncertainty ($\sim$ 4 K) in the actual sample temperature during the fast ramping up ($\sim$ 2 K/min) of the temperature of the sample holder. For the sake of comparison, the black line represents the metallic filling in the heating cycle as extracted from the XLD-PEEM images (see Fig. 3.2 (b)). The small mismatch between the temperatures at which vanishes ($\sim$ 190 K) and $F_M(t) \simeq 1$ ($\sim$ 180 K) is related to the finite resolution of the XLD-PEEM that is insensitive to insulating domains smaller than $\sim$ 30 nm. The gray dashed area between the solid and dashed black lines corresponds to the estimated uncertainty of $F_M(t)$ due to the finite PEEM resolution. See Appendix B.2 for a detailed discussion of the role of PEEM resolution in retrieving the $F_M(t)$ value from the pixel-segmentation analysis of the XLD-PEEM images. The colored dots indicate the temperatures of the XLD-PEEM images and time traces as reported in top panel (a). Adapted from [Ronchi et al. (2019)].

have been performed using setup SU1. At 145 K, the maximum of the out-of-equilibrium reflectivity change is focused on the wavelength range 550-1100 nm (1.1-2.2 eV), in good agreement with the results shown in 4.3 (b). The range of validity of Eq. (4.2) extends to δF_M values as large as 30%, as shown in Appendix B.2. On the other hand, considering that the photoinduced $\delta R/R(\omega, \Delta t)$ signal corresponds to a few percent of the static $[R_M(\omega) - R_I(\omega)]/R_I(\omega)$ difference and is measured with a signal-to-noise ratio of 10^{-6}, pump-induced changed of $F_M(\Delta t)$ as small as 10^{-4} are well within the experimental capability.

To address the connection between the spatial evolution and the temporal dynamics of the metallic seeds, we compare the outcomes of time-resolved optical spectroscopy and XLD-PEEM measurements performed on the same sample and in the same points of the hysteresis cycle. In Fig. 4.5 (a) we show the one-to-one correspondence between the real space XLD-PEEM images of the IMT and the time-resolved dynamics of $\delta F_M(\Delta t)$ during the heating cycle. In the time domain, the existence of stable finite-size metallic regions (white contours in XLD-PEEM images of Fig. 4.5 (a) bottom panel) for T $\geq$ 145 K corresponds to a slower buildup dynamics, i.e., to an increase of the time necessary to achieve the saturation of $\delta F_M(\Delta t)$, with respect to the dynamics measured at lower temperatures (120 K). In the I-M coexisting region, we also observe an increase of the long-time signal (δt = 25 ps) as shown in Fig. 4.5 (a) top panel. In Fig. 4.5 (b) we report the temperature dependence of (25 ps), which exhibits a clear maximum corresponding to the hysteresis region observed by XLD-PEEM. All the experiments have been performed with an incident pump fluence of 0.3 mJ/cm^2, which corresponds to an absorbed energy E_{abs} = 13 J/cm^3. We stress that the absorbed energy is significantly smaller than the threshold necessary to overcome the latent heat associated with the mesoscopic IMT, which ranges from $E_{th} \sim$ 110 J/cm^3 at 100–140 K to $E_{th} \sim$ 30 J/cm^3 at 160 K [Singer et al. (2018); Liu et al. (2011); Abreu et al. (2015)]. For this small value of absorbed energy, the maximum pump-induced temperature increase is limited to $\delta T \leq$ 4 K. At the same time, the light excitation induces an orbital polarization $\delta p \sim 3 \times 10^{-3}$, corresponding to a free-energy density variation $\delta(g_M - g_I) \simeq$ 4 meV, which largely overcomes the thermal effect $k_{\mathrm{b}}\delta T$. We thus conclude that the observed dynamics of $\delta F_M(\Delta t)$ is triggered by the impulsive change of orbital polarization and is related to the early-stage growth of isolated metallic domains.

Avrami model and ballistic growth of metallic droplets

The physical picture emerging from the combination of nanoimaging and picosecond dynamics of the IMT is the following: In the temperature range in which the average volume of the metallic domains is smaller than v_{cr}, the system is dominated by the formation of fluctuating small metallic nuclei, which are not captured by the static XLD-PEEM images. In this regime, the light excitation drives a rapid (< 5 ps) increase of the number of subcritical metallic nuclei, corresponding to $\delta F_M \sim 0.6\%$ (see Fig. 4.5 (b)). In the I-M coexisting region (T $\geq$ 145 K), the photoinduced orbital polarization δp triggers the growth of metallic seeds at the domain

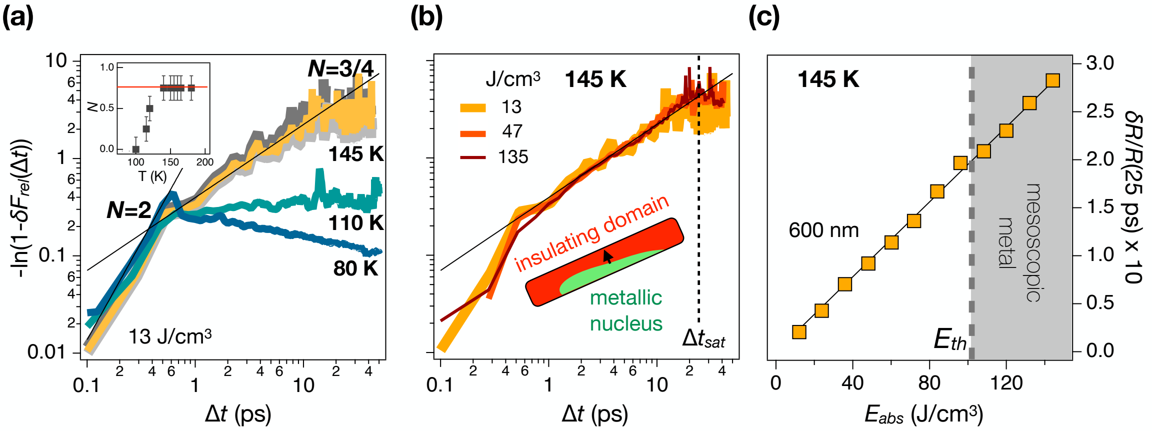

Figure 4.6: **Avrami model for the metallic growth.** (a) Avrami plot of the dynamics of $\delta F_{rel}(\Delta t) = [\delta R/R(\Delta t]/[\delta R/R(\infty)]$ at different temperatures. The value of $\delta R/R(\infty)$ is given by the asymptotic value of the exponential fitting to the data in the 0–20 ps time window. The gray traces represent the curves obtained assuming $\delta R/R(\infty) \pm 10\%$. The slope does not significantly depend on the value of $\delta R/R(\infty)$. The black lines indicate the expected curves for N = 2 and 3/4. Inset: Avrami coefficient N of the long-lived dynamics ($\Delta t > 1$ ps) as a function of the temperature. The red line indicates the asymptotic value N = 3/4. (b) Avrami plot of $\delta F_{rel}(\Delta t)$ at 145 K for different values of $\mathrm{E_{abs}}$. The solid black line indicates the expected curve for N = 3/4. The dashed line indicates the time at which the growth dynamics saturates. (c) The asymptotic value of the absolute relative reflectivity variation, i.e., $\delta R/R(25ps)$, measured at 600 nm wavelength and T = 145 K, is reported as a function of the absorbed energy density. The black thin line is the linear fit to the data. The dashed line indicates the energy threshold $\mathrm{E_{th}}$ above which THz mesoscopic conductivity has been observed [Abreu et al. (2015)]. The measurements reported in panels (a), (b), and (c) have been performed using setup SU2. Adapted from [Ronchi et al. (2019)].

boundaries, which overcome v_{cr} and irreversibly grow until they encounter the opposite edge of the monoclinic stripes. This process leads to the metallization of a small fraction of the insulating domains, such that the increase of the total metallic filling factor is of the order of $\delta F_M \sim 3\%$ (see Fig. 4.5 (b)). The nucleation and growth of a new phase at the cost of the initial one is usually described by the Avrami model [Avrami (1939, 1940, 1941)], which predicts that the relative filling-factor variation from the equilibrium value $F_M(0)$ to the steady state $F_M(0)+\delta F_M(\infty)$ takes the form $\delta F_{rel}(\Delta t) = \delta F_M(\Delta t)/\delta F_M(\infty) = 1 - \exp(K\Delta t^N)$, where K is a constant related to the growth rate and N is the Avrami coefficient, characteristic of the phase nucleation and growth mode. In Fig. 4.6 we plot the quantity $\ln(-\ln[1 - \delta F_{rel}(\Delta t)])$ as a function of the logarithmic time $\ln(\Delta t)$. The relative metallic filling is taken as the ratio between the reflectivity variation and its asymptotic value, i.e., $\delta F_{rel}(\Delta t) = [\delta R/R(\Delta t)]/[\delta R/R(\infty)]$. At very low temperature (T = 80 K, Fig. 4.6 (a)), we observe a rapid (0-500 fs) growth with N = 2, followed by a slow decay. While this fast dynamics is compatible with the sudden growth of two-dimensional domains with a rapidly exhausting nucleation rate [Papon et al. (2006)], the slow relaxation to the initial equilibrium condition, i.e., $F_M = 0$, indicates that the metallic nuclei never reach the stability threshold. This dynamics is likely associated with the nucleation of small droplets in the middle of the insulating stripelike monoclinic domains, which are then rapidly reabsorbed. When the temperature is increased, the dynamics of $\delta F_M(\Delta t)$ starts exhibiting the fingerprint of a long-lived growth of the metallic phase, under the form of a linear increase of the signal, in agreement with the prediction of the Avrami law: $\ln(-\ln[1-\delta F_{rel}(\Delta t)]) = \ln(K) + N\ln(\Delta t)$. The Avrami coefficient progressively increases (see the inset in Fig. 4.6 (a)) until it reaches a plateau in the I-M coexisting region (T $\leq$ 145 K), where the data show a linear behavior over more than one decade (1-20 ps). In this regime, the Avrami coefficient (N = 3/4) is close to unity, as expected for a martensitic transition [Cahn (1956)], in which the seeds of the new phase nucleate at the domain boundaries in the first instants and then grow with constant velocity along one direction. More specifically, the one-dimensional growth of boundary-pinned domains is characterized by N = 1 for pure interface-controlled growth and by N = 1/2 for pure diffusion-controlled growth [Papon et al. (2006)]. The experimental finding of N = 3/4 suggests that the interface-controlled dynamics retains some diffusive features, possibly related to the melting of spatially separated metallic droplets. We note that the simultaneous presence of the N = 2 and 3/4 dynamics in the time traces measured in the I-M coexisting region does not represent a transition between different nucleation and growth regimes, rather it demonstrates the simple coexistence of two independent phenomena, which are, respectively, the nucleation of small and unstable metallic droplets in the middle of the insulating monoclinic domains and the one-dimensional irreversible growth of metallic seeds nucleated at the domain boundaries. The growth of δF_M saturates after $\Delta t_{sat} \sim$ 25–30 ps (see the black dashed line in Fig. 4.6 (b)) from the impulsive excitation. Considering the sound velocity of V_2O_3 at 145 K, $v_s \sim$ 8 km/s [Abreu et al. (2017); Seikh et al. (2006)], Δt_{sat}corresponds to a typical length of 200–240 nm, which is very close to the average width of the striped monoclinic domains observed by XLD-PEEM in the AFI phase. This result suggests that the metallic growth is a ballistic collective process [Singer et al. (2018);

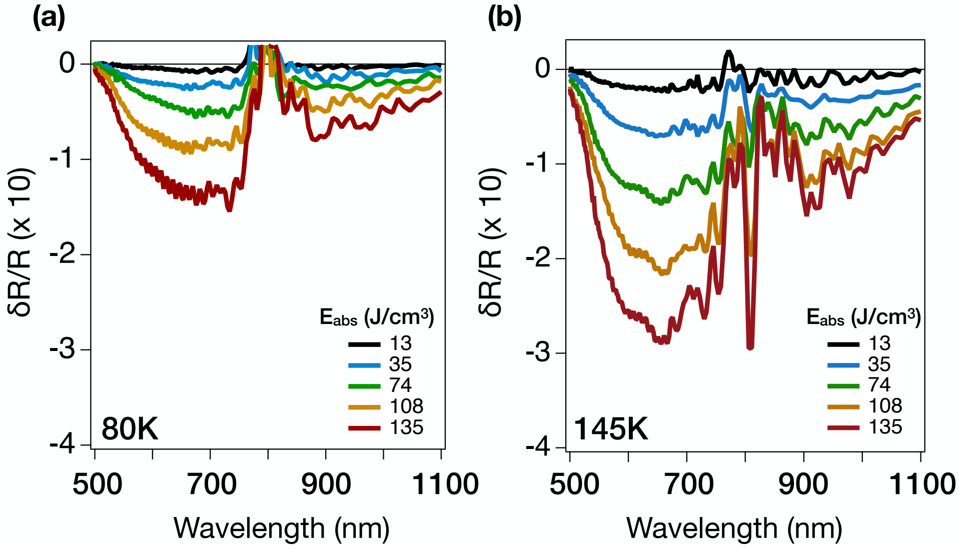

Figure 4.7: **Absorbed energy density dependence of the relative reflectivity variation spectrum** (a) The asymptotic value of the relative reflectivity variation, i.e., $\delta R/R(25\text{ ps})$ as a function of the wavelength 500-1100 nm (1.1-2.5 eV) at T = 80 K, for different absorbed energy density. (b) The asymptotic value of the relative reflectivity variation, i.e., $\delta R/R(25\text{ ps})$ as a function of the wavelength 500-1100 nm (1.1-2.5 eV) at T = 145 K, for different absorbed energy density. In both panels, it is possible to observe noise at 800 nm (1.5 eV) due to the scattering of the pump beam in the photodetector. The measurements reported in panels (a) and (b) have been performed using setup SU2.

Abreu et al. (2015)] in which the metallic domain expansion propagates at the sound velocity, until it encounters the edges of the striped monoclinic domains. An interesting insight into the nature of the nonequilibrium growth of metallic seeds is given by the fluence dependence of the dynamics. In the I-M coexisting region, the N = 3/4 coefficient is an intrinsic feature, which does not depend on the pump excitation fluence, as shown in Fig. 4.6 (b) for excitation densities as high as 135 J/cm^3. In Fig. 4.6 (c) we also report the asymptotic value of the absolute relative reflectivity variation $\delta R/R(25\text{ ps})$ measured at 600 nm wavelength, as a function of the absorbed energy. Surprisingly, $\delta R/R(25\text{ ps})$ scales linearly throughout the spanned E_{abs} range and does not exhibit any signature of discontinuity across $E_{th} \sim$ 110 J/cm^3, which is reported as the energy necessary to overcome the latent heat and to observe the onset of metallic THz conductivity [Abreu et al. (2015)] within 50–100 ps and the mesoscopic change of the lattice structure from low-temperature monoclinic to the high-temperature corundum [Singer et al. (2018)] on similar timescales. For sake of completeness, in Fig. 4.7 we report the asymptotic value of the wavelength-dependent relative reflectivity variation $\delta R/R(25\text{ ps})$ at 80 K and 145 K. The values plotted in Fig. 4.6 (c) are extracted from Fig. 4.7 (b). At 145 K, the linear behavior throughout the spanned $\mathrm{E_{Abs}}$ range is observed at all wavelengths.

Discussion

To rationalize the present results, it is instructive to give a closer look to the interplay between the lattice and the electronic band structure, as it emerges from calculations accounting for the on-site Coulomb repulsion U [Poteryaev et al. (2007); Grieger and Fabrizio (2015)]. If we consider the vanadium atoms, the high-temperature corundum lattice consists in shifted honeycomb planes stacked along the c axis (see Fig. 4.8 (a)). The hexagonal symmetry of the honeycomb planes preserves the degeneracy of the e_g^{π} and $e_g^{\pi *}$ orbitals, which are therefore equivalently occupied. The low- temperature monoclinic antiferromagnetic phase is the result of the breaking of the hexagonal symmetry (see Fig. 4.8 (a)), associated with the elongation of two edges of the hexagons (V_1-V_3), which leads to an overall increase of the unit-cell volume by 1.4% [McWhan and Remeika (1970); Dernier and Marezio (1970)]. The breaking of the hexagonal symmetry is accompanied by a tilt of the hexagons with respect to the honeycomb planes, which increases the distance of the V_1-V_2 dimers along the c-axis (see Fig. 4.8 (a)), without further affecting the unit-cell volume (for V_1-V_2 and V_1-V_3 nearest neighbour distances in the different V_2O_3 phases, the reader can refer to the Table 2.1 reported in Chapter 2). While the hexagonal symmetry breaking lifts the degeneracy of the e_g^{π} and $e_g^{\pi *}$ orbitals and modifies their population difference, the relative motion of the V_1-V_2 dimers affects the energy distance between the e_g^{π} and $\mathrm{a_{1g}}$ levels, which controls the metallicity of the system [Poteryaev et al. (2007); Grieger and Fabrizio (2015)]. Indeed, metastable metallicity in a lattice structure that retains the monoclinic distortion of vanadium hexagons has been predicted theoretically [Grieger and Fabrizio (2015)] and observed in V_2O_3 under high pressure [Ding et al. (2014)] and in VO_2 photoexcited [Morrison et al. (2014)] using a protocol similar to the present experiment. Our results are compatible with the following intriguing scenario [Grieger and Fabrizio (2015)]. The pump excitation induces a nonthermal increase of the $\mathrm{a_{1g}}$ occupation accompanied by the simultaneous depletion of an equal amount of electrons occupying the two e_g^{π} orbitals, i.e., $\delta n_{e_g^{\pi}} \simeq \delta n_{e_g^{\pi *}} \simeq \delta n_{a_{1g}}/2$. The photoexcitation thus induces a sudden change of the orbital polarization δp, which can

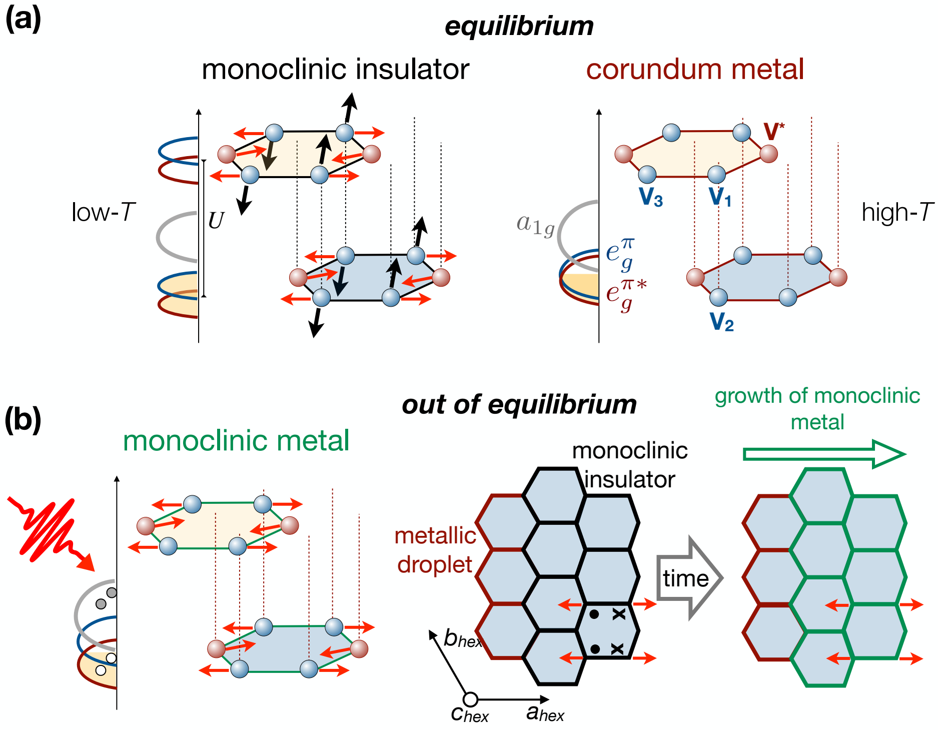
(a)
equilibrium
monoclinic insulator
corundum metal
low-T
U
a_{1g}
e_g^π
$e_g^{\pi *}$
V*
V3
V1
V2
high-T
(b)
out of equilibrium
monoclinic metal
growth of monoclinic metal
monoclinic insulator
metallic droplet
time
b_{hex}
c_{hex}
a_{hex}

Figure 4.8: **Illustration of the nonequilibrium metallic growth dynamics.** (a) Sketch of the stacked honeycomb planes in the low-temperature monoclinic and high-temperature corundum phases. In the corundum metal, the hexagonal symmetry preserves the equivalence of the V (blue) and V (red) sites and, therefore, of the two degenerate e_g^π and $e_g^{\pi *}$ orbitals. In the monoclinic insulating phase, the distortion of the hexagons (red arrows) lifts the e_g^π degeneracy, whereas the out-of-plane motion of the vanadium atoms (black arrows), associated with the tilting of the hexagons, controls the $\mathrm{a}_{1\mathrm{g}}$-e_g^π energy distance. (b) Sketch of the possible transient metal-like monoclinic state. The photoinduced change of $\delta(n_{e_g^\pi} - n_{a_{1g}})$ triggers the restoring of the nearest neighbour V_1-V_2 distance (tilting back of the hexagons), whereas it does not affect the in-plane hexagonal distortion. Photoexcitation thus triggers the growth of already formed metallic droplets via the propagation of a transient nonequilibrium lattice rearrangement (monoclinic metal). The black, red, and green borders of the hexagons indicate the monoclinic insulator, the corundum metal, and the monoclinic metal, respectively. The red arrows indicate the in-plane distortion of the hexagons, whereas the dots (crosses) indicate the out-of-plane inward (outward) motion of the vanadium atoms associated with the hexagons tilting. Adapted from [Ronchi et al. (2019)].

lead to the transient collapse of the insulating band structure [Sandri and Fabrizio (2015)], but it does not significantly alter the population difference between the two e_g^π orbitals and, as a consequence, does not affect the potential that stabilizes the monoclinic distortion of the vanadium hexagons [Grieger and Fabrizio (2015)]. Within this picture, the pump excitation can trigger the rapid (0-30 ps) proliferation and growth of metallic regions that exhibit transient metal-like electronic properties and a nonthermal lattice structure, obtained by restoring the V_1-V_2 dimers distance (tilting back of the hexagons) at constant volume while retaining the monoclinic distortion of the vanadium hexagons (see Fig. 4.8 (c)). Once the metastable metal-like nuclei have filled the striped monoclinic domains, the excess energy stored in the system drives the slower (50–100 ps) first-order transition into the corundum metal [Singer et al. (2018)], which involves the restoring of the hexagonal symmetry and the volume decrease of the unit cell. This slower process triggers the melting of the isolated metallic grains into a percolative network with mesoscopic metallic properties in the THz [Abreu et al. (2015)]. The final stage of the metallization thus consists of the two-dimensional growth of mesoscopic metallic puddles, described by the N = 2 Avrami coefficient, as measured by optical pump-THz probe spectroscopy [Abreu et al. (2015)]. This multistep picture of metallic growth is supported by recent time-resolved X-ray diffraction experiments [Singer et al. (2018)] that unveiled the fast onset ($\sim$ 2.5 ps) of a precursor nonthermal structural change of the honeycomb planes triggered by light excitation. This structural dynamics, which is continuous in the excitation energy, preserves the unit-cell volume and propagates at the sound velocity. When the excitation energy overcomes the latent heat, the precursory nonthermal lattice dynamics is followed by the mesoscopic transformation into the equilibrium metallic corundum structure.

4.3 Conclusion

In conclusion, our results show that the insulating domain boundaries host the birth of metallic seeds, whose expansion can be triggered by the impulsive photoinduced change of the orbital population. The timescale of the growth process (25-30 ps) corresponds to the propagation at the sound velocity across the transverse dimension (i.e. the width of the domain) of the insulating stripes. Our results show that this nanotexture strongly affects the nucleation and growth dynamics of metallic grains. Our data point toward a nonthermal scenario, in which the expanding metallic grains transiently retain the in-plane distortion of the vanadium hexagons typical of the AFI phase. The use of XLD-PEEM for the study of nanotextured phases can be readily extended to many different d- or f-shell correlated materials. The dynamical processes unveiled by our work also impact the modeling of the electrical breakdown in Mott insulators [Stoliar et al. (2013)]. Our results suggest that each node in the resistor network corresponds to an insulating nanodomain with a well-defined orientation of the monoclinic distortion, and they show how the node metallizes by light excitation. The possibility of suitably engineering the lateral size of the nanotextured insulating domains in thin films is key to controlling the electronic and magnetic switching of Mott insulators at THz frequencies, with impact on the development of novel Mottronics devices [Tokura et al. (2017)].

Chapter 5

Evidence of transient monoclinic metal-like state in V_2O_3

This chapter has been adapted from the publication:

"Photoinduced transient monoclinic metal-like state in V_2O_3 stabilized by nanotexture"
A. Ronchi, P. Homm, M. Menghini, P. Franceschini, F. Maccherozzi, A. Fitzpatrick, F. Banfi, G. Ferrini, F. Cilento, F. Parmigiani, S.S. Dhesi, M. Fabrizio, J-P. Locquet, and C. Giannetti

(in preparation)

In this chapter, we present the preliminary results obtained during the beamtime at beamline i06 (DLS, UK) in June 2019. The experiment was very complex as it was the first attempt of performing tr-PEEM on V_2O_3. Generally, this kind of out-of-equilibrium experiments need a high control of all experimental parameters since a prerequisite is to have spatial and temporal coincidence between pump and probe. In our case, the setup of the experiment required two different beamtimes (2018 and 2019) to reach the optimal conditions. The experiment has been proposed to address the possibility of driving a purely electronic, metastable and reversible switching of the conductive state (monoclinic metal) in V_2O_3, as already discussed in Chapter 4. We discovered that after the pump-induced excitation the in-plane monoclinic nanotexture is retained although the laser fluence was above the threshold to optically drive the system in a complete metallic state. This intriguing result suggests the possibility to partially decouple the SPT from the IMT. The results are expected to impact the modelling of the non-thermal switching in Mott insulators and to boost the opto-electric ultrafast control of correlated materials at THz frequencies.

5.1 Experimental technique: tr-PEEM

During the beamtime, we exploited the PEEM time-resolved setup of the I06 beamline to investigate the temporal dynamics of the low-temperature spatial inhomogeneities in a V_2O_3 thin film after a pulsed laser photoexcitation (photon energy 1.5 eV, rep. rate 266.9 kHz). Indeed, the aim of the experiment was to determine whether there is a *melting* of antiferromagnetic (AF) domains induced by an external optical pump above the threshold to photoinduced the IMT. In order to carry out a time-resolved PEEM experiment, it was necessary to exploit the synchrotron hybrid mode scheme (see Fig. 5.1). In this configuration, single pulses with higher brilliance also circulated in the synchrotron ring together with the normal X-rays multibunches. The temporal width of the single X-ray pulse was 100 ps, which set the temporal resolution of the experiment. The temporal coincidence is obtained when the pump laser pulses are synchronized with the X-ray single pulses, and to do that, it was possible to modify the relative delay by acting on the opto-acoustic mirror of the cavity. This changes the phase through which the pump pulses are released from the laser cavity. The experimental measurements have been carried out on a 51 nm V_2O_3 film on (0001)-sapphire substrate, grown and characterized by the laboratory of Solid State Physics and Magnetism of KU Leuven (for a detailed discussion on the structural and electrical characterization of the film, see appendix A).

The two main experimental challenges we had to face were 1) the estimation of the spot size of the pump laser beam at the sample's surface 2) the temporal and spatial coincidence between the near-IR pump and X-ray probe. The first step has been to estimate the pump spot size. A rough or wrong estimation of the spot dimension could significantly overestimate/underestimate the incident fluence on the sample and it could

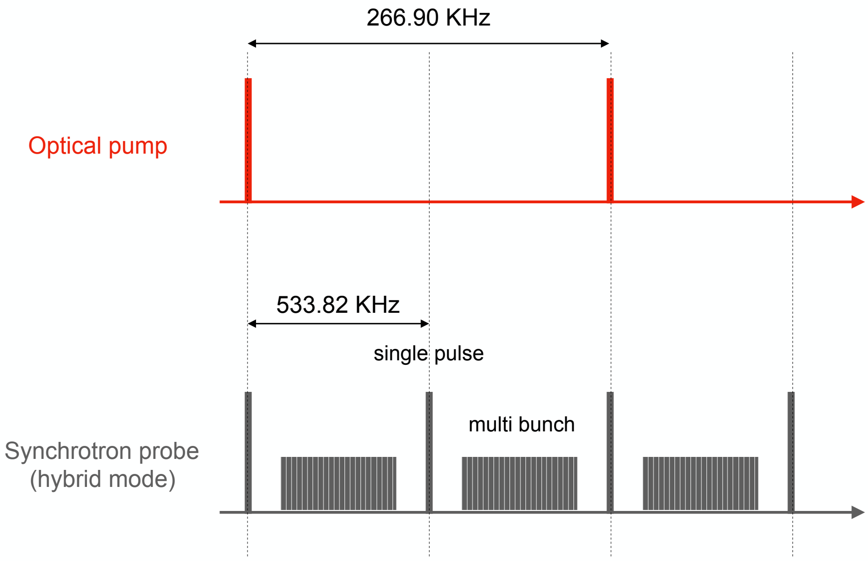

Figure 5.1: **Sketch of synchrotron hybrid mode configuration.** Top: The optical pump deliver near-infrared laser pulses at 1.5 eV (800 nm) with a repetition rate of 266.90 kHz. This frequency has been chosen to be exactly half of the frequency of the single pulse synchrotron probe. Therefore, for each pump pulse, there are two X-rays probe pulses. Bottom: Tr-PEEM requires the synchrotron working in hybrid mode. In this configuration, single pulse with $\sim$ 100 ps time resolution were circulating in the ring together with the normal X-rays multibunches. An electronic gate permitted to filter away the multi bunches. The single pulse frequency was 533.82 kHz.

prevent having enough optical excitation to overcome the threshold of the IMT transition. The main difficulty in estimating the pump spot size, and therefore the pump fluence, was related to the impossibility of placing a beam profiler into the vacuum chamber at the sample position. Fortunately, when the laser shined on some particular surface impurities, there was a pump-induced non-linear photoemission effect. First of all, this ensured that the laser was arriving on the sample in the same FOV as the PEEM images (i.e. spatial coincidence). Secondly, by moving the in-plane sample position, we performed a raster scan of the intensity of the pump-induced non-linear photoemission and since the impurity is much smaller than the laser spot, we could reconstruct the laser profile (see Fig. 5.2 (a)). In Fig. 5.2 (b) we plotted the integrated line profiles of the gray areas (LP0 and LP1) in panel (a) with their respective Lorentzian fit (red solid line, Fig. 5.2 panel (b)). The procedure allowed to determine a slightly elliptical spot size of (96 ± 2) μm x (110 ± 5) μm. The laser power (up to $\sim$ 480 mW) has been measured with a power meter before entering the vacuum chamber, and we have taken into account even the losses of the windows and of the focusing lens inside the vacuum chamber. According to the above information, we have been able to estimate the incident pump fluence on the sample, which was at maximum 22 ± 4 mJ/cm^2.

To get closer to the temporal coincidence between the near-IR pump and X-ray probe we used fast photodiodes in the vacuum chamber (temporal resolution $\sim$ 100 ps). We used two different photodiodes and, then, the difference is calculated in optical path. This method allowed us to get relatively close to the temporal coincidence. By the way, the photo-induced non-linear photoemission intensity I_{NLP} was reduced while the near-IR pump and X-ray single pulse were coincident. By changing the laser phase shift we were able to reconstruct the cross-correlation between pump and probe pulses by measuring the intensity of the non-linear photoemission I_{NLP} (see solid grey line in Fig. 5.2, panel (c)). In the inset, it is possible to observe the real-space temporal evolution of the pump-induced non-linear photoemission from the small surface defect before, during and after the coincidence with the X-ray single pulse. The minimum of the I_{NLP} has been set as the time zero of the time-resolved PEEM experiment.

Once optimized the procedures to find the spatial and temporal overlaps and to measure the pump spot size on the sample, as a second step, we performed time-resolved XLD experiment at two energies (519.9 eV, 518 eV), 1 polarization (Linear Horizontal (LH)) at different time delays with respect to the laser pump excitation. The temporal dynamics of the PIPT has been followed within a temporal window spanning up to 7 ns. For each time delay, the final PEEM image was the result of an average of 4 sets of 40 images each (10 sec acquisition time per image), thus about 40 minutes for each time delay. Each set of 40 images has been collected within a sequence of not-ordered different time delays, to avoid experimental fluctuations (drift of the sample, change in the X-ray intensity, etc...) that were possible due to the long exposition time. In addition, for each sequence of positive delays we took a negative delay (image taken before time zero) reference image, which was used to compensate for possible background variations. In addition, the image at negative delay is chosen as a reference because it represents the unperturbed state of the system, in which the pump excitation is not arrived yet on the sample.

A typical example of PEEM image obtained from this data collecting protocol is shown in Fig. 5.2 (d). In the images it is possible to distinguish the

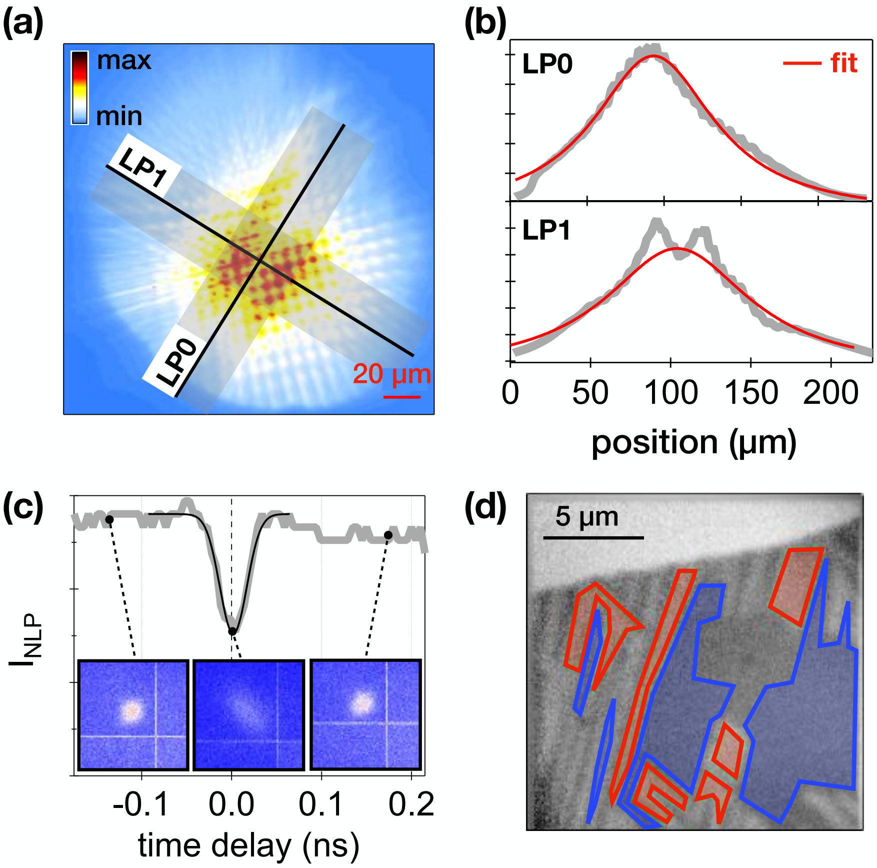

Figure 5.2: **Temporal and spatial characterization in tr-PEEM experiment.** (a) Image representing the reconstruction of the laser spot by means of the non-linear photoemission from a defect present on the surface of the sample. LP0 and LP1 gray areas represent the integrated regions used to obtain the line profiles in panel (b). (b) Line profiles (solid gray) and Lorentian fit (solid red) of the gray areas in panel (a). (c) Intensity of the pump-induced non-linear photoemission $\mathrm{I_{NLP}(t)}$. The minimum of the total intensity is shown in correspondence with the temporal coincidence between the near-IR pump and X-ray probe (i.e. time zero). Inset: Image of the integrated area used to obtain the total intensity $\mathrm{I_{NLP}(t)}$. At t = 0 ns, the pump-induced non-linear photoemission $\mathrm{I_{NLP}(t)}$ has its minimum, since the spot disappears. (d) Example of the tr-PEEM image obtained from the acquisition protocol described in the main body of the text. The red and blue areas represent, respectively, the regions of maximum (I_{XLD}^{light}) and minimum (I_{XLD}^{dark}) XLD contrast used to extract the relative contrast variation $\Delta I_{XLD}(t)$ between neighbouring monoclinic domains.

same monoclinic domains already described in chapter 3. These monoclinic domains present the same nominal size and shape previously observed and discussed. To investigate the pump-induced melting of the monoclinic domains, we decide to apply the following protocol. First of all, for each set of PEEM images (corresponding to chosen time delays), we decided to consider the same dark and light grey areas. This permitted to compare always the same regions. An example is shown in Fig. 5.2 (d), in which red areas identify light domains, whereas blue areas dark domains. The different domains, as already explained in Chapter 3, are characterized by two different in-plane monoclinic orientations. Then, let us define the contrast between dark and light domains as

$$\delta I_{XLD} = |I_{XLD}^{dark} - I_{XLD}^{light}| \tag{5.1}$$

where I_{XLD}^{dark} and I_{XLD}^{light} are, respectively, the XLD intensities of the blue and red areas in Fig. 5.2 (d). Please remember that dark domains mean negative I_{XLD}, while light domains mean positive I_{XLD}. Therefore, their difference gives always the drop of contrast between the domains. Finally, the relative contrast variation (%) shown in Fig. 5.4 (a) is the result of the re-normalization with respect to the negative time delay PEEM image of each delays sequence and it is defined as

$$\Delta I_{XLD}(t) = \frac{\delta I_{XLD}(t) - \delta I_{XLD}(t < t_0)}{\delta I_{XLD}(t < t_0)} \cdot 100 \tag{5.2}$$

where $\delta I_{XLD}(t < t_0)$ is the contrast between dark and light domains at negative time delay. The error bars shown in Fig. 5.4 (a) have been calculated by considering the standard deviation of $\delta I_{XLD}(t < t_0)$ for all the negative delays acquired during the experiment. The error is ± 3 %.

5.2 Results and discussion

Photoinduced transient monoclinic metal-like state stabilized by nanotexture

In this experiment, we performed the first time-resolved measurements of the dynamics of the monoclinic domains in V_2O_3. More specifically, we used

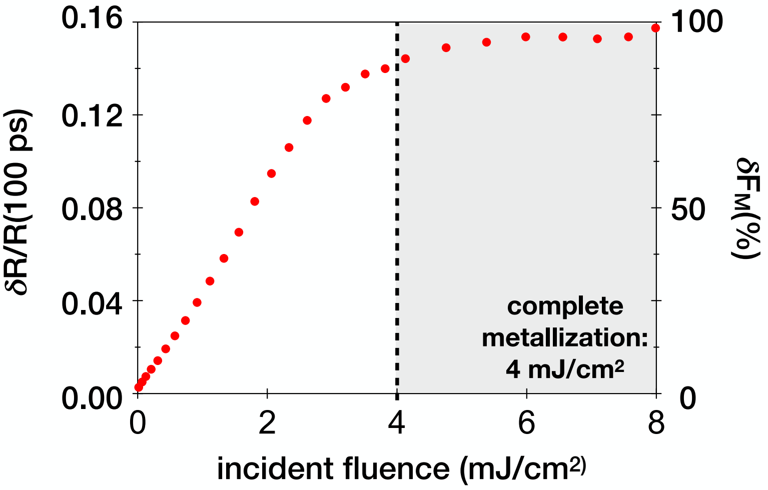

Figure 5.3: **Pump-induced metallic filling fraction vs pump incident fluence at 100 K.** Relative variation of reflectivity $\delta R/R$ measured at 100 ps delay time vs pump incident fluence. The pump's wavelength was 800 nm with a FWHM of 50 μm, whereas the probe's wavelength was 515 nm with a FWHM of 10 μm. The repetition rate of both laser beam was pre-set at 10 kHz to avoid Joule heating effect. As explained in Chapter 3 the $\delta R/R$ is proportional to the metallic filling fraction $\delta F_M(\%)$. Above 4 mJ/cm^2 of incident fluence, the $\delta R/R(100$ ps) saturates, this means that the system has reached the complete metallization.

ultrashort light pulses (<100 fs) in the infrared (1.5 eV) to photoinduce the IMT at temperatures T = 100 K ($T_C \sim 135$ K). The pump incident fluence was the maximum available, 22 mJ/cm^2. Fig. 5.3 shows the transient relative variation of reflectivity $\delta R/R$ at 100 ps delay as a function of the pump incident fluence. These measurements have been performed on the same sample in ILAMP laboratories in Brescia before the DLS experiment. Above 4 mJ/cm^2 it is possible to observe the saturation of the $\delta R/R$ (100 ps) $\simeq \delta F_M$ indicating the complete metallization of the system. This ensures that the fluence used in the DLS experiment was sufficient to photoinduce a complete IMT. The main achievements obtained from the beamtime 2019 are the following:

1. Even a pump excitation at absorbed fluences larger than those necessary (4 mJ/cm^2) to observe the complete IMT in all-optical pump-probe experiments, results in a partial quench (<25%, see Fig. 5.4, panel (a)) of the XLD contrast between neighboring domains. No dynamics of the domain topology is clearly visible by comparing PEEM images before and after photoexcitation (see Fig. 5.4 panel (b)).

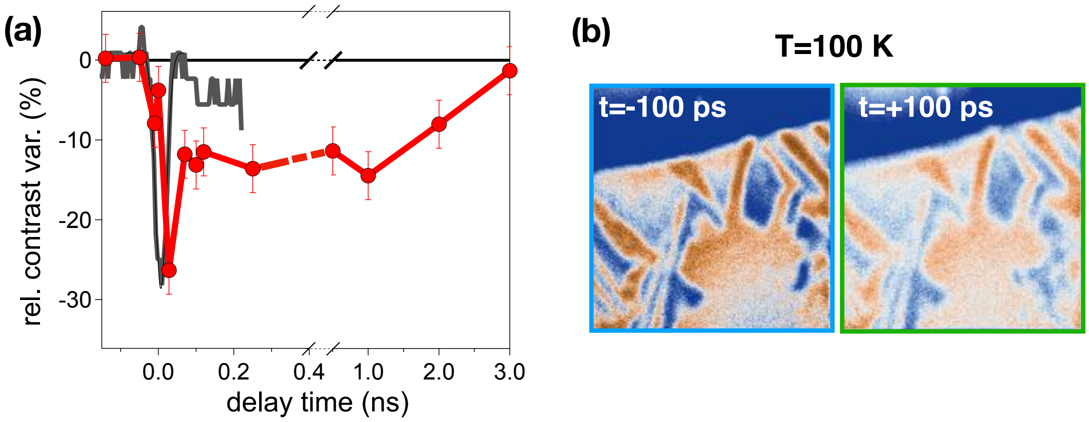

Figure 5.4: **Photoinduced dynamics of the monoclinic domains at 100** K. (a) The dynamics of the relative contrast (red dots) between neighboring domains. The error is ± 3 %. The exact procedure to obtain the point and their relative errors have been described in the main body of the text. The black line is the cross-correlation signal between the laser and synchrotron pulses. (b) PEEM images at negative and positive delay times.

These results strongly suggest that the in-plane monoclinic distortion is preserved during the photo-induced IMT. This result is in good agreement with previous works showing the possibility to observe a monoclinic metal phase [Singer et al. (2018); Grieger and Fabrizio (2015)]. We stress the fact that we are performing an out-equilibrium experiment in which the behavior of the system can be drastically different with respect to the steady-state approach. Consequently, contrary to what is observed under steady-state in very recent works [Kalcheim et al. (2019); Frandsen et al. (2019)], the out of equilibrium approach can reveal decoupling between the MIT and the SPT.

2. The cooling back of the system is observed within about 2 ns. This aspect is reasonable and in accordance with the previous time-resolved measurements which show on similar samples that the system returns to its pre-excitation state on the nanosecond time scale [Liu et al. (2011); Abreu et al. (2017). The numerical simulations in Chapter 5 confirm this recovering time scale.

To address the interplay between the underlying monoclinic nanotexture and the possibility of creating a transient metallic state which retains the in-plane monoclinic distortion, we introduce here the simplest functional describing the first order insulator to metal transition. Let's introduce

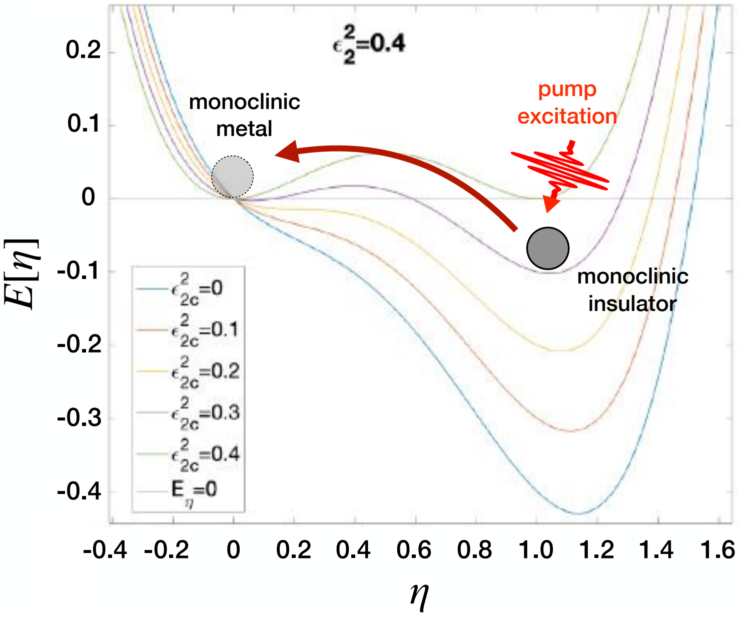

Figure 5.5: **Ginzburg-Landau free energy.** Example of a plot of the GL free energy as a function of the elongation η for a fixed in-plane strain ϵ_2^2=0.4 changing the parameter ϵ_{2c}^2. If the latter is zero (blue curve) the system is definitely in a monoclinic insulating phase. If ϵ_{2c}^2 is increased the energy of the insulating phase progressively increase, until, a monoclinic metallic ($\eta \simeq 0$) minumum appears in the purple and green curves. The increasing of the value ϵ_{2c}^2 simulates the effect of the pump-induced photoexcitation (sketch). Adapted from [De Poli (2020)].

the order parameter η, which can be thought as associated to the out-of-plane elongation of the vanadium dimers (see Fig. 4.8, Chapter 4) and it is believed to be at the origin of the metallicity [Poteryaev et al. (2007); Grieger and Fabrizio (2015)]. We can thus write the following Free Energy density:

$$E[\epsilon_2, \eta] = \alpha\eta^2(\eta - \eta_o)^2 - (\epsilon_2^2 - \epsilon_{2c}^2)\eta \tag{5.3}$$

which is a functional of the spatially dependent shear strain $\epsilon_2(r)$, obtained from the minimization of Eq. 3.2 (already discussed in Chapter 3), of the parameter $\eta(r)$ and of the parameter ϵ_{2c} which will be discussed in the following. For sake of simplicity, let us discuss the homogeneous case, i.e. we consider spatially independent η and ϵ_2, with $\epsilon_{2c} = 0$. The functional 5.3 displays two minima: the metallic one at $\eta = 0$ and the insulating one at $\eta = \eta_0$. The energy minimum of the insulating phase is lower than the metallic one only when $\epsilon_2 > 0$, i.e. when the the systems starts developing the monoclinic distortion. In this condition, we reproduce a transition from a metallic corundum ($\eta = 0$, $\epsilon = 0$) to a monoclinic insulator ($\eta \neq 0$, $\epsilon_2 \neq 0$). Nonetheless, the MIT is a first-order transition, which implies the existence of a parameter space region in which the two metallic and insulating minima can exist, although with different relative energy. In order to reproduce such a behaviour, we introduce the parameter ϵ_{2c}, which defines a region ($\epsilon_2^2 < \epsilon_{2c}^2$) where the metallic solution is the absolute minimum of the energy, although with non-zero shear strain ($\epsilon_2^2 \neq 0$). The critical parameter ϵ_{2c} thus regulate the existance of a monoclinic metallic solution for shear strain smaller than the critical value.

We will now use the functional 6.3 to describe the photo-induced metallization process triggered by the pump excitation. As discussed in Chapter 4, the light excitation at 1.5 eV is able to induce an orbital polarization δp, which modifies the free energy difference between the insulating and metallic states: $\delta E = -U/2 * \delta p$. Following the discussion above, a pump-induced change of the energy difference between the insulating and metallic states can be mimicked by assuming a fluence-dependent $\epsilon_{2c}(f_p)$, where f_p is the pump fluence. We now start from the equilibrium insulating phase, corresponding to a large value of $\epsilon_2^2 - \epsilon_{2c}^2$ such that no metallic minimum at $\eta = 0$ exists (blue line in Fig. 5.5). The pump excitation induces an increase of ϵ_{2c} and a corresponding decrease of $\epsilon_2^2 - \epsilon_{2c}^2$ up to the point that the metallic minimum at $\eta = 0$ appears (green and purple lines in Fig. 5.5). In this case, we have the possibility of inducing a metallic state with monoclinic shear strain which represents what has been observed in the experiments. The crucial observation which makes such a simple empirical model a realistic description of the photo-induced metallization process, is the underlying existence of the monoclinic nanotexture characterized by nanometric domains with monoclinic distortion along the three different equivalent monoclinic axes (see Fig. 3.2, Chapter 3). As previously discussed in Chapter 3, the boundaries between different domains are inherently constrained to zero shear strain ($\epsilon_2 = 0$). As a consequence, independently of the smallness of the parameter ϵ_{2c}, at the domain boundaries the strain will be always smaller than the critical value, thus engendering the growth of metallic regions with non-zero shear strain. This simple model thus highlights the role of the intrinsic nanotexture of the monoclinic phase in the photo-induced metallization process. The existence of zero-strain boundaries stabilizes the monoclinic metallic phase thus seeding the birth and growth of metallic monoclinic domains which eventually fill the entire volume when the pump excitation is large enough.

Our results also provide a new tool for controlling the emergence of the non-thermal metallic phase with monoclinic shear strain. Controlling the nanotexture and the domains size, for example via strain engineering, allows to manipulate the transient non-thermal state with impact on devices based on the ultrafast insulator-to-metal transition [Yang et al. (2011); del Valle et al. (2018); Tokura et al. (2017); Basov et al. (2017)].

5.3 Conclusion

In this chapter, we have presented the preliminary results obtained during the beamtime at beamline i06 (DLS, UK) in June 2019. The experiment was the first attempt at performing tr-PEEM on V_2O_3. The experiment has shown the possibility of driving a purely electronic, metastable and reversible switching of the conductive state (monoclinic metal) in V_2O_3. We demonstrated that after the pump-induced excitation the in-plane monoclinic nanotexture is retained although the laser fluence was above the threshold to optically drive the system in a complete metallic state. This intriguing result suggests the possibility to partially decouple the SPT from the IMT. Preliminary result of a numerical model has been presented in support of this scenario. The results are expected to impact the modelling of the non-thermal switching in Mott insulators and to boost the opto-electric ultrafast control of correlated materials at THz frequencies.

Chapter 6

Non-thermal light-assisted resistance collapse in a V_2O_3-based Mottronic device

This chapter has been adapted from the publication:

"Non-thermal light-assisted resistance collapse in a V_2O_3-based Mottronic device"
A. Ronchi, P. Franceschini, P. Homm, M. Gandolfi, G. Ferrini, S. Pagliara, F. Banfi, M. Menghini, J-P. Locquet, and C. Giannetti
(submitted to Phys. Rev. Applied)

In the last decades, much effort has been so far dedicated to the study of the transient optical, electronic and lattice properties [Mansart et al. (2010); Liu et al. (2011); Abreu et al. (2015); Morrison et al. (2014); Abreu et al. (2017); Lantz et al. (2017); Ronchi et al. (2019); Otto et al. (2019); Giorgianni et al. (2019)] of V_2O_3 and on the role of intrinsic nanoscale inhomogeneities [Lupi et al. (2010); McLeod et al. (2016); Ronchi et al. (2019)] with the goal of clarifying to what extent the photoinduced transition is similar to the thermally driven one. In contrast, little is known about the actual resistive state that is induced by the light excitation possibly combined with external voltage application. Recent theoretical works have suggested that, in the vicinity of the insulator-metal coexisting region, the application of voltage [Mazza et al. (2016)] and the excitation with light pulses capable of manipulating the band occupation [Sandri and Fabrizio (2015); Ronchi et al.

(2019)], can lead to the weakening of the insulating state and, eventually, to the complete Mott gap collapse and resistive switching along a non-thermal pathway.

In this chapter, we developed a Mottronic device, based on a micro-bridged V_2O_3 epitaxial thin film, in which the resistivity state consequent to a controlled excitation by trains of ultrashort pulses can be measured. V_2O_3 is a prototypical Mott insulator that exhibits a first-order Insulator-to-Metal transition (IMT) occurring at $T_{IMT} \sim 170$ K and characterized by a resistivity change of several orders of magnitude [McWhan et al. (1969); Jayaraman et al. (1970); Limelette et al. (2003)]. At $T > T_{IMT}$, our device undergoes a resistive switching process, i.e. the resistance drops to the metallic value, at a temperature-dependent threshold voltage V_{th}. However, the switching process in V_2O_3 devices is associated to the formation of micrometric conductive filaments [Kalcheim et al. (2020)], which usually make the evaluation of the local heating and the investigation of the thermal nature of the dynamics rather difficult. In order to avoid this additional complexity, we investigate the light-induced volatile resistance drop for different applied voltages, always smaller than V_{th}. This below-threshold volatile resistance drop thus provides information about the homogeneous weakening of the insulating phase triggered by the voltage/light excitation. Starting from the resistance vs temperature calibration curve of the device, we are able to compare the photoinduced resistivity drop to the local heating effect, which is carefully estimated by finite-element simulations. Our main results can be summarized as follows: i) the application of a sufficiently long train of light pulses alone drives a volatile resistance drop that is compatible with that predicted by finite-element simulations of the thermal problem. The minimum number of pulses necessary to observe a significant effect suggests that the light-induced local heating is mediated by the electronic specific heat, which becomes extremely large as T_{IMT} is approached; ii) when a significant below-threshold electrical bias ($V = 0.5$ V) is applied, the volatile resistivity drop induced by the train of light pulses exceeds what is observed in the absence of applied bias and what is predicted by thermal simulations which also account for Joule heating. This result leads to the conclusion that the combined voltage/light excitation protocol makes the collapse of the insulating electronic phase easier.

6.1 Experimental details

6.1.1 Device fabrication

A 67 nm epitaxial V_2O_3 film is deposited by oxygen-assisted molecular beam epitaxy (MBE) in a vacuum chamber with a base pressure of 10^{-9} Torr. A 37 nm Cr_2O_3 buffer layer is interposed between the film and the substrate to minimise lattice mismatch and optimise strain relaxation in the film. A (0001)-Al_2O_3 substrate is used without prior cleaning and is slowly heated to a growth temperature of 700 °C. Vanadium is evaporated from an electron gun beam with a deposition rate of 0.1 $\text{Å}\,\text{s}^{-1}$, and an oxygen partial pressure of $6.2 \cdot 10^{-6}$ Torr is used during the growth [Dillemans et al. (2014)]. Under these conditions, a single crystalline film with the c-axis oriented perpendicular to the surface is obtained (sample VO_008, see Appendix A for further details on the sample characterization). A micro bridge, constituted by 40 nm Au/5 nm Ti thick electrodes with 50 μm-width and 2 μm separation, is nanopatterned on the film surface, as shown in Fig. 6.1 (a). Temperature-dependent resistivity measurements (see Fig. 6.1 (b)) are performed using a Keithley Sourcemeter 2634B in the 2-points configuration across the Au/Ti electrodes. The device temperature is controlled by a closed-cycle cryostat equipped with a heater. The temperature sweep rate is set to 0.5 K per minute. When cooled down, the device undergoes the metal-to-insulator transition, characterized by a resistance increase of almost three orders of magnitudes, at $T_{\text{IMT}} \sim 170$ K. In our device, the resistance ranges from 20 Ω at room temperature (metallic state) to 130 kΩ at T = 140 K (insulating state). The heating and cooling branches evidence the typical hysteresis cycle of the IMT, which spans the insulator/metal coexistence region from 155 to 185 K.

6.1.2 Photo-induced resistivity measurements

Resistance measurements are combined with light excitation by focusing a train of infrared pulses (0.4 μJ, 50 fs) at 800 nm wavelength (1.55 eV photon energy) generated by an optical parametric amplifier pumped by a Yb-laser system. A pulse picker allows to control both the repetition rate, set to 25 kHz, and the total number of pulses impinging on the sample. The laser output is focused on the device by a 10 cm lens. The FWHM of the spot size on the device is 50 μm, as measured using the knife-edge

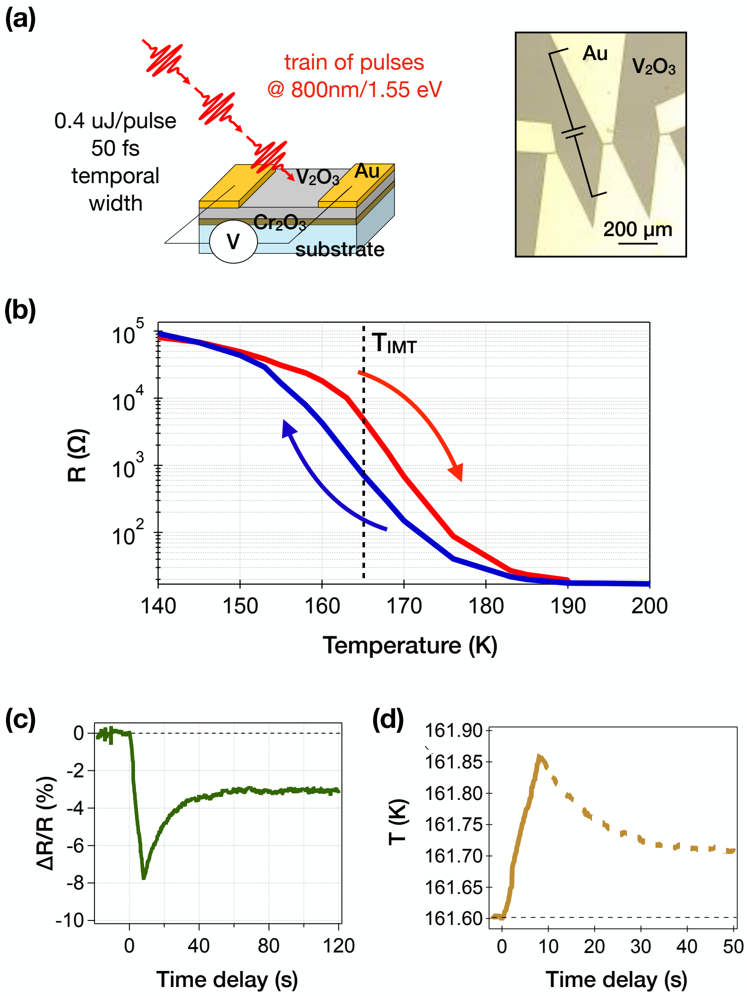

Figure 6.1: **Working principle of the experiment.** **(a)** Left: Cartoon of the experimental set-up. A finite train of laser pulses ($\hbar\omega = 1.55$ eV, 50 fs temporal width, $\nu = 25$ kHz) is used to photoexcite the device. The change in the 2-points resistance of the device is simultaneously measured across the region before, during and after the laser excitation by means of Au/Ti electrodes. The contact resistance can be neglected since is very small ($\sim 5\ \Omega$) with respect to the V_2O_3 bridge resistance ($\sim 15\ \mathrm{k}\Omega$). Right: Microscopic image of the device used during the experiment. **(b)** Equilibrium 2-points resistance hysteresis measured as a function of the temperature. The red (blue) arrows indicate the heating (cooling) branch. **(c)** Relative variation of resistance measured across the device as a function of the time delay. The time zero corresponds to the moment when the first pulse of the laser train arrives. **(d)** Result of the conversion of resistance drop measurements (see panel (c)) into effective local temperature. The resistance vs temperature curve shown in Fig.6.1(b) has been inverted such to obtain for each value of resistance the corresponding value of temperature. The dashed line corresponds to the cooling down branch of the system, which cannot be uniquely associated to an actual local temperature since during the cooling the system doesn't follow any known path.

technique. The pump incident fluence on the device is of the order of 0.2 mJ/cm^2, which is below the threshold necessary to photoinduce the complete insulator-to-metal transition [Ronchi et al. (2019)]. In Fig. 6.1 (c) we show the typical resistance drop measured after excitation with a controlled number of light pulses (200 kpulses at 25 kHz rep. rate). The device is cooled down to 100 K and then heated up to T $\simeq$ 160 K, i.e. in the insulator-metal coexistence region. Before light excitation, the system is thus in a high resistivity state along the heating branch of the hysteresis curve shown in Fig. 6.1 (b). The time-dependent resistance is obtained by measuring the current flowing across the bridge in the voltage source mode configuration ($V = 0.5$ mV). After 8 s, i.e. at the end of the pulse train, the resistance drops by 8 % with respect to the initial value. Once the light excitation is removed, the relative resistance variation starts to decrease, until it reaches a plateau corresponding to a non-volatile change of about 3%. The explanation of this effect resides in the inherent hysteresis of the IMT (see Fig. 6.1 (b)): after the laser-induced warming up, the relaxation process leads the system to a state that is located somewhere on the cooling branch and is therefore characterized by a smaller resistivity. In order to restore the initial resistance value, the device must be subjected to a complete thermal cycle, corresponding to heating up to 300 K, cooling down to 100 K and then heating up to T $\simeq$ 160 K. The same thermal cycle protocol is applied before any of the resistance drop measurements reported in the following.

The resistance-temperature curve shown in Fig.6.1 (b) can be used to retrieve the local effective temperature of the V_2O_3 device during the light excitation process, as shown in Fig. 6.1 (d). The local effective temperature is extracted as follows. The heating branch of the resistance vs temperature curve (Fig. 6.1 (b)) is interpolated and inverted. A twelfth-degree polynomial function is fit to the curve obtained by the inversion procedure. The fit coefficients are used in an automatic routine to convert each point of all the experimental curves in local effective temperature (see Fig. 6.1 (d)). The error associated to the local effective temperature retrieved through the above procedure is then obtained by considering the accuracy of the Keithley Sourcemeter ($\pm$ 0.02 %) in the voltage range applied during the experiments. We stress that the resistance-temperature relation is single-valued only along the heating branch. Therefore, the resistance value can be converted in the actual local temperature only during the heating up process in the 0-8 s time span.

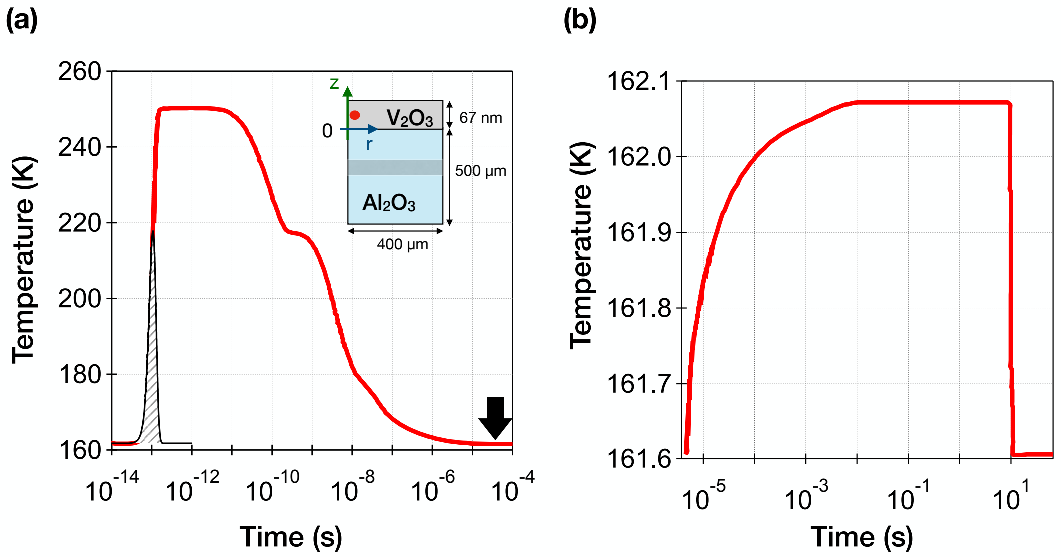

Figure 6.2: **Finite elements method simulations. (a)** The red line represents the temperature increase due to the single pulse excitation (black dashed area) as a function of the time (logarithmic scale). The black arrow indicates the time ($t = 40\ \mu$s) at which the following pulse arrives. Inset: sketch of the geometry used in the Comsol simulations. The red dot indicates the point where the temperature has been evaluated ($z = 33.5$ nm, $r = 50$ nm). **(b)** The steady-state temperature variation of the system induced by $2 \cdot 10^5$ laser pulses is shown. The maximum temperature reached after the excitation with the pulse train is used as input to build the curves reported in Fig. 6.3 (a).

6.1.3 Finite Elements Method simulation of the thermal problem

The heating induced by the laser excitation is numerically simulated by finite-element methods (Comsol Multiphysics). In the simulations, we consider the 67 nm thick V_2O_3 film on top of a 500 μm thick (0001)-Al_2O_3 substrate. The Cr_2O_3 buffer-layer is omitted since its thermal and optical properties are very similar to the sapphire's ones. The problem is solved in 2D axial symmetry in a region with 800 μm diameter. A representation of the sample cross-section is reported in the inset of Fig. 6.2 (a). Insulating boundary conditions are applied on the top and lateral boundaries, whereas the sapphire bottom boundary (z = -500 μm) is kept at the constant temperature $T_0 = 161.6$ K, which corresponds to the actual initial effective temperature of the device, as extracted from the resistance value. The thermal problem is addressed in two different cases: the single- and multi-pulse excitation protocols.

In the former case, a single laser pulse with temporal and spatial gaussian

Parameter	**Value**	**Units**	**Ref.**
$c_p(T)\Big\vert_{V_2O_3}$	$c_p(T)$ (~495 @160 K)	J kg^{-1} K^{-1}	Keer et al. (1976)
$c_p\Big\vert_{Al_2O_3}$	776	J kg^{-1} K^{-1}	Weber (2001)
$\kappa(T)\Big\vert_{V_2O_3}$	$\kappa(T)$ (~3.1 @160 K)	W m^{-1} K^{-1}	Andreev et al. (1978)
$\kappa\Big\vert_{Al_2O_3}$	35	W m^{-1} K^{-1}	Caddeo et al. (2017)
$\rho_{V_2O_3}$	4870	kg m^{-3}	Weber (2001)
$\rho_{Al_2O_3}$	3980	kg m^{-3}	Weber (2001)
$\mathrm{Re}(\tilde{n}_{V_2O_3})$	1.997 @800 nm	kg m^{-3}	Qazilbash et al. (2008)
$\mathrm{Im}(\tilde{n}_{V_2O_3})$	0.382 @800 nm	kg m^{-3}	Qazilbash et al. (2008)
$\mathrm{Re}(\tilde{n}_{Al_2O_3})$	1.76 @800 nm	kg m^{-3}	Malitson (1962)

Table 6.1: Summary of materials parameters values adopted in the present work for FEM simulations.

profiles matching the experimental ones, excites the sample. We consider an energy density delivered to the system (0.66 kJ/cm^3) such that the time and spatial integral matches the total energy released by the laser pulse. The estimated energy absorbed within the 67 nm V_2O_3 film is calculated with a multireflection model (total absorption A= 0.22), assuming the optical constants reported in the literature [Qazilbash et al. (2008)]. Using Fourier's law, the energy balance within the volume of the V_2O_3 film can be written as:

$$-\nabla\cdot\left[-\kappa(T(r,z,t))\nabla T(r,z,t)\right]+P(r,z,t)=\rho\, c_p((r,z,t))\frac{\partial T(r,z,t)}{\partial t} \tag{6.1}$$

where $P(r,z,t)$ is the absorbed pulse power profile, $\kappa(T)$ is the temperature dependent thermal conductivity [Andreev et al. (1978)], ρ the mass density, and $c_p(T)$ the temperature-dependent total specific heat at constant pressure [Keer et al. (1976)]. For sake of completeness, the parameters used in the simulation are reported in Table 6.1. The following heat flux continuity boundary condition is used at the V_2O_3/ Al_2O_3 interface:

$$k_{V_2O_3}\frac{\partial T}{\partial z}\bigg|_{z=0^+}=k_{Al_2O_3}\frac{\partial T}{\partial z}\bigg|_{z=0^-}. \tag{6.2}$$

The initial condition is T_0 = 161.6 K throughout the sample and the substrate. The equations are solved via the finite element method, covering a time scale spanning seven orders of magnitude.

The thermal dynamics of the single pulse excitation is shown in Fig. 6.2 (a). We remark that we are interested in thermal dynamics on timescales longer than the pulse duration and electron-phonon coupling. Therefore, we will assume the complete thermalization between the electron and lattice subsystems, as implied by the use of the total specific heat and thermal conductivity values. After the impulsive energy absorption, the temperature reaches its maximum value ($\sim$ 250 K) within few picoseconds. The cooling down process, mainly driven by the energy diffusion through the sapphire substrate, starts approximately $\sim$ 10 ps after the excitation. If we consider the time needed to reduce the initial temperature variation by a factor 2, we obtain a half-life of about 2 ns. The cooling down to the initial temperature T_0 = 161.6 K is almost completed within $\sim$ 40 μs, although a small temperature increase of $\sim$ 0.04 K persists.

In the multi-pulse excitation protocol, the heating associated to each pulse accumulates on top of the temperature increase triggered by the previous ones. Considering a pulse distance of 40 μs (25 kHz rep. rate), the small temperature difference accumulated after each pulse leads to a steady-state increase of the local effective temperature, which ultimately drives the resistance drop across the bridge observed after the light excitation. For simplicity, the effect of thermal heating induced by the multi-pulse excitation is simulated by considering a continuous laser beam in which the average power is the same of the pulse train. An example of the temperature dynamics, for a train of $2 \cdot 10^5$ pulses, is shown in Fig. 6.2 (b). The heat accumulation leads to a steady-state temperature increase up to value close to 162.1 K. Once the input power is removed, the system rapidly cools down to the initial temperature.

6.2 Results and discussion

The comparison between the experimental results and the numerical simulations is shown in Fig. 6.3 (a). The applied voltage for the resistance measurements is V = 0.5 mV, i.e. much smaller than the threshold $V_{th} \simeq$2.5 eV necessary to obtain the resistive switching. The experimental points (green circles) represent the maximum effective temperature increase, estimated by the volatile resistance drop as described in Sec 6.1.2, as a function of the number of excitation pulses. We stress that each experimental point is obtained after a complete thermal cycle, necessary to restore the initial resistance of the device (see Sec. 6.1.1). The data show that no significant temperature increase is detectable below $\sim 10^4$ pulses. Above this threshold the temperature grows and saturates after approximately 10^6 pulses. The temperature achieved in the saturation regime, i.e. when the excitation average power perfectly matches the thermal losses towards the substrate, is $\sim$ 162.06 K. The dynamics of the temperature $T(t)$ can be rationalized in terms of a simple differential equation:

$$C_T \frac{d(T - T_0)}{dt} = P - \frac{1}{R_{th}}(T - T_0) \tag{6.3}$$

where C_T is the total heat capacity, P is the external power and R_{th} is the thermal resistance, which is inversely proportional to the substrate thermal conductivity. The solution of this equation is the exponential function: $T(t) = T_0 + \delta T_\infty(1 - e^{-t/\tau})$, where $\tau = R_{th}C_T$ and $\delta T_\infty = R_{th}P$. The red solid line in Fig. 6.3 (a) represents the exponential fit, which allows extracting a time constant $\tau = 18.5 \pm 0.8$ s corresponding to $(4.6 \pm 0.2)\times 10^5$ pulses.

The local effective temperature retrieved by the resistance drop is compared to the results of calculations of the full thermal problem, as described in Sec. 6.1.3. The black solid line in Fig. 6.3 (a) represents the temperature increase corresponding to the steady state heating obtained by finite-element calculations, when an average power corresponding to that of the pulse train exciting the device is considered. The calculated temperature increase also accounts for the time constant of the electrical circuit used for the resistance measurements, which would wash out resistance drops faster than $\sim$100 ms. The calculated steady-state temperature increase, i.e. δT_∞=0.5 K perfectly matches the experimental value. Considering that δT_∞ depends only on the dissipated power P and on the thermal resistance, we can conclude that the finite element calculations perfectly account for the heat dissipation within the V_2O_3 film and through the substrate. The difference between the calculated and measured time constants of the exponential heating dynamics can be instead attributed to an underestimation of the total heat capacity C_T. Throughout the calculations of the thermal problem, we assumed perfect electron-phonon thermalization and we have thus considered the V_2O_3 temperature-dependent total specific heat [Keer et al. (1976)]. Nonetheless, the absorption of each single light pulse is mediated by the electronic population which undergoes a large temperature increase. The effective electronic temperature dynamically overcomes the Mott insulator-to-metal transition temperature T_{IMT}, which is accompanied by a divergence

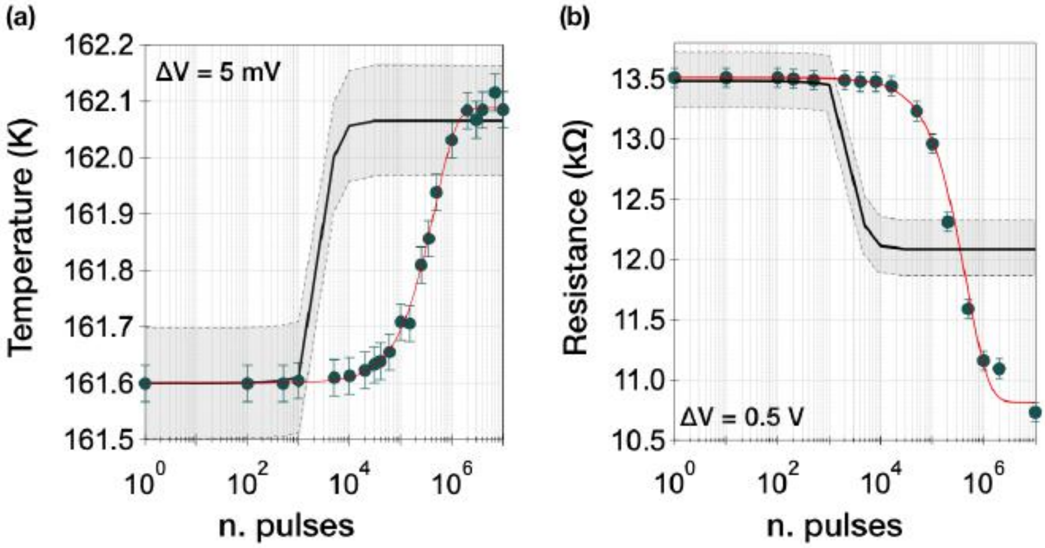

Figure 6.3: **Comparison between experimental and numerical results.** **(a)** Maximum variation of the sample's temperature induced by the laser pulses as a function of the total amount of pulses (green circles). The applied voltage is V =0.5 mV. The solid black line represents the simulated data where the maximum temperature has been extracted for each finite number of pulses. The grey area shows the error interval associated to the model assumptions and numerical approximations. The red solid line represents the exponential fit to the experimental data. **(b)** Maximum laser-induced drop of the device resistance when a constant voltage bias $V = 0.5$ V is applied across the Au/Ti electrodes (green circles). The solid black line represents the outcome of numerical simulation, from which the expected resistance drop is retrieved from the local effective heating for each finite number of pulses. The dissipated power related to the Joule heating has been added to the power dissipated by the laser excitation. The grey area shows the error interval associated to the model assumptions and numerical approximations. The solid red line represents the exponential fit to the experimental data.

of the electronic effective mass m^*. Considering that the electronic specific heat of an electron gas $c_{el} \propto m^{*3/2}$, the dynamical crossing of $\mathrm{T_{IMT}}$ is naturally accompanied by a large increase of c_{el}. In the vicinity of the Mott transition, the electron gas thus behaves like a reservoir capable of absorbing a large quantity of energy but limiting the impulsive increase of the effective temperature of the electron-phonon system. Our results are compatible with $c_{el} = (30 \pm 6) \times c_p(T_{IMT})\big|_{V_2O_3}$, which suggests an effective mass increase of 10, perfectly compatible with what recently observed in VO_2 [Lee et al. (2017)].

Once assessed the validity of the thermal model to evaluate the laser-induced heating in the saturation regime, we can compare the expected thermally induced resistance drop to what is actually measured when the laser pulses are combined to the application of a voltage that is no longer negligible with respect to V_{th}. In Fig. 6.3 (b) we report the resistance drop, measured following the procedure previously described, with $V = 0.5$ V applied voltage. In this case, although the resistance drop is described by an exponential function (solid red line) with the same time constant (τ=18.7 ± 1.6 s), the value achieved in the saturation regime ($\delta \mathrm{R}_\infty \simeq$2.6 k$\Omega$) is twice the value measured ($\delta \mathrm{R}_\infty \simeq$1.3 k$\Omega$) for $V = 5$ mV.

The measured resistance drop measured at $V = 0.5$ V is compared to the value expected by considering the laser-induced heating (the parameters of the thermal calculations are the same than the previous low-voltage case) and including the effect of Joule heating induced by the current flowing throughout the V_2O_3 bridge. The additional dissipated power can be written as

$$\Delta P_J(T) = \frac{\Delta V^2}{R_{V_2O_3}(T)} \tag{6.4}$$

which is added to the total power source $P(r, z)$ provided by the pulse train. The black solid line in Fig. 6.3 (b) represents the result of the numerical simulation converted in the expected resistance drop by means of the resistance vs temperature calibration curve (see Fig. 6.1 (b)). We note that the Joule heating induced by the current, $\Delta P_J(T)$=2×10^{-5} W is negligible as compared to the laser power, which amounts to $\sim 10^{-2}$ W. As a conclusion, the additional Joule heating does not account for the measured resistance drop in the stationary regime, which is twice that expected for heating alone. We also stress that the voltage applied through the device is smaller than the threshold value necessary for the resistive switching. Therefore, in this regime no metallic filaments [Kalcheim et al. (2020)], possibly responsible for large local Joule heating, are created and the system can be treated as homogeneous.

6.3 Conclusion

In conclusion, we investigated the simultaneous action of a train of infrared light pulses and an external voltage on a Mottronic device based on V_2O_3, which undergoes an IMT at $\mathrm{T_{IMT}} \simeq$170 K. When the device is in the insulator-metal coexisting region (T = 160 K) and a 0.5 V voltage is applied, the measured resistance drop induced by a pulse number exceeding 10^6 is twice than the value expected from the simple local heating of the device. Our results suggest that although the 0.5 V voltage is below the threshold (V_{th}=2.5 V) necessary for inducing the complete and irreversible resistive switching, it brings the insulating phase close to the insulator-to-metal instability. The simultaneous excitation with a sufficient number of infrared pulses thus triggers a further weakening of the insulating state along a non-thermal pathway. This process can be rationalized on the basis of recent theoretical results [Mazza et al. (2016)], which showed that in the insulator-metal coexistence region, the application of an electric field alone is able to induce the non-thermal weakening of the Mott insulating phase via the formation of new metallic states at the Fermi level with no counterpart at equilibrium. This mechanism is in sharp contrast with the conventional Zener tunneling mechanism that is usually invoked to describe the resistive switching dynamics. Interestingly, the state variable that characterizes the transition is the orbital polarization, defined as p = $n_{e_g^\pi}$-$n_{a_{1g}}$, where $n_{e_g^\pi}$ is the occupation of the lowest energy V-3d e_g^π orbitals and $n_{a_{1g}}$ is the occupation of the V-3d a_{1g} orbitals. The Mott insulating phase is characterized by p = 2, whereas the application of an electric field induces the formation of a metallic state with p = 1.2-1.6. As recently shown [Ronchi et al. (2019)], the excitation with infrared light pulses with 1.55 eV photon energy can induce an orbital polarization decrease of the order of $\delta p \simeq$-10^{-3}-10^{-2}, thus favouring the weakening of the insulating phase and the growth of already existing metallic domains. In conclusion, the combination of a below-threshold voltage and the excitation with infrared light pulses capable of modifying the occupation of vanadium orbitals favours the metallicity of the system well beyond what can be ascribed to thermal effects. The present results call for the development of time-resolved microscopy techniques to investigate the real-time dynamics of the metallicity in Mottronics and resistive switching devices subject to the simultaneous application of electric fields and light pulses.

Chapter 7

Conclusion and outlook

In conclusion, the aim of this thesis work was to combine voltage bias with laser excitation to investigate the possibility of obtaining an ultrafast and reversible non-thermal switching in a V_2O_3-based microdevice. The proposed experiment was very complex and required preliminary preparation to study some key ingredients that at the beginning of the project were still missing.

First of all, it was necessary to address the role of the spatial inhomogenities across the IMT in controlling the temporal dynamics of the transition itself. In particular, many efforts were focused on investigating the supposed homogeneous low-temperature insulating phase. In Chapters 3 and 4 we uncovered the intrinsic nanotexture of the monoclinic AFI phase of V_2O_3 and its relation with the multistep nature of the IMT dynamics at short time scales. Exploiting the sensitivity of resonant X-ray PEEM to the orientation of the V 3d orbitals, we unveiled a spontaneous self-organization of the Mott insulating phase, characterized by striped monoclinic domains with different orientations. This AFI nanotexture appears to be an intrinsic property of the insulating phase, independent of the film's thickness or the characteristics of the substrate, as predicted from the theory of the martensitic transitions. The results also show that the insulating domain boundaries host the birth of metallic seeds, whose expansion can be triggered by the impulsive photoinduced change of the orbital population. The timescale of the growth process (25-30 ps) corresponds to the propagation at the sound velocity across the transverse dimension of the insulating stripes. Our results show that this nanotexture strongly affects the nucleation and growth dynamics of metallic grains. The data point toward a non-thermal scenario, in which the expanding metallic grains transiently retain the in-plane distortion of the vanadium hexagons typical of the AFI phase.

As second step, we addressed the nature of this photoinduced transient metallic state by performing for the first time tr-PEEM on a V_2O_3 thin film (see Chapter 5). The experiment demonstrated the possibility of driving an electronic, metastable switching of a non-thermal metal-like state. We demonstrated that after the pump-induced excitation the in-plane monoclinic nanotexture is retained although the laser fluence is above the threshold to optically drive the system in a complete metallic state. Numerical simulations suggested that this particular condition is favoured by the presence of the domains boundaries in the monoclinic nanotexture itself. Therefore, the monoclinic nanotexture has a key role in the stabilization of the monoclinic metal. This intriguing result suggests the possibility to partially decouple the SPT from the IMT. This decoupling would pave the way to greatly improve the transition speed performance in Mottronics, with great benefit in nextgen applications, one example among all neuromorphic networks.

Building on these results, we then tackled the final goal of this work. In Chapter 6, we investigated the simultaneous action of a train of infrared light pulses and an external voltage on a V_2O_3-based device. We showed that, when the device is in the insulator-metal coexisting region and a voltage smaller than that necessary to achieve the resistive switching is combined with a sufficient long train of pulses, the measured resistance drop is twice than the one expected from the simple local heating of the device. Our results suggest that the below-threshold voltage brings the insulating phase close to the insulator-to-metal instability. In this condition, the excitation with infrared light pulses capable of modifying the occupation of vanadium orbitals favours the metallicity of the system well beyond what can be ascribed to thermal effects. The multi-excitation protocol presented in this work suggests the possibility to induce a non-thermal ultrafast IMT by combining electric field and photoexcitation in a Mottronic device. In addition, the dynamical processes unveiled by our work also impact the modeling of the electrical breakdown in Mott insulators. Our results suggest that each node in the resistor network corresponds to an insulating nanodomain with a well-defined orientation of the monoclinic distortion. The light excitation can trigger, on the picosecond timescale, the ultrafast switching of isolated monoclinic domains from the insulating to a non-thermal metallic state which retains the monoclinic lattice structure. This new intriguing result opens to the possibility of controlling the electronic and magnetic switching of Mott insulators at THz frequencies by suitably engineering the geometry of the nanotextured insulating domains in thin films, with impact on the development of novel Mottronics devices.

More in general the results reported in this thesis work has an impact on the understanding of the physics that governs the MIT and SPT in V_2O_3. In particular, the combination of nano-imaging (PEEM), time-resolved spectroscopy and electrical measurements allowed us to disentangle the importance of the different DOF and to observe fundamental aspects of the IMT never caught before. The results shown are not relevant only for the V_2O_3 case, but also be promptly extended to many d- or f-shell Mott insulators, pushing forward the understanding of all these exotic materials for the application in future technologies. Besides, the work presented in this thesis lays the foundation for new research perspectives. For example, to better clarify the role of the monoclinic nanotexture in controlling the resistive switching dynamics it would be interesting to carry out a PEEM experiment before and after the application of a voltage bigger enough to induce the RS. The observation of the presence or absence of the monoclinic nanotexture after the RS switching, could establish once and for all whether this transition is of electronic or thermal origin. This dynamics could then be studied from a temporal point of view by providing an optical pump-probe experiment while a voltage below or above the threshold is applied between the electrodes of the device. Both of these experiments could provide valuable details on the spatial and temporal dynamics of the resistive switching and have a profound impact on the development of new strategies in the control and manipulation of Mottronic devices for technological applications.

Appendices

Appendix A

Thin films growth details and sample list

The sample list used for this thesis work is itemized in Table A.1. All the V_2O_3 thin films were deposited by oxygen assisted Molecular Beam Epitaxy (MBE) in a vacuum chamber with a base pressure of 10^{-9} Torr. A (0001)-Al_2O_3 substrate is used without prior cleaning and is slowly heated to the growth temperature of 700 C, as measured with a thermocouple. V is evaporated from an e-gun with a deposition rate of 0.1 Å/s with an oxygen partial pressure of 6.2×10^{-6} Torr. Under these conditions, a single crystal epitaxially grown thin film with the c-axis perpendicular to the surface plane is obtained [Homm Jara (2019)]. X-ray Diffraction (XRD) and X-ray Reflectivity (XRR) measurements have been performed on all the samples to characterize their structural quality. For instance for the 40 nm V_2O_3 film epitaxially grown on (0001)-Al_2O_3, X-ray diffraction measurements were performed on a Panalytical X'pert Pro diffractometer using monochromatic $K_{\alpha 1}$ radiation of a Cu anode. A film thickness of 40 nm and a surface roughness below 1 nm were determined from XRR measurements and the simulation of the data with the X'pert Reflectivity software. The XRR measurement and simulated curve are shown in Fig. A.1 (a). The θ-2θ scan in Fig. A.1 (b) shows the symmetric peak (0006) of the film and substrate, with the c-axis oriented perpendicular to the surface. The finite-size oscillations (Pendellösung fringes) around the film peak maximum confirm the high quality epitaxial deposition with a smooth surface and interface. Finally, to extract the lattice parameters (a and c) of the film, RSM around the asymmetric peak (1 0 -1 10) of the film and

Name	**Layer**	**Film**	**Buffer**	**Size** [mm^2]	**T**(K)	**Experiment**
VB6-B	single	40 nm V_2O_3	/	10×10	145	PEEM, UOS
VO_010	single	51 nm V_2O_3	/	10×10	135	tr-PEEM, UOS
VO_008	bilayer	67 nm V_2O_3	37 nm Cr_2O_3	7×7	165	PEEM, RS+UOS

Table A.1: List of the V_2O_3 samples measured in PEEM and Ultrafast Optical Spectroscopy (Ultrafast Optical Spectroscopy (UOS)) experiments.

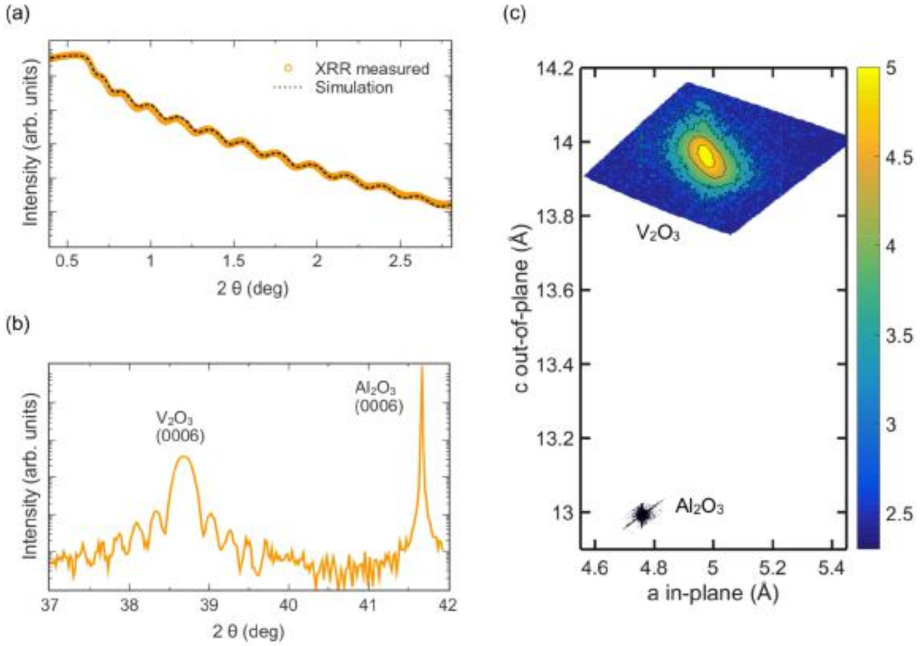

Figure A.1: (a) XRR measurement and simulated curve to extract the film thickness and surface roughness. XRD θ-2θ scans around the (0006) reflections of the 40 nm V_2O_3 film and Al_2O_3 substrate. (c) Reciprocal Space Map (RSM) transformed to in-plane and out-of-plane lattice spacings of the film and the substrate. Adapted from [Ronchi et al. (2019).]

the substrate were performed. The resulting RSM transformed to in-plane (a-axis) and out-of-plane (c-axis) lattice spacings is shown in Fig. A.1 (c). The lattice parameters extracted from the peak maximum are a = 4.977 Å and c = 13.962 Å and correspond well with the bulk V_2O_3 values of a = 4.954 Å and c = 14.008 Å, thus confirming the single crystalline nature of the film. The estimated error on the lattice parameters is ± 0.003 Å. The small tensile (compressive) in-plane (out-of-plane) strain of 0.46% (-0.33%) is thermal in nature [Dillemans et al. (2014)]. A similar protocol has been used to characterize the growth quality of all the V_2O_3 or V_2O_3/Cr_2O_3 thin films measured in this thesis.

Appendix B

PEEM images analysis

B.1 Evaluation of the metallic filling fraction $\mathrm{F_M}$

The analysis of the XLD-PEEM images has been performed by means of the image processing package Fiji [Schindelin et al. (2012); Rueden et al. (2017)]. Whitin this package, the Weka Trainable Segmentation [Arganda-Carreras et al. (2017)] machine learning algorithms have been applied to the images to produce pixel-based segmentations, and consequently, to identify different XLD contrast regions. Once the metallic areas inside a single domain have been highlighted, we calculate the percentage of metallicity by counting the number of recognized pixel with respect to the total pixels number in a fixed domain. A weighted average is evaluated with respect to the size of several domains to give more accurate results [Ronchi et al. (2019)].

B.2 PEEM resolution

The structures observed in XLD-PEEM images are the result of a convolution between the real size of the spatial domains and the experimental resolution ($\sim$ 30 nm). The finite resolution prevents the identification of insulating areas with dimension less than 30 nm, thus leading to an over-estimation of the real metallic filling fraction $\mathrm{F_M}$ determined via the clustering process of the pixel-based segmentation routine [Schindelin et al. (2012); Rueden et al. (2017); Arganda-Carreras et al. (2017)]. In order to quantify this over-estimation, we simulated the effect of the experimental resolution by

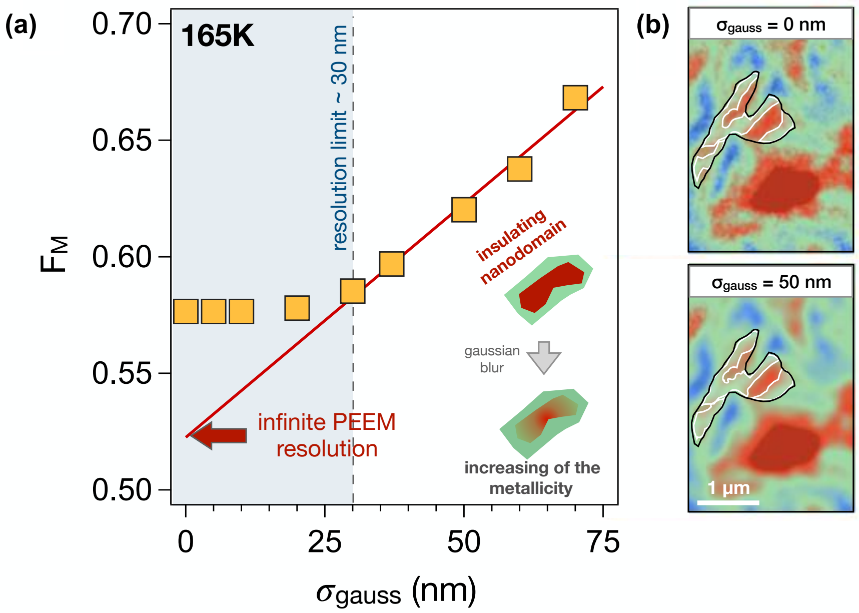

Figure B.1: **Estimated error calculation on the metallic fillling fraction F_M.** (a) Estimated metallic filling fraction F_M (yellow markers) as a function of radius of the gaussian blurring of the XLD-PEEM images. Above the instrumental resolution limit ($\sim$ 30 nm) a linear increase of the estimated F_M is observed. The linear fit (red line) allows us to extrapolate the real F_M that would be observed by an infinite resolution experiment. The difference between the extrapolated and the calculated metallic fraction can be considered as the uncertainty of the points of heating branch of the hysteresis cycle shown in Fig. 3.4. (b) Top: XLD-PEEM images taken at 165 K. The metallic regions are highlighted by the white contours. Bottom: image blurred with $\sigma_{gauss} = 50$ nm. After the pixel-based segmentation, the metallic area (white shadows) increases by about 4%. Adapted from [Ronchi et al. (2019).]

performing a gaussian blurring in the same region of interest of Fig. 3.4. The plot in Fig. B.1 reports the estimated F_M as a function of the radius (σ_{gauss}) of the gaussian blurring. A linear fit has been used to extrapolate the value of F_M in the $\sigma_{gauss} \longrightarrow 0$ limit (ideal case) and therefore the uncertainty in the metallic filling fraction F_M, which amounts for instance to $\sim$ 10% at 165K [Ronchi et al. (2019)].

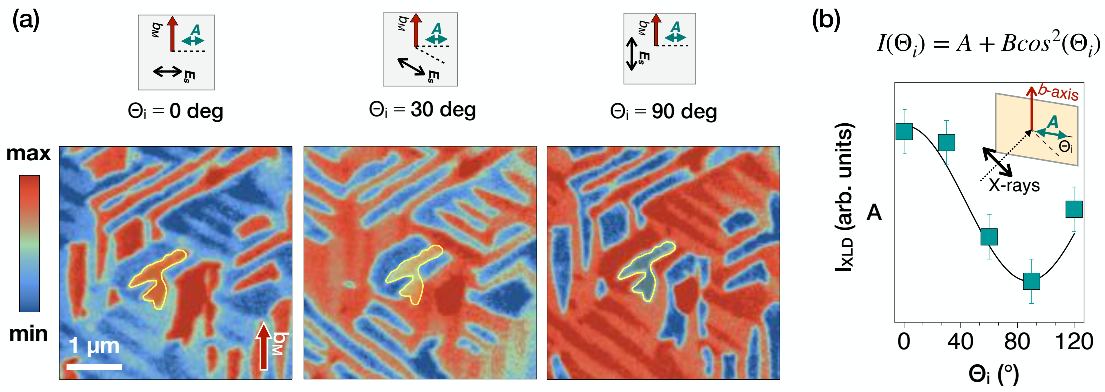

Figure B.2: **Study of the domains orientation at 120** K. (a) XLD-PEEM images at different angles between the in-plane electric field polarization $\mathbf{E_S}$ of the X-rays and the antiferromagnetic A-axis, perpendicular to the crystallographic b-axis of the V_2O_3 film. The yellow line highlights the domain which has been analized in panel (b). (b) I_{XLD} as a function of the angle Θ_i between the A-axis (green arrow) and the X-ray polarization direction (double-headed black red arrow). The insets shows a sketch of the experimental configuration.

B.3 Study of the AFI monoclinic domain orientation

The XLD contrast of the insulating domains depends on the relative angle between the direction of the linear horizontal light $\mathbf{E_S}$ polarization and the antiferromagnetic **A** axis within each domain. In Fig. B.2(a) we report different PEEM images of the same sample area acquired by rotating the V_2O_3 film around the c-axis, i.e. at different angles (Θ_i) between the in-plane light polarization and the **A**-axis. While the morphology of the domains does not change, the XLD signal (I_{XLD}) scales as:

$$I_{XLD} = A + B \cdot \cos^2 \Theta_i \tag{B.1}$$

as expected for magnetic linear dichroism signals [Lüning et al. (2003)]. In Fig. B.2(b), we report the angle-dependence of $I_{XLD}(\Theta_i)$ of the monoclinic domain highlighted by the yellow line.

Appendix C

Reflectivity variation and Bruggeman Effective Medium Approximation

The Bruggeman effective medium approximation has been widely used (see e.g. Refs. Lupi et al. (2010), Jepsen et al. (2006), and Stewart et al. (2012)) to describe the effective optical properties of vanadium oxides across the percolative IMT. The model relates the effective macroscopic dielectric function (ϵ_{eff}) of an inhomogeneous system, constituted by a mixture of metallic and insulating regions, to the dielectric functions of the metallic (ϵ_{M}) and insulating (ϵ_{I}) bulk species:

$$\begin{aligned} \epsilon_{eff} = \frac{1}{4}\{\epsilon_I(2-3F_M)+\epsilon_M(3F_M-1)+ \\ +\sqrt{[\epsilon_I(2-3F_M)+\epsilon_M(3F_M-1)]^2+8\epsilon_I\epsilon_M}\} \end{aligned} \tag{C.1}$$

where $\mathrm{F_M}$ is the metallic filling fraction as defined in the main text. The procedure adopted for calculating the effective optical properties is the following:

1. ϵ_{M} is extracted from the experimental high-temperature temperature (T = 200 K) reflectivity (see the inset of Fig. C.1(a) by means of a multi-reflection model, which accounts for the thin $\mathrm{V_2O_3}$ film and the

substrate. The input dielectric function, which perfectly reproduces the measured reflectivity in the 1.4-2.2 eV energy range ($\mathrm{R_M}(\omega)$), is given by a Drude-Lorentz Model (DLM). The oscillators parameters of the DLM have been taken from Ref. Rueden et al. (2017);

2. the experimental reflectivity change between the metallic and insulating phases (shown in Fig. 4.3 of the main text) in the spectral region 1.4-2.2 eV is reproduced by modifying the central frequency of the Lorentz oscillator centered at 2 eV (e_g^π LHB→UHB transition). As output, we obtain ϵ_I, which reproduces $R_M(\omega) - R_I(\omega)$, where $R_I(\omega)$ is the thin film reflectivity at T = 120 K;

3. the effective dielectric function, $\epsilon_{eff}(F_M, \omega)$, is calculated by means of Eq. C.1 for the $\mathrm{F_M}$ values extracted from the PEEM images (Fig. 4.5);

4. the non-equilibrium variation of the effective dielectric function is calculated as $\delta\epsilon_{eff}(F_M, \omega) = \epsilon_{eff}(F_M + \delta F_M, \omega) - \epsilon_{eff}(F_M, \omega)$;

5. the relative reflectivity variation is calculated as

$$\frac{\delta R}{R}(F_M, \omega) = \left[R(F_M + \delta F_M, \omega) - R(F_M, \omega)\right]/R(F_M, \omega) \qquad \text{(C.2)}$$

   using the multi-reflection model and $\epsilon_{eff}(F_M, \omega)$ as an input.

By using the above procedure, we numerically demonstrate the possibility of linearizing both $\delta\epsilon_{eff}(F_M, \omega)$ and $\frac{\delta R}{R}(F_M, \omega)$. In Fig. C.1(a) we plot the real and imaginary parts of the calculated $\delta\epsilon_{eff}(F_M, \omega)$ for $\mathrm{F_M}$ =0.5 and $\delta F_\mathrm{M} =$ 0.1. The $\delta\epsilon_{eff}(F_M, \omega)$ function perfectly overlaps to $\left[\epsilon_M(\omega) - \epsilon_I(\omega)\right]\delta F_M$. Similar results are obtained for any value of $\mathrm{F_M}$. In Fig. C.1(b) we numerically demonstrate the relation $\Phi(F_M, \omega) \simeq \left[R_M(\omega) - R_I(\omega)/R_I(\omega)\right]$, which is used in this work to extract the transient filling factor variation from the relative reflectivity variation. The function $\Phi(F_M, \omega)$ is calculated as:

$$\Phi(F_M, \omega) = \frac{\delta R}{R}(F_M, \omega)\frac{1}{\delta F_M} \qquad \text{(C.3)}$$

for $\mathrm{F_M}$ ranging from 0.01 to 0.93. $\Phi(F_M, \omega)$ is almost independent of the

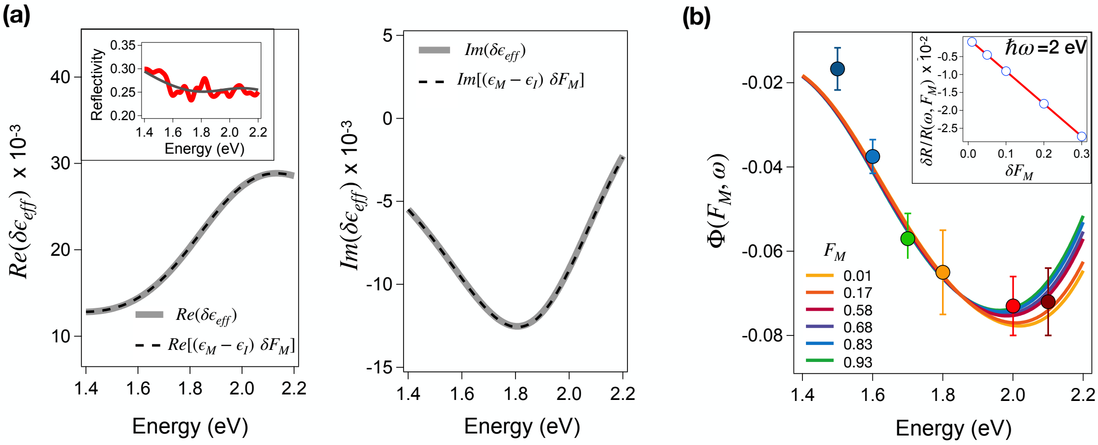

Figure C.1: **Effective dieletric function model.** (a) Frequency dependence of the real and imaginary part of the out-equilibrium effective dielectric function $\delta\epsilon_{eff}(F_M, \omega)$ calculated by means of the Bruggeman model (gray line) for $\mathrm{F_M} = 0.5$ and $\delta F_\mathrm{M} = 0.1$. The black dashed line represents the approximation $\delta\epsilon_{eff} \simeq (\epsilon_M - \epsilon_I)\delta F_M$. These two curves differ by less than 0.2% at 2 eV photon energy. Inset: high-temperature (T = 200 K) reflectivity as a function of the photon energy (red line) and Drude-Lorentz reflectivity model for a 40 nm V_2O_3 film (black line) on a Al_2O_3 substrate. (b) $\Phi(F_M, \omega) \simeq [R_M(F_M, \omega) - R_I(F_M, \omega)/R_I(F_M, \omega)]$ plotted for different values of $\mathrm{F_M}$, corresponding to the metallic filling fractions at the temperature reported in Fig. 4.3. The function $\Phi(F_M, \omega)$ is almost independent of $\mathrm{F_M}$ and differs by less than 5% in the energy range 1.8-2.2 eV and for $0.01 < F_M < 0.93$. The colored dots represent the equilibrium reflectivity change, $[R_M(\omega) - R_I(\omega)/R_I(\omega)]$, as shown in Fig. 4. Inset: Linear relation between $\delta R/R(\hbar\omega = 2\ \mathrm{eV})$ for $\mathrm{F_M} = 0.01$ (dots) and δF_M . The red thin line is the linear fit to the data. Adapted from [Ronchi et al. (2019)].

initial value of $\mathrm{F_M}$ and, within the error bars, is equal to the experimental $[R_M(\omega) - R_I(\omega)/R_I(\omega)]$ function, where $R_I(\omega)$ is the reflectivity at T = 120 K. In the inset of Fig. C.1(b) we also plot the calculated $\frac{\delta R}{R}(\hbar\omega = 2\ \mathrm{eV})$ as a function of δF_M , thus proving the linear relation between the pump-induced reflectivity variation in the visible range and the filling fraction variation.

Finally, in order to demonstrate that the linearization $\delta R(F_M, \omega)/R = \Phi(F_M, \omega) \cdot \delta F_\mathrm{M}$ holds in the entire fluence range spanned by our experiment (see the fluence-dependent data in Fig. 5c), we calculated $\delta R(F_M, \omega)/R$ at the filling factor corresponding to T = 145 K, i.e. $\mathrm{F_M} \simeq 0.01$, for δF_M extending up to 30%. The estimated reflectivity variation is linearly proportional to δF_M for the values accessed by the experiment, as shown in the inset of C.1(b). Similar results are obtained at any value of $\mathrm{F_M}$.

Appendix D

Sample holder drawings for electrical and optical measurements

Carrying out the optical measurements combined with electric bias required the development of a specific sample holder. In fact, such measurements had never been performed in the ILAMP laboratories of the UCSC in Brescia. The conception, development of CAD drawings, and functional tests took nearly two and a half years. In particular, the long period has been used to solve numerous technical issues regarding the practicality of use, the technical feasibility, the choice of the optimal materials given the use in high-vacuum and at cryogenic temperatures. For this reason, the support of a Milan company Cinquepascal srl was requested. The mentioned company also dealt with production. The final result of the sample holder built is shown in Fig. D.1. The main feature of this sample holder is the possibility to remove the mask, upon which the sample is glued, without having to remove all the fixed L-shaped support. Everything is easily done by unscrewing 4 screws. The materials chosen were copper for the thermally conductive parts, fiberglass for the insulating parts, and gold for the pogo pin connectors.

After an initial phase of tests, it was realized that the masks made were not optimal for wire-bonding the samples. We, therefore, had a brainstorming with the electric facility at the Department of Physics and Astronomy at KUL. We adapted the mask as shown in Fig. D.2. We thank the collaboration of Valentijn Tuts for taking the time to make this change.

The experimental setup for electric transport and optical pump-probe measurements has been fully operational since September 2019.

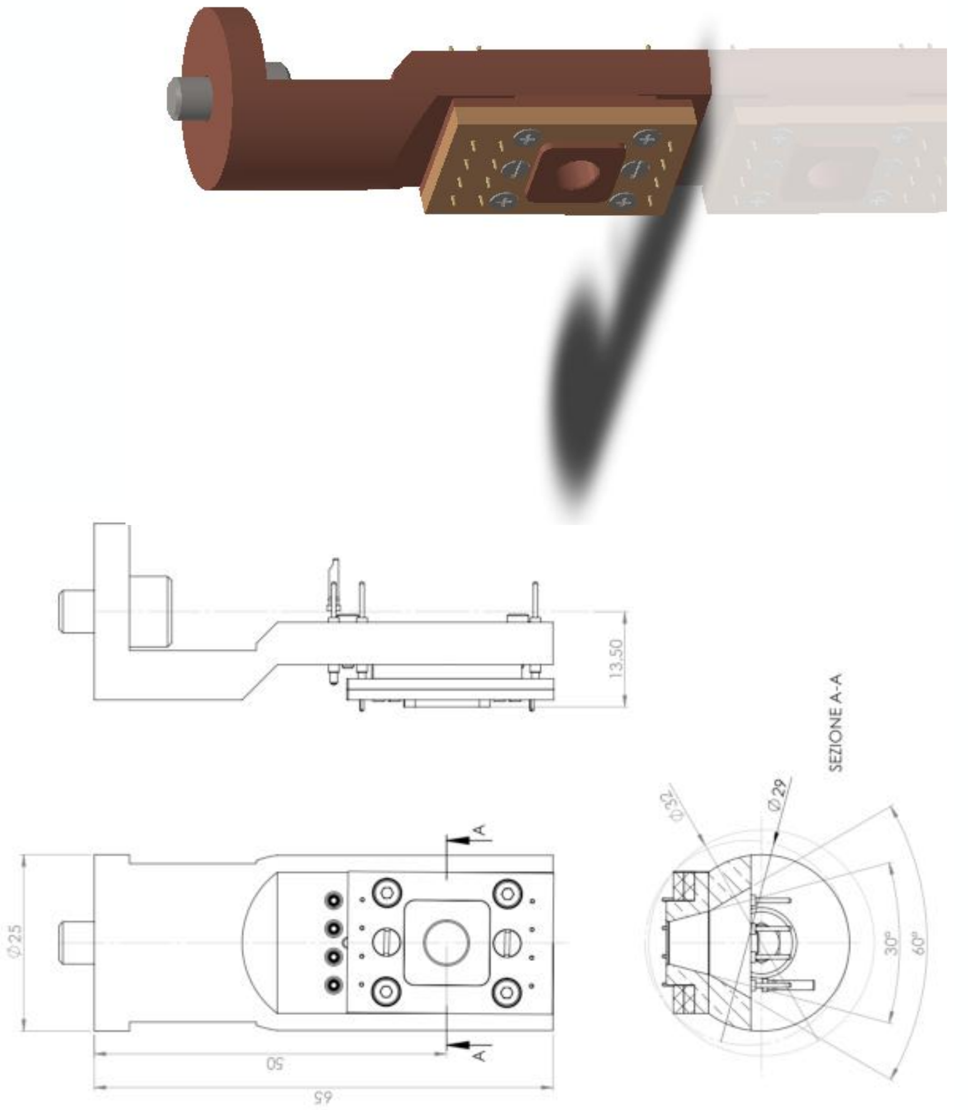
13.50
SEZIONE A-A
Ø32
Ø29
A
A
Ø25
30°
60°
50
65

Figure D.1: Drawing of the sample holder made for electrical measurements at UCSC in Brescia.

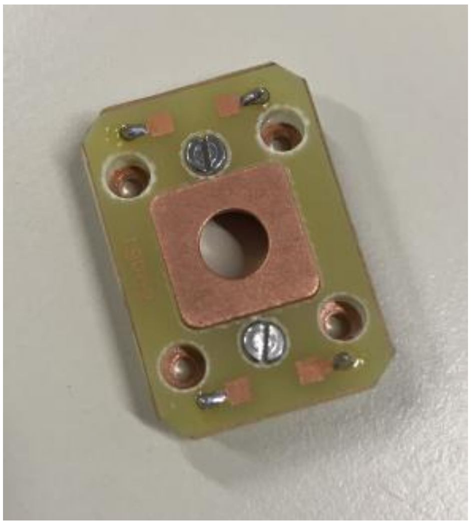

Figure D.2: Upgrade of the mask for wire-bonding made at KUL.

Bibliography

Abreu, E., Gilbert Corder, S. N., Yun, S. J., Wang, S., Ramírez, J. G., West, K., Zhang, J., Kittiwatanakul, S., Schuller, I. K., Lu, J., Wolf, S. A., Kim, H.-T., Liu, M., and Averitt, R. D. (2017). Ultrafast electron-lattice coupling dynamics in VO_2 and V_2O_3 thin films. *Phys. Rev. B*, 96:094309.

Abreu, E., Wang, S., Ramírez, J. G., Liu, M., Zhang, J., Geng, K., Schuller, I. K., and Averitt, R. D. (2015). Dynamic conductivity scaling in photoexcited V_2O_3 thin films. *Phys. Rev. B*, 92:085130.

Andreev, V. N., Chudnovskii, F. A., Petrov, A. V., and Terukov, E. I. (1978). Thermal conductivity of VO_2, V_3O_5, and V_2O_3. *physica status solidi (a)*, 48(2):K153–K156.

Anisimov, V. I., Kondakov, D. E., Kozhevnikov, A. V., Nekrasov, I. A., Pchelkina, Z. V., Allen, J. W., Mo, S.-K., Kim, H.-D., Metcalf, P., Suga, S., Sekiyama, A., Keller, G., Leonov, I., Ren, X., and Vollhardt, D. (2005). Full orbital calculation scheme for materials with strongly correlated electrons. *Phys. Rev. B*, 71:125119.

Arcangeletti, E., Baldassarre, L., Di Castro, D., Lupi, S., Malavasi, L., Marini, C., Perucchi, A., and Postorino, P. (2007). Evidence of a pressure-induced metallization process in monoclinic VO_2. *Phys. Rev. Lett.*, 98:196406.

Arganda-Carreras, I., Kaynig, V., Rueden, C., Eliceiri, K. W., Schindelin, J., Cardona, A., and Sebastian Seung, H. (2017). Trainable Weka Segmentation: a machine learning tool for microscopy pixel classification. *Bioinformatics*, 33(15):2424–2426.

Avrami, M. (1939). Kinetics of phase change. i general theory. *The Journal of Chemical Physics*, 7(12):1103–1112.

Avrami, M. (1940). Kinetics of phase change. ii transformation-time relations for random distribution of nuclei. *The Journal of Chemical Physics*, 8(2):212–224.

Avrami, M. (1941). Granulation, phase change, and microstructure kinetics of phase change. iii. *The Journal of Chemical Physics*, 9(2):177–184.

Banfi, F., Pressacco, F., Revaz, B., Giannetti, C., Nardi, D., Ferrini, G., and Parmigiani, F. (2010). Ab initio thermodynamics calculation of all-optical time-resolved calorimetry of nanosize systems: Evidence of nanosecond decoupling of electron and phonon temperatures. *Phys. Rev. B*, 81:155426.

Bao, W., Broholm, C., Aeppli, G., Dai, P., Honig, J. M., and Metcalf, P. (1997). Dramatic switching of magnetic exchange in a classic transition metal oxide: Evidence for orbital ordering. *Phys. Rev. Lett.*, 78:507–510.

Basov, D. N., Averitt, R. D., and Hsieh, D. (2017). Towards properties on demand in quantum materials. *Nature Materials*, 16(11):1077–1088.

Basov, D. N., Averitt, R. D., van der Marel, D., Dressel, M., and Haule, K. (2011). Electrodynamics of correlated electron materials. *Rev. Mod. Phys.*, 83:471–541.

Baum, P., Yang, D.-S., and Zewail, A. H. (2007). 4d visualization of transitional structures in phase transformations by electron diffraction. *Science*, 318(5851):788–792.

Baus, M. and Lovett, R. (1990). Generalization of the stress tensor to nonuniform fluids and solids and its relation to saint-venant's strain compatibility conditions. *Phys. Rev. Lett.*, 65:1781–1783.

Baus, M. and Lovett, R. (1991). Stress-strain relations in nonuniform equilibrium fluids. *Phys. Rev. A*, 44:1211–1218.

Bear, M., Connors, B., and Paradiso, M. (2007). *Neuroscience*. Neuroscience: Exploring the Brain. Lippincott Williams & Wilkins.

Bethe, H. (1928). Theorie der beugung von elektronen an kristallen. *Annalen der Physik*, 392(17):55–129.

Bhandari, K. P. and Ellingson, R. J. (2018). 11 - an overview of hybrid organic–inorganic metal halide perovskite solar cells. In Letcher, T. M. and Fthenakis, V. M., editors, *A Comprehensive Guide to Solar Energy Systems*, pages 233 – 254. Academic Press.

Bloch, F. (1928). Quantum mechanics of electrons in crystal lattices. *Z. Phys*, 52:555–600.

Bonnell, D. A., Basov, D. N., Bode, M., Diebold, U., Kalinin, S. V., Madhavan, V., Novotny, L., Salmeron, M., Schwarz, U. D., and Weiss, P. S. (2012). Imaging physical phenomena with local probes: From electrons to photons. *Rev. Mod. Phys.*, 84:1343–1381.

Borg, S. F. (1990). *Fundamentals of Engineering Elasticity*. World Scientific.

Bruggeman, D. A. G. (1935). Berechnung verschiedener physikalischer konstanten von heterogenen substanzen. i. dielektrizitätskonstanten und leitfähigkeiten der mischkörper aus isotropen substanzen. *Annalen der Physik*, 416(7):636–664.

Caddeo, C., Melis, C., Ronchi, A., Giannetti, C., Ferrini, G., Rurali, R., Colombo, L., and Banfi, F. (2017). Thermal boundary resistance from transient nanocalorimetry: A multiscale modeling approach. *Phys. Rev. B*, 95:085306.

Cahn, J. W. (1956). The kinetics of grain boundary nucleated reactions. *Acta Metallurgica*, 4(5):449 – 459.

Chudnovskii, F., Andreev, V., Kuksenko, V., Piculin, V., Frolov, D., Metcalf, P., and Honig, J. (1997). Acoustic emission during metal–insulator phase transition in V_2O_3. *Journal of Solid State Chemistry*, 133(2):430 – 433.

Cocker, T. L., Titova, L. V., Fourmaux, S., Bandulet, H. C., Brassard, D., Kieffer, J. C., El Khakani, M. A., and Hegmann, F. A. (2010). Terahertz conductivity of the metal-insulator transition in a nanogranular VO_2 film. *Applied Physics Letters*, 97(22):221905.

Cooley, J. W. and Tukey, J. W. (1965). An algorithm for the machine calculation of complex fourier series. *Mathematics of Computation*, 19(90):297–301.

De Poli, A. (2020). Nanotexture and dynamics of the Mott insulator to metal transition in V_2O_3, Master's thesis, Catholic University of the Sacred Heart.

del Valle, J., Ramírez, J. G., Rozenberg, M. J., and Schuller, I. K. (2018). Challenges in materials and devices for resistive-switching-based neuromorphic computing. *Journal of Applied Physics*, 124(21):211101.

del Valle, J., Salev, P., Tesler, F., Vargas, N. M., Kalcheim, Y., Wang, P., Trastoy, J., Lee, M.-H., Kassabian, G., Ramírez, J. G., Rozenberg, M. J., and Schuller, I. K. (2019). Subthreshold firing in Mott nanodevices. *Nature*, 569(7756):388–392.

Dernier, P. D. and Marezio, M. (1970). Crystal structure of the low-temperature antiferromagnetic phase of V_2O_3. *Phys. Rev. B*, 2:3771–3776.

Dillemans, L., Smets, T., Lieten, R. R., Menghini, M., Su, C.-Y., and Locquet, J.-P. (2014). Evidence of the metal-insulator transition in ultrathin unstrained V_2O_3 thin films. *Applied Physics Letters*, 104(7):071902.

Dimoulas, A., Vellianitis, G., Mavrou, G., Apostolopoulos, G., Travlos, A., Wiemer, C., Fanciulli, M., and Rittersma, Z. M. (2004). $La_2Hf_2O_7$ high-k gate dielectric grown directly on Si(001) by molecular-beam epitaxy. *Applied Physics Letters*, 85(15):3205–3207.

Ding, Y., Chen, C.-C., Zeng, Q., Kim, H.-S., Han, M. J., Balasubramanian, M., Gordon, R., Li, F., Bai, L., Popov, D., Heald, S. M., Gog, T., Mao, H.-k., and van Veenendaal, M. (2014). Novel high-pressure monoclinic metallic phase of V_2O_3. *Phys. Rev. Lett.*, 112:056401.

Dressel, M. and Grüner, G. (2002). *Electrodynamics of Solids: Optical Properties of Electrons in Matter*. Cambridge University Press.

Dönges, S. A., Khatib, O., O'Callahan, B. T., Atkin, J. M., Park, J. H., Cobden, D., and Raschke, M. B. (2016). Ultrafast nanoimaging of the photoinduced phase transition dynamics in VO_2. *Nano Letters*, 16(5):3029–3035. PMID: 27096877.

E.M. Litshitz, L. P. (1981). Chapter xii - kinetics of phase transitions. In E.M. Litshitz, L. P., editor, *Course of Theoretical Physics*, volume 10 of *Course of Theoretical Physics*, pages 427 – 447. Pergamon, Amsterdam.

Fonck, E., Feigl, G. G., Fasel, J., Sage, D., Unser, M., Rüfenacht, D. A., and Stergiopulos, N. (2009). Effect of aging on elastin functionality in human cerebral arteries. *Stroke*, 40(7):2552–2556.

Frandsen, B. A., Kalcheim, Y., Valmianski, I., McLeod, A. S., Guguchia, Z., Cheung, S. C., Hallas, A. M., Wilson, M. N., Cai, Y., Luke, G. M., Salman, Z., Suter, A., Prokscha, T., Murakami, T., Kageyama, H., Basov, D. N., Schuller, I. K., and Uemura, Y. J. (2019). Intertwined magnetic, structural, and electronic transitions in V_2O_3. *Phys. Rev. B*, 100:235136.

Fujiwara, H., Sekiyama, A., Mo, S.-K., Allen, J. W., Yamaguchi, J., Funabashi, G., Imada, S., Metcalf, P., Higashiya, A., Yabashi, M., Tamasaku, K., Ishikawa, T., and Suga, S. (2011). Evidence for the constancy of u in the mott transition of V_2O_3. *Phys. Rev. B*, 84:075117.

Gerstner, W., Kistler, W. M., Naud, R., and Paninski, L. (2014). *Neuronal Dynamics: From Single Neurons to Networks and Models of Cognition*. Cambridge University Press.

Giannetti, C., Capone, M., Fausti, D., Fabrizio, M., Parmigiani, F., and Mihailovic, D. (2016). Ultrafast optical spectroscopy of strongly correlated materials and high-temperature superconductors: a non-equilibrium approach. *Advances in Physics*, 65(2):58–238.

Giorgianni, F., Sakai, J., and Lupi, S. (2019). Overcoming the thermal regime for the electric-field driven Mott transition in vanadium sesquioxide. *Nature Communications*, 10(1):1159.

Grieger, D. and Fabrizio, M. (2015). Low-temperature magnetic ordering and structural distortions in vanadium sesquioxide V_2O_3. *Phys. Rev. B*, 92:075121.

Guénon, S., Scharinger, S., Wang, S., Ramírez, J. G., Koelle, D., Kleiner, R., and Schuller, I. K. (2013). Electrical breakdown in a V_2O_3 device at the insulator-to-metal transition. *EPL (Europhysics Letters)*, 101(5):57003.

Hansmann, P., Toschi, A., Sangiovanni, G., Saha-Dasgupta, T., Lupi, S., Marsi, M., and Held, K. (2013). Mott–hubbard transition in V_2O_3 revisited. *physica status solidi (b)*, 250(7):1251–1264.

Henning, P. F., Homes, C. C., Maslov, S., Carr, G. L., Basov, D. N., Nikolić, B., and Strongin, M. (1999). Infrared studies of the onset of conductivity in ultrathin Pb films. *Phys. Rev. Lett.*, 83:4880–4883.

Homm Jara, P. (2019). Electronic, structural and optical phase transitions in strongly correlated oxide thin films grown by molecular beam epitaxy, PhD thesis, KU Leuven.

Hu, W., Kaiser, S., Nicoletti, D., Hunt, C. R., Gierz, I., Hoffmann, M. C., Le Tacon, M., Loew, T., Keimer, B., and Cavalleri, A. (2014). Optically enhanced coherent transport in $YBa_2Cu_3O_{6.5}$ by ultrafast redistribution of interlayer coupling. *Nature Materials*, 13(7):705–711.

Ielmini, D. (2016). Resistive switching memories based on metal oxides: mechanisms, reliability and scaling. *Semiconductor Science and Technology*, 31(6):063002.

Imada, M., Fujimori, A., and Tokura, Y. (1998). Metal-insulator transitions. *Rev. Mod. Phys.*, 70:1039–1263.

Indiveri, G., Linares-Barranco, B., Hamilton, T., van Schaik, A., Etienne-Cummings, R., Delbruck, T., Liu, S.-C., Dudek, P., Häfliger, P., Renaud, S., Schemmel, J., Cauwenberghs, G., Arthur, J., Hynna, K., Folowosele, F., SAÏGHI, S., Serrano-Gotarredona, T., Wijekoon, J., Wang, Y., and Boahen, K. (2011). Neuromorphic silicon neuron circuits. *Frontiers in Neuroscience*, 5:73.

Inoue, I. H. and Rozenberg, M. J. (2008). Taming the Mott transition for a novel Mott transistor. *Advanced Functional Materials*, 18(16):2289–2292.

Janod, E., Tranchant, J., Corraze, B., Querré, M., Stoliar, P., Rozenberg, M., Cren, T., Roditchev, D., Phuoc, V. T., Besland, M.-P., and Cario, L. (2015). Resistive switching in mott insulators and correlated systems. *Advanced Functional Materials*, 25(40):6287–6305.

Jayaraman, A., McWhan, D. B., Remeika, J. P., and Dernier, P. D. (1970). Critical behavior of the mott transition in cr-doped V_2O_3. *Phys. Rev. B*, 2:3751–3756.

Jepsen, P. U., Fischer, B. M., Thoman, A., Helm, H., Suh, J. Y., Lopez, R., and Haglund, R. F. (2006). Metal-insulator phase transition in a VO_2 thin film observed with terahertz spectroscopy. *Phys. Rev. B*, 74:205103.

Kalcheim, Y., Butakov, N., Vargas, N. M., Lee, M.-H., del Valle, J., Trastoy, J., Salev, P., Schuller, J., and Schuller, I. K. (2019). Robust coupling between structural and electronic transitions in a Mott material. *Phys. Rev. Lett.*, 122:057601.

Kalcheim, Y., Camjayi, A., del Valle, J., Salev, P., Rozenberg, M., and Schuller, I. K. (2020). Non-thermal resistive switching in Mott insulator nanowires. *Nature Communications*, 11(1):2985.

Keer, H., Dickerson, D., Kuwamoto, H., Barros, H., and Honig, J. (1976). Heat capacity of pure and doped V_2O_3 single crystals. *Journal of Solid State Chemistry*, 19(1):95 – 102.

Kim, B.-J., Lee, Y. W., Choi, S., Lim, J.-W., Yun, S. J., Kim, H.-T., Shin, T.-J., and Yun, H.-S. (2008). Micrometer x-ray diffraction study of VO_2 films: Separation between metal-insulator transition and structural phase transition. *Phys. Rev. B*, 77:235401.

Kim, H.-T., Chae, B.-G., Youn, D.-H., Maeng, S.-L., Kim, G., Kang, K.-Y., and Lim, Y.-S. (2004). Mechanism and observation of Mott transition in VO_2-based two- and three-terminal devices. *New Journal of Physics*, 6:52–52.

Kim, H.-T., Lee, Y. W., Kim, B.-J., Chae, B.-G., Yun, S. J., Kang, K.-Y., Han, K.-J., Yee, K.-J., and Lim, Y.-S. (2006). Monoclinic and correlated metal phase in VO_2 as evidence of the mott transition: Coherent phonon analysis. *Phys. Rev. Lett.*, 97:266401.

Krause, H.-J. and Kreutzbruck, M. (2002). Recent developments in squid nde. *Physica C: Superconductivity*, 368(1):70 – 79.

Kübler, C., Ehrke, H., Huber, R., Lopez, R., Halabica, A., Haglund, R. F., and Leitenstorfer, A. (2007). Coherent structural dynamics and electronic correlations during an ultrafast insulator-to-metal phase transition in VO_2. *Phys. Rev. Lett.*, 99:116401.

Kündel, J., Pontiller, P., Müller, C., Obermeier, G., Liu, Z., Nateprov, A. A., Hörner, A., Wixforth, A., Horn, S., and Tidecks, R. (2013). Direct observation of the lattice precursor of the metal-to-insulator transition in v2o3 thin films by surface acoustic waves. *Applied Physics Letters*, 102(10):101904.

Lantz, G. (2015). Ultrafast electron dynamics in Mott materials, PhD thesis (Université Paris-Sud).

Lantz, G., Mansart, B., Grieger, D., Boschetto, D., Nilforoushan, N., Papalazarou, E., Moisan, N., Perfetti, L., Jacques, V. L. R., Le Bolloc'h, D., Laulhé, C., Ravy, S., Rueff, J.-P., Glover, T. E., Hertlein, M. P., Hussain, Z., Song, S., Chollet, M., Fabrizio, M., and Marsi, M. (2017). Ultrafast evolution and transient phases of a prototype out-of-equilibrium Mott–Hubbard material. *Nature Communications*, 8(1):13917.

LeCun, Y., Bengio, Y., and Hinton, G. (2015). Deep learning. *Nature*, 521(7553):436–444.

Lee, S., Hippalgaonkar, K., Yang, F., Hong, J., Ko, C., Suh, J., Liu, K., Wang, K., Urban, J. J., Zhang, X., Dames, C., Hartnoll, S. A., Delaire, O., and Wu, J. (2017). Anomalously low electronic thermal conductivity in metallic vanadium dioxide. *Science*, 355(6323):371–374.

Li, Z., Wu, J., Hu, Z., Lin, Y., Chen, Q., Guo, Y., Liu, Y., Zhao, Y., Peng, J., Chu, W., Wu, C., and Xie, Y. (2017). Imaging metal-like monoclinic phase stabilized by surface coordination effect in vanadium dioxide nanobeam. *Nature Communications*, 8(1):15561.

Liang, Y., Qin, P., Liang, Z., Zhang, L., Yuan, X., and Zhang, Y. (2019). Identification of a monoclinic metallic state in VO_2 from a modified first-principles approach. *Modern Physics Letters B*, 33(12):1950148.

Limelette, P., Georges, A., Jérome, D., Wzietek, P., Metcalf, P., and Honig, J. M. (2003). Universality and critical behavior at the mott transition. *Science*, 302(5642):89–92.

Liu, M. K., Pardo, B., Zhang, J., Qazilbash, M. M., Yun, S. J., Fei, Z., Shin, J.-H., Kim, H.-T., Basov, D. N., and Averitt, R. D. (2011). Photoinduced phase transitions by time-resolved far-infrared spectroscopy in V_2O_3. *Phys. Rev. Lett.*, 107:066403.

Liu, X., Li, S., Nandi, S. K., Venkatachalam, D. K., and Elliman, R. G. (2016). Threshold switching and electrical self-oscillation in niobium oxide films. *Journal of Applied Physics*, 120(12):124102.

Lüning, J., Nolting, F., Scholl, A., Ohldag, H., Seo, J. W., Fompeyrine, J., Locquet, J.-P., and Stöhr, J. (2003). Determination of the antiferromagnetic spin axis in epitaxial $LaFeO_3$ films by x-ray magnetic linear dichroism spectroscopy. *Phys. Rev. B*, 67:214433.

Luo, Y., Su, F., Zhang, C., Zhong, L., Pan, S., Xu, S., Wang, H., Dai, J., and Li, G. (2017). Terahertz transport dynamics in the metal-insulator transition of V_2O_3 thin film. *Optics Communications*, 387:385 – 389.

Lupi, S., Baldassarre, L., Mansart, B., Perucchi, A., Barinov, A., Dudin, P., Papalazarou, E., Rodolakis, F., Rueff, J. P., Itié, J. P., Ravy, S., Nicoletti, D., Postorino, P., Hansmann, P., Parragh, N., Toschi, A., Saha-Dasgupta, T., Andersen, O. K., Sangiovanni, G., Held, K., and Marsi, M. (2010). A microscopic view on the Mott transition in chromium-doped V_2O_3. *Nature Communications*, 1(1):105.

Mahowald, M. and Douglas, R. (1991). A silicon neuron. *Nature*, 354(6354):515–518.

Majid, S. S., Shukla, D. K., Rahman, F., Gautam, K., Choudhary, R. J., Sathe, V. G., and Phase, D. M. (2017). Stabilization of metallic phase in V_2O_3 thin film. *Applied Physics Letters*, 110(17):173101.

Malitson, I. H. (1962). Refraction and dispersion of synthetic sapphire. *J. Opt. Soc. Am.*, 52(12):1377–1379.

Maniarasu, S., Manjunath, V., Veerappan, G., and Ramasamy, E. (2018). Chapter 11 - flexible perovskite solar cells. In Thomas, S. and Thankappan, A., editors, *Perovskite Photovoltaics*, pages 341 – 371. Academic Press.

Mansart, B., Boschetto, D., Sauvage, S., Rousse, A., and Marsi, M. (2010). Mott transition in cr-doped V_2O_3 studied by ultrafast reflectivity: Electron correlation effects on the transient response. *EPL (Europhysics Letters)*, 92(3):37007.

Mattoni, G., Zubko, P., Maccherozzi, F., van der Torren, A. J. H., Boltje, D. B., Hadjimichael, M., Manca, N., Catalano, S., Gibert, M., Liu, Y., Aarts, J., Triscone, J. M., Dhesi, S. S., and Caviglia, A. D. (2016). Striped nanoscale phase separation at the metal-insulator transition of heteroepitaxial nickelates. *Nature Communications*, 7(1):13141.

Mazza, G., Amaricci, A., Capone, M., and Fabrizio, M. (2016). Field-driven mott gap collapse and resistive switch in correlated insulators. *Phys. Rev. Lett.*, 117:176401.

McLeod, A. S., van Heumen, E., Ramirez, J. G., Wang, S., Saerbeck, T., Guenon, S., Goldflam, M., Anderegg, L., Kelly, P., Mueller, A., Liu, M. K., Schuller, I. K., and Basov, D. N. (2016). Nanotextured phase coexistence in the correlated insulator V_2O_3. *Nature Physics*, 13(1):80–86.

McWhan, D. B., Menth, A., Remeika, J. P., Brinkman, W. F., and Rice, T. M. (1973). Metal-insulator transitions in pure and doped V_2O_3. *Phys. Rev. B*, 7:1920–1931.

McWhan, D. B. and Remeika, J. P. (1970). Metal-insulator transition in $(V_{1-x}Cr_x)_2O_3$. *Phys. Rev. B*, 2:3734–3750.

McWhan, D. B., Rice, T. M., and Remeika, J. P. (1969). Mott transition in cr-doped V_2O_3. *Phys. Rev. Lett.*, 23:1384–1387.

Mead, C. (1990). Neuromorphic electronic systems. *Proceedings of the IEEE*, 78(10):1629–1636.

Mitrano, M., Cantaluppi, A., Nicoletti, D., Kaiser, S., Perucchi, A., Lupi, S., Di Pietro, P., Pontiroli, D., Riccò, M., Clark, S. R., Jaksch, D., and Cavalleri, A. (2016). Possible light-induced superconductivity in K_3C_{60} at high temperature. *Nature*, 530(7591):461–464.

Mo, S.-K., Denlinger, J. D., Kim, H.-D., Park, J.-H., Allen, J. W., Sekiyama, A., Yamasaki, A., Kadono, K., Suga, S., Saitoh, Y., Muro, T., Metcalf, P., Keller, G., Held, K., Eyert, V., Anisimov, V. I., and Vollhardt, D. (2003). Prominent quasiparticle peak in the photoemission spectrum of the metallic phase of V_2O_3. *Phys. Rev. Lett.*, 90:186403.

Mo, S.-K., Kim, H.-D., Allen, J. W., Gweon, G.-H., Denlinger, J. D., Park, J.-H., Sekiyama, A., Yamasaki, A., Suga, S., Metcalf, P., and Held, K. (2004). Filling of the mott-hubbard gap in the high temperature photoemission spectrum of $(V_{0.972}Cr_{0.028})_2O_3$. *Phys. Rev. Lett.*, 93:076404.

Mo, S.-K., Kim, H.-D., Denlinger, J. D., Allen, J. W., Park, J.-H., Sekiyama, A., Yamasaki, A., Suga, S., Saitoh, Y., Muro, T., and Metcalf, P. (2006). Photoemission study of $(V_{1-x}M_x)_2O_3$ (M=Cr, Ti). *Phys. Rev. B*, 74:165101.

Morrison, V. R., Chatelain, R. P., Tiwari, K. L., Hendaoui, A., Bruhács, A., Chaker, M., and Siwick, B. J. (2014). A photoinduced metal-like phase of monoclinic VO_2 revealed by ultrafast electron diffraction. *Science*, 346(6208):445–448.

Mott, N. (1990). On metal-insulator transitions. *Journal of Solid State Chemistry*, 88(1):5 – 7.

Nag, J., Haglund, R. F., Andrew Payzant, E., and More, K. L. (2012). Non-congruence of thermally driven structural and electronic transitions in VO_2. *Journal of Applied Physics*, 112(10):103532.

Nasu, K. (2004). *Photoinduced phase transitions.* World Scientific, Singapore.

Nishigaki, Y., Nagai, T., Nishiwaki, M., Aizawa, T., Kozawa, M., Hanzawa, K., Kato, Y., Sai, H., Hiramatsu, H., Hosono, H., and Fujiwara, H. (2020). Extraordinary strong band-edge absorption in distorted chalcogenide perovskites. *Solar RRL*, 4(5):1900555.

O'Callahan, B. T., Jones, A. C., Hyung Park, J., Cobden, D. H., Atkin, J. M., and Raschke, M. B. (2015). Inhomogeneity of the ultrafast insulator-to-metal transition dynamics of VO_2. *Nature Communications*, 6(1):6849.

Otto, M. R., René de Cotret, L. P., Valverde-Chavez, D. A., Tiwari, K. L., Émond, N., Chaker, M., Cooke, D. G., and Siwick, B. J. (2019). How optical excitation controls the structure and properties of vanadium dioxide. *Proceedings of the National Academy of Sciences*, 116(2):450–455.

Papalazarou, E., Gatti, M., Marsi, M., Brouet, V., Iori, F., Reining, L., Annese, E., Vobornik, I., Offi, F., Fondacaro, A., Huotari, S., Lacovig, P., Tjernberg, O., Brookes, N. B., Sacchi, M., Metcalf, P., and Panaccione, G. (2009). Valence-band electronic structure of V_2O_3: Identification of v and o bands. *Phys. Rev. B*, 80:155115.

Papon, P., Leblond, J., and Meijer, P. (2006). *The physics of phase transitions: Concepts and applications.*

Park, J.-H., Tjeng, L. H., Tanaka, A., Allen, J. W., Chen, C. T., Metcalf, P., Honig, J. M., de Groot, F. M. F., and Sawatzky, G. A. (2000). Spin and orbital occupation and phase transitions in V_2O_3. *Phys. Rev. B*, 61:11506–11509.

Pfalzer, P., Obermeier, G., Klemm, M., Horn, S., and Denboer, M. (2006). Structural precursor to the metal-insulator transition in V_2O_3. *Phys. Rev. B*, 73.

Porat, O., Heremans, C., and Tuller, H. (1997). Stability and mixed ionic electronic conduction in $Gd_2(Ti_{1-x}Mo_x)_2O_7$ under anodic conditions. *Solid State Ionics*, 94(1):75 – 83. Papers from the International Workshop.

Porat, O., Spears, M., Heremans, C., Kosacki, I., and Tuller, H. (1996). Modelling and characterization of mixed ionic-electronic conduction in $Gd_2(Ti_{1-x}Mn_x)_2O_7 + \mathrm{y}$. *Solid State Ionics*, 86-88:285 – 288. Proceedings of the 10th International Conference on Solid State Ionics.

Poteryaev, A. I., Tomczak, J. M., Biermann, S., Georges, A., Lichtenstein, A. I., Rubtsov, A. N., Saha-Dasgupta, T., and Andersen, O. K. (2007). Enhanced crystal-field splitting and orbital-selective coherence induced by strong correlations in V_2O_3. *Phys. Rev. B*, 76:085127.

Püspöki, Z., Storath, M., Sage, D., and Unser, M. (2016). *Transforms and Operators for Directional Bioimage Analysis: A Survey*, pages 69–93. Springer International Publishing, Cham.

Qazilbash, M. M., Burch, K. S., Whisler, D., Shrekenhamer, D., Chae, B. G., Kim, H. T., and Basov, D. N. (2006). Correlated metallic state of vanadium dioxide. *Phys. Rev. B*, 74:205118.

Qazilbash, M. M., Schafgans, A. A., Burch, K. S., Yun, S. J., Chae, B. G., Kim, B. J., Kim, H. T., and Basov, D. N. (2008). Electrodynamics of the vanadium oxides VO_2 and V_2O_3. *Phys. Rev. B*, 77:115121.

Qazilbash, M. M., Tripathi, A., Schafgans, A. A., Kim, B.-J., Kim, H.-T., Cai, Z., Holt, M. V., Maser, J. M., Keilmann, F., Shpyrko, O. G., and Basov, D. N. (2011). Nanoscale imaging of the electronic and structural transitions in vanadium dioxide. *Phys. Rev. B*, 83:165108.

Rana, R., Klopf, J. M., Grenzer, J., Schneider, H., Helm, M., and Pashkin, A. (2019). Nonthermal nature of photoinduced insulator-to-metal transition in NbO_2. *Phys. Rev. B*, 99:041102.

Razza, S., Castro-Hermosa, S., Di Carlo, A., and Brown, T. M. (2016). Research update: Large-area deposition, coating, printing, and processing techniques for the upscaling of perovskite solar cell technology. *APL Materials*, 4(9):091508.

Rezakhaniha, R., Agianniotis, A., Schrauwen, J. T. C., Griffa, A., Sage, D., Bouten, C. V. C., van de Vosse, F. N., Unser, M., and Stergiopulos, N. (2012). Experimental investigation of collagen waviness and orientation in the arterial adventitia using confocal laser scanning microscopy. *Biomechanics and Modeling in Mechanobiology*, 11(3):461–473.

Rodolakis, F., Hansmann, P., Rueff, J.-P., Toschi, A., Haverkort, M. W., Sangiovanni, G., Tanaka, A., Saha-Dasgupta, T., Andersen, O. K., Held, K., Sikora, M., Alliot, I., Itié, J.-P., Baudelet, F., Wzietek, P., Metcalf, P., and Marsi, M. (2010). Inequivalent routes across the mott transition in V_2O_3 explored by x-ray absorption. *Phys. Rev. Lett.*, 104:047401.

Ronchi, A., Franceschini, P., Fanfarillo, L., Homm, P., Menghini, M., Peli, S., Ferrini, G., Banfi, F., Cilento, F., Damascelli, A., Parmigiani, F., Locquet, J.-P., Fabrizio, M., Capone, M., and Giannetti, C. (2018). Ultrafast orbital manipulation and Mott physics in multi-band correlated materials. In Betz, M. and Elezzabi, A. Y., editors, *Ultrafast Phenomena and Nanophotonics XXII*, volume 10530, pages 77 – 93. International Society for Optics and Photonics, SPIE.

Ronchi, A., Homm, P., Menghini, M., Franceschini, P., Maccherozzi, F., Banfi, F., Ferrini, G., Cilento, F., Parmigiani, F., Dhesi, S. S., Fabrizio, M., Locquet, J.-P., and Giannetti, C. (2019). Early-stage dynamics of metallic droplets embedded in the nanotextured mott insulating phase of V_2O_3. *Phys. Rev. B*, 100:075111.

Roytburd, A. (1995). Principal concepts of martensitic theory. *Journal de Physique IV Colloque C8*, 05:21–30.

Rueden, C. T., Schindelin, J., Hiner, M. C., DeZonia, B. E., Walter, A. E., Arena, E. T., and Eliceiri, K. W. (2017). Imagej2: Imagej for the next generation of scientific image data. *BMC Bioinformatics*, 18(1):529.

Sandri, M. and Fabrizio, M. (2015). Nonequilibrium gap collapse near a first-order Mott transition. *Phys. Rev. B*, 91:115102.

Sato, K., Kobayashi, S., and Nakashima, T. (2011). Present status and future perspective of Bismuth-based high-temperature superconducting wires realizing application systems. *Japanese Journal of Applied Physics*, 51(1):010006.

Sawa, A. (2008). Resistive switching in transition metal oxides. *Materials Today*, 11(6):28 – 36.

Schindelin, J., Arganda-Carreras, I., Frise, E., Kaynig, V., Longair, M., Pietzsch, T., Preibisch, S., Rueden, C., Saalfeld, S., Schmid, B., Tinevez, J.-Y., White, D. J., Hartenstein, V., Eliceiri, K., Tomancak, P., and Cardona, A. (2012). Fiji: an open-source platform for biological-image analysis. *Nature Methods*, 9:676–682.

Seikh, M. M., Narayana, C., Sood, A., Murugavel, P., Kim, M., Metcalf, P., Honig, J., and Rao, C. (2006). A brillouin study of the temperature-dependence of the acoustic modes across the insulator–metal transitions in V_2O_3 and cr-doped V_2O_3. *Solid State Communications*, 138(9):466 – 471.

Serdijn, W. and Dongen, M. (2016). *Design of Efficient and Safe Neural Stimulators - a multidisciplinary approach.*

Shenoy, S. R. and Lookman, T. (2008). Strain pseudospins with power-law interactions: Glassy textures of a cooled coupled-map lattice. *Phys. Rev. B*, 78:144103.

Shimizu, Y. and Maeda, K. (1998). Solid electrolyte NOx sensor using pyrochlore-type oxide electrode devoted to the late dr tetsuro seiyama. *Sensors and Actuators B: Chemical*, 52(1):84 – 89.

Shiohara, Y., Taneda, T., and Yoshizumi, M. (2011). Overview of materials and power applications of coated conductors project. *Japanese Journal of Applied Physics*, 51(1):010007.

Singer, A., Ramirez, J. G., Valmianski, I., Cela, D., Hua, N., Kukreja, R., Wingert, J., Kovalchuk, O., Glownia, J. M., Sikorski, M., Chollet, M., Holt, M., Schuller, I. K., and Shpyrko, O. G. (2018). Nonequilibrium phase precursors during a photoexcited insulator-to-metal transition in V_2O_3. *Phys. Rev. Lett.*, 120:207601.

Sohn, J. M., Kim, M. R., and Woo, S. I. (2003). The catalytic activity and surface characterization of $Ln_2B_2O_7$ (Ln=Sm, Eu, Gd and Tb; B=Ti or Zr) with pyrochlore structure as novel ch4 combustion catalyst. *Catalysis Today*, 83(1):289 – 297. 5th International Workshop on Catalytic Combustion.

Sommerfeld, A. (1928). Zur elektronentheorie der metalle auf grund der fermischen statistik. *Zeitschrift für Physik*, 47(1):1–32.

Stewart, M. K., Brownstead, D., Wang, S., West, K. G., Ramirez, J. G., Qazilbash, M. M., Perkins, N. B., Schuller, I. K., and Basov, D. N. (2012). Insulator-to-metal transition and correlated metallic state of V_2O_3 investigated by optical spectroscopy. *Phys. Rev. B*, 85:205113.

Stoliar, P., Cario, L., Janod, E., Corraze, B., Guillot-Deudon, C., Salmon-Bourmand, S., Guiot, V., Tranchant, J., and Rozenberg, M. (2013). Universal electric-field-driven resistive transition in narrow-gap mott insulators. *Advanced Materials*, 25(23):3222–3226.

Stoliar, P., Tranchant, J., Corraze, B., Janod, E., Besland, M.-P., Tesler, F., Rozenberg, M., and Cario, L. (2017). A leaky-integrate-and-fire neuron analog realized with a Mott insulator. *Advanced Functional Materials*, 27(11):1604740.

Szot, K., Speier, W., Bihlmayer, G., and Waser, R. (2006). Switching the electrical resistance of individual dislocations in single-crystalline $SrTiO_3$. *Nature Materials*, 5(4):312–320.

Tokura, Y. (2003). Correlated-Electron Physics in Transition-Metal Oxides. *Physics Today*, 56(7):50–55.

Tokura, Y. (2006). Photoinduced phase transition: A tool for generating a hidden state of matter. *Journal of the Physical Society of Japan*, 75(1):011001.

Tokura, Y., Kawasaki, M., and Nagaosa, N. (2017). Emergent functions of quantum materials. *Nature Physics*, 13(11):1056–1068.

Torriss, B., Ibrahim, A., Ozaki, T., and Chaker, M. (2018). Ultrafast photoinduced insulator-metal transition in epitaxial samarium nickelate thin films investigated by time-resolved terahertz spectroscopy. *Phys. Rev. B*, 98:165132.

Trastoy, J., Camjayi, A., del Valle, J., Kalcheim, Y., Crocombette, J.-P., Gilbert, D. A., Borchers, J. A., Villegas, J. E., Ravelosona, D., Rozenberg, M. J., and Schuller, I. K. (2020). Magnetic field frustration of the metal-insulator transition in V_2O_3. *Phys. Rev. B*, 101:245109.

Vidas, L., Schick, D., Martínez, E., Perez-Salinas, D., Ramos-Álvarez, A., Cichy, S., Batlle-Porro, S., Johnson, A. S., Hallman, K. A., Haglund, R. F., and Wall, S. (2020). Does VO_2 host a transient monoclinic metallic phase? *Phys. Rev. X*, 10:031047.

Wall, S., Wegkamp, D., Foglia, L., Appavoo, K., Nag, J., Haglund, R. F., Stähler, J., and Wolf, M. (2012). Ultrafast changes in lattice symmetry probed by coherent phonons. *Nature Communications*, 3(1):721.

Wall, S., Yang, S., Vidas, L., Chollet, M., Glownia, J. M., Kozina, M., Katayama, T., Henighan, T., Jiang, M., Miller, T. A., Reis, D. A., Boatner, L. A., Delaire, O., and Trigo, M. (2018). Ultrafast disordering of vanadium dimers in photoexcited VO_2. *Science*, 362(6414):572–576.

Waser, R. and Aono, M. (2007). Nanoionics-based resistive switching memories. *Nature Materials*, 6(11):833–840.

Waser, R., Dittmann, R., Staikov, G., and Szot, K. (2009). Redox-based resistive switching memories – nanoionic mechanisms, prospects, and challenges. *Advanced Materials*, 21(25-26):2632–2663.

Weber, M. J. (2001). *Handbook of Optical Materials.* CRC Press, Boca Raton, FL.

Wong, H. . P., Lee, H., Yu, S., Chen, Y., Wu, Y., Chen, P., Lee, B., Chen, F. T., and Tsai, M. (2012). Metal–oxide RRAM. *Proceedings of the IEEE*, 100(6):1951–1970.

Yang, Z., Ko, C., and Ramanathan, S. (2011). Oxide electronics utilizing ultrafast metal-insulator transitions. *Annual Review of Materials Research*, 41(1):337–367.

Zhang, J. and Averitt, R. (2014). Dynamics and control in complex transition metal oxides. *Annual Review of Materials Research*, 44(1):19–43.

Zhou, Y. and Ramanathan, S. (2013). Correlated electron materials and field effect transistors for logic: A review. *Critical Reviews in Solid State and Materials Sciences*, 38(4):286–317.

Zhu, Y., Cai, Z., Chen, P., Zhang, Q., Highland, M. J., Jung, I. W., Walko, D. A., Dufresne, E. M., Jeong, J., Samant, M. G., Parkin, S. S. P., Freeland, J. W., Evans, P. G., and Wen, H. (2016). Mesoscopic structural phase progression in photo-excited VO_2 revealed by time-resolved x-ray diffraction microscopy. *Scientific Reports*, 6(1):21999.

Curriculum Vitae

ANDREA RONCHI

Birth: Brescia (Italy), 05/02/1990
Nationality: Italian
Mail: `a.robot@hotmail.it`
ORCID: 0000-0001-8960-4561

EDUCATION

Ph.D. in Physics 2016-2020
KU Leuven, Leuven, Belgium

M.S. in Physics 2013-2015
Universitá Cattolica del Sacro Cuore, Brescia, Italy
Grade 110 cum laude/110

B.S. in Physics 2009-2013
Universitá Cattolica del Sacro Cuore, Brescia, Italy
Grade 109/110

List of Publications

2020

A. Ronchi, P. Homm, M. Menghini, P. Franceschini, F. Maccherozzi, A. Fitzpatrick, F. Banfi, G. Ferrini, F. Cilento, F. Parmigiani, S. S. Dhesi, M. Fabrizio, J.-P. Locquet, and C. Giannetti. Photoinduced transient monoclinic metal-like state in V_2O_3 stabilized by nanotexture. in preparation, Oct 2020.

A. Ronchi, P. Franceschini, P. Homm, M. Gandolfi, G. Ferrini, S. Pagliara, F. Banfi, M. Menghini, J.-P. Locquet and C. Giannetti. Non-thermal light-assisted resistance collapse in a V_2O_3-based Mottronic device. *submitted to Phys. Rev. Applied*, Oct 2020.

A. Ronchi, A. Sterzi, M. Gandolfi, A. Belarouci, C. Giannetti, N. Del Fatti, F. Banfi, and G. Ferrini. Descrimination of nano-objects via cluster analysis techniques applied to time-resolved thermo-acoustic microscopy. *submitted to Ultrasonics*, Oct 2020.

S. Peli, **A. Ronchi**, G. Bianchetti, F. Rossella, C. Giannetti, M. Chiari, P. Pingue, F. Banfi, and G. Ferrini. Optical and mechanical properties of streptavidin-conjugated gold nanospheres through data mining techniques. *Sci. Rep.*, **10**:16230 (2020).

P. Franceschini, L. Carletti, A.P. Pushkarev, F. Preda, A. Perri, A. Tognazzi, **A. Ronchi**, G. Ferrini, S. Pagliara, F. Banfi, D. Polli, G. Cerullo, C. De Angelis, S. Makarov, and C. Giannetti. Tuning the Ultrafast Response of Fano Resonances in Halide Perovskite Nanoparticles. *ACS Nano*, Oct 2020.

2019

A. Ronchi, P. Homm, M. Menghini, P. Franceschini, F. Maccherozzi, F. Banfi, G. Ferrini, F. Cilento, F. Parmigiani, S. S. Dhesi, M. Fabrizio, J.-P. Locquet, and C. Giannetti. Early-stage dynamics of metallic droplets embedded in the nanotextured Mott insulating phase of V_2O_3. *Phys. Rev. B*, **100**:075111, Aug 2019.

2018

A. Ronchi, P. Franceschini, L. Fanfarillo, P. Homm, M. Menghini, S. Peli, G. Ferrini, F. Banfi, F. Cilento, A. Damascelli, F. Parmigiani, J-P. Locquet, M. Fabrizio, M. Capone, and C. Giannetti Ultrafast orbital manipulation and Mott physics in multi-band correlated materials *Proc. SPIE*, 10530, Ultrafast Phenomena and Nanophotonics XXII, 105300V (22 February 2018).

F. Cilento, G. Manzoni, A. Sterzi, S. Peli, **A. Ronchi**, A. Crepaldi, F. Boschini, C. Cacho, R. Chapman, E. Springate, H. Eisaki, M. Greven, M. Berciu, A. F. Kemper, A. Damascelli, M. Capone, C. Giannetti, and F. Parmigiani Dynamics of correlation-frozen antinodal quasiparticles in superconducting cuprates, *Science Advances*, **4**:2 eaar1998 (2018).

2017

S. Peli, S. Dal Conte, R. Comin, N. Nembrini, **A. Ronchi**, P. Abrami, F. Banfi, G. Ferrini, D. Brida, S. Lupi, M. Fabrizio, A. Damascelli, M. Capone, G. Cerullo, and C. Giannetti. Mottness at Finite Doping and Charge Instabilities in Cuprates. *Nature Physics*, **13** (8), 806–811 (2017).

C. Caddeo, C. Melis, **A. Ronchi**, C. Giannetti, G. Ferrini, R. Rurali, L. Colombo, and F. Banfi. Thermal boundary resistance from transient nanocalorimetry: A multiscale modeling approach. *Phys. Rev. B*, **95**:085306, Feb 2017.

FACULTY OF SCIENCE
DEPARTMENT OF PHYSICS AND ASTRONOMY
SEMICONDUCTOR PHYSICS DIVISION
Celestijnenlaan 200D box 2417
B-3001 Leuven